# UC Santa Cruz

## UC Santa Cruz Electronic Theses and Dissertations

### Title

Observational and modeling studies of collision-coalescence in marine stratocumulus

### Permalink

https://escholarship.org/uc/item/6r73029h

### Author

Witte, Mikael Kurt

### Publication Date

2016

### Copyright Information

This work is made available under the terms of a Creative Commons Attribution-NonCommercial-ShareAlike License, availalbe at https://creativecommons.org/licenses/by-nc-sa/4.0/

Peer reviewed|Thesis/dissertation

eScholarship.org Powered by the California Digital Library
University of California

UNIVERSITY OF CALIFORNIA
SANTA CRUZ

# OBSERVATIONAL AND MODELING STUDIES OF COLLISION-COALESCENCE IN MARINE STRATOCUMULUS

A dissertation submitted in partial satisfaction of the
requirements for the degree of

DOCTOR OF PHILOSOPHY

in

EARTH SCIENCES

by

**Mikael K. Witte**

June 2016

The Dissertation of Mikael K. Witte
is approved:

Professor Patrick Chuang, Chair

Professor Nic Brummell

Assistant Professor Xi Zhang

Dean Tyrus Miller
Vice Provost and Dean of Graduate Studies

Copyright © by
Mikael K. Witte
2016

# Contents

**List of Figures** vi

**List of Tables** ix

**Abstract** x

**Dedication** xii

**Acknowledgments** xiii

**1 Introduction** 1
- 1.1 Overview of marine stratocumulus . . . 2
- 1.2 Microphysical processes in warm clouds . . . 5
  - 1.2.1 Theories of precipitation formation . . . 8
- 1.3 Summary . . . 12

**2 On Clouds and Clocks** 13
- 2.1 Introduction . . . 13
- 2.2 Methodology . . . 16
- 2.3 Results and Discussion . . . 19
  - 2.3.1 The clouds . . . 19
  - 2.3.2 The ideal clock . . . 21
  - 2.3.3 Failures . . . 22
  - 2.3.4 Total water as cumulus clock . . . 23
    - 2.3.4.1 Single-pulse clouds . . . 24
    - 2.3.4.2 Multiple-pulse clouds . . . 26
  - 2.3.5 Caveats and limitations . . . 31
- 2.4 Conclusions . . . 32

**3 Estimating collision-coalescence rates from observations of marine stratocumulus 35**
3.1 Introduction . . . 35
3.2 Method . . . 38
3.2.1 Observations . . . 38
3.2.2 Rebinning of the DSD . . . 40
3.2.3 Estimating rate constants from a DSD . . . 43
3.3 Validation against a collision box model . . . 44
3.3.1 Description of the model . . . 44
3.3.2 Derived rate constants . . . 45
3.4 Results . . . 49
3.4.1 Closure assumption . . . 49
3.4.2 Estimated rate constants and enhancement factors from leg composites . . . 49
3.4.3 Enhancement factors from individual segments . . . 50
3.4.4 Sensitivity of results to process representation . . . 53
3.5 Discussion . . . 55

**4 The role of microphysical spectral resolution on large eddy simulations of marine stratocumulus 57**
4.1 Introduction . . . 57
4.2 Model description . . . 60
4.2.1 Modifications to microphysics . . . 62
4.3 Case studies . . . 65
4.4 Results . . . 68
4.4.1 Basic characterization of output . . . 68
4.4.2 Changes in the drop size distribution . . . 77
4.4.3 Changes in the vertical structure of turbulence . . . 79
4.5 Summary . . . 86

**5 Can turbulent collision-coalescence improve the representation of drop size spectra in simulations of marine stratocumulus? 88**
5.1 Introduction . . . 88
5.2 Model description . . . 90
5.3 Observations and case studies . . . 92
5.3.1 Case 1: 0730 . . . 94
5.3.2 Case 2: 0812 . . . 96
5.3.3 Case 3: 0815 . . . 98
5.4 Model results and validation against observations . . . 100
5.5 Comparison of LES microphysics output with observations . . . 105

5.6 Discussion . . . . . 111

**6 Summary** **113**

**A Details of the rate constant analytical framework** **116**

**B Validation of radiative fluxes across spectral resolution** **118**

**Bibliography** **124**

# List of Figures


2.1 Environmental soundings taken over the period of time from which clouds are selected. With the exception of LWC, the profiles are clear-air domain averages. . . . . 18
2.2 Cloud volume vs normalized time. Lifetime $\tau$ is in minutes. . . . . 20
2.3 Volume-averaged time series of $\Delta\theta_v$. . . . . 21
2.4 Scatter plot of volume-averaged $\Delta\theta_v$ and $\frac{dV}{dt}$. . . . . 22
2.5 Time series of volume-averaged potential temperature. . . . . 24
2.6 Time series of the altitude of liquid water cloud center of mass. . . . . 25
2.7 Time series of cloud top altitude. . . . . 26
2.8 The time evolution of $r_t^*$ is well fit by linear regression. The solid black line is the fit and the dashed black lines are approximately one standard deviation from the mean slope. . . . . 27
2.9 Individual altitude time series of $r_t^*$ show the same general trend as the full-cloud average, but higher altitudes exhibit a larger dynamic range. . 28
2.10 Time series of $r_t^*$ averaged over the entire cloud and at individual levels. Cloud average $\Delta\theta_v$ is shown for comparison. . . . . 29
2.11 A cloud average $r_t^*$ time series for a double-pulse cloud. The solid black line is the single-pulse fit, the dashed black lines are the fit $t/\tau \pm 0.1$, and the gray area envelops the single-pulse cloud data. The Pulse 1 and Pulse 2 time axes show the independent pulse ages associated with times $b_1$ and $b_2$, respectively. . . . . 30
2.12 Time series of liquid water path. Liquid water path is the cloud-integrated LWC divided by maximum cross-sectional area. . . . . 33

3.1 Typical DSD observations from both cloud probes (PDI and CIP) from TO2 Leg 1, a non-drizzling case. . . . . 42
3.2 Rate constant as a function of collector drop diameter from the Bott model using the Hall kernel. . . . . 46
3.3 Bott model rate constants relative to corresponding Hall kernel values. . 47

3.4 Rate constants as calculated from POST PDI observations. . . . . 50
3.5 Observed rate constants normalized by Bott model output using the Hall kernel. For several of the largest monomer cases, observed rate constants are less than those predicted by the Bott model. . . . . 51
3.6 Probability density functions of enhancement factor from segments conditioned on collector drop diameter. . . . . 52
3.7 Observed rate constants normalized by Bott model output using the Ayala kernel with $\epsilon = 300\,\mathrm{cm\,s^{-3}}$. . . . . 54

4.1 Initial soundings . . . . . 66
4.2 Profiles of potential temperature $\theta$ . . . . . 69
4.3 Profiles of total water mixing ratio $q_t$ . . . . . 69
4.4 Profiles of LWC . . . . . 70
4.5 Difference profiles of LWC . . . . . 71
4.6 Time series of domain average LWP . . . . . 72
4.7 Time series of differences of domain mean LWP . . . . . 73
4.8 Profile of the DSD as a function of altitude at 30 m intervals in cloud ($\overline{q_l(z)} > 0.01\,\mathrm{g\,kg^{-1}}$), 0730 case . . . . . 74
4.9 Profile of the DSD as a function of altitude at 30 m intervals in cloud ($\overline{q_l(z)} > 0.01\,\mathrm{g\,kg^{-1}}$), 0812 case . . . . . 75
4.10 Profile of the DSD as a function of altitude at 30 m intervals in cloud ($\overline{q_l(z)} > 0.01\,\mathrm{g\,kg^{-1}}$), 0815 case . . . . . 76
4.11 Profiles of rain rate $R$ . . . . . 78
4.12 Profiles of the 99th percentile size of the mass DSD. Levels with $\overline{N_D} < 1\,\mathrm{cm^{-3}}$ per grid cell are excluded. . . . . 79
4.13 Profiles of average TKE . . . . . 80
4.14 Average profiles of buoyancy TKE production . . . . . 82
4.15 Profiles of $\overline{w'^2}$ . . . . . 83
4.16 Profiles of net latent heating rate. Cloud base for each simulation is denoted by hash marks on the abscissa and defined as the lowest level with $\overline{q_l} > 0.01\,\mathrm{g\,kg^{-1}}$. . . . . 84
4.17 Partitioning of buoyancy production by $w'$, 0812 case. Cloud base and top are denoted by hashmarks on abscissa. . . . . 85

5.1 Thermodynamic soundings for the 0730 case. . . . . 94
5.2 Profile of the merged DSD as a function of altitude, 0730 case. . . . . 95
5.3 Thermodynamic soundings for the 0812 case. . . . . 96
5.4 Profile of the merged DSD as a function of altitude, 0812 case . . . . . 97
5.5 Thermodynamic soundings for the 0815 case. . . . . 98
5.6 Profile of the merged DSD as a function of altitude, 0815 case . . . . . 99

5.7 Profiles of potential temperature $\theta$ . . . 100
5.8 Profiles of liquid water content LWC . . . 101
5.9 Profiles of rain rate $R$ . . . 102
5.10 Profiles of TKE dissipation rate $\epsilon$ . . . 103
5.11 Profile of total drop concentration $N_D$ . . . 104
5.12 Profiles of $d_{99}$ from merged mass DSDs. Colored markers (▲ for observations, + for CTRL runs, × for TURB runs) indicate cloud base, defined as $\overline{LWC(z)} > 0.05\,\mathrm{g\,m^{-3}}$. . . . 107
5.13 Profiles of $d_{99.9}$ from merged DSDs. Colored markers (▲ for observations, + for CTRL runs, × for TURB runs) indicate cloud base, defined as $\overline{LWC(z)} > 0.05\,\mathrm{g\,m^{-3}}$. . . . 109
5.14 Profiles of $d_{90}$ from merged DSDs. Colored markers (▲ for observations, + for CTRL runs, × for TURB runs) indicate cloud base, defined as $\overline{LWC(z)} > 0.05\,\mathrm{g\,m^{-3}}$. . . . 110

B.1 Profiles of longwave cooling rate . . . 119
B.2 Profiles of shortwave heating rate . . . 119
B.3 Profile of longwave cooling rate, 0730 case . . . 120
B.4 Profile of shortwave heating rate, 0730 case . . . 121
B.5 Relative difference of integrated longwave cooling, 0730 case . . . 122
B.6 Relative difference of integrated shortwave heating, 0730 case . . . 123

# List of Tables


2.1 Model details . . . . . 17
2.2 Intrinsic and extrinsic variables examined . . . . . 23

3.1 Microphysical characteristics of POST flights subdivided by flight leg. . 41

4.1 Model configuration and settings for RAMS-LES. . . . . 61
4.2 Boundary conditions for each simulated case. . . . . 67
4.3 Cloud base and top heights for each simulation, defined as the first and last level with liquid water mixing ratio $\overline{q_l} > 0.01\,\mathrm{g\,kg^{-1}}$ . . . . . 71

**Abstract**

Observational and Modeling Studies of Collision-Coalescence in Marine Stratocumulus

by

Mikael K. Witte

Low clouds cover over a quarter of the planet's surface in the annual mean and exert a significant cooling effect on global climate. Despite their importance, the representation of such clouds in global circulation models remains a major source of uncertainty in projections of future climate. The lifetime of such clouds can be modified by precipitation, which is observed to occur 20-40% of the time in stratocumulus over the ocean [*Wood*, 2012]. The processes by which precipitation forms are also highly uncertain and accurate quantitative precipitation forecasting remains a grand challenge in meteorology. The goal of this research is to explore and evaluate the representation of clouds in observations and models of the atmosphere, with a focus on improving our understanding of the primary process responsible for liquid precipitation formation, collision-coalescence.

The first goal of this research is to develop a metric for the dynamical "age" of small cumulus for use in contexting *in situ* observations. The lifetime of shallow cumulus is typically under an hour hence the metric must be accurate for a single measurement of the cloud. It is found that the deviation of cloud total water mixing ratio from the mean surface mixed layer total water mixing ratio is an effective measure because the mechanism by which total water mixing ratio is diluted, entrainment, is irreversible.

Collision-coalescence is notoriously difficult to observe *in situ* and its implementation in models of the atmosphere is highly uncertain because it is an inherently local process, dependent on interactions of drops on length scales as small as micrometers. The second goal of this dissertation is to assess the ability of theoretically derived collision-coalescence rates to explain observations of cloud drops in marine stratocumulus off the coast of Monterey, California. Drop size spectra averaged over length scales of 1.5

and 30 kilometers are found to require enhancements of collision rates that vary as a function of the mode of the drop size distribution from $10^{-1}$ for the largest mode sizes to over 20 for the smallest sizes. Unresolvable small-scale variability in the DSD is likely a major factor in determining the spread in required enhancements.

The third goal of the research presented herein is to implement a high spectral resolution bin microphysics scheme in a large eddy simulation (LES) model. The high resolution scheme is validated by comparison with simulations using the default spectral resolution. Considerable differences in microphysical structure and planetary boundary layer turbulence are found when collision-coalescence is active due to artificial acceleration of the process at the default resolution, which causes higher concentrations at large drop sizes than in the high resolution configuration.

Finally, the fourth goal of this research is to evaluate the ability of a turbulent collision kernel to improve the representation of precipitation formation. The net effect of the turbulent kernel is to deplete the cloud top of large drops, but the effect of this varies depending on total drop concentration such that precipitating and non-precipitating cases have opposite responses. Precipitating cases experience an enhanced sedimentation flux throughout the boundary layer at default resolution, while nonprecipitating cases and high spectral resolution simulations experience further suppression of precipitation. We conclude that the effects of changing spectral resolution dominate the effects of the turbulent kernel. This finding is contingent on the assumption that microphysical boundary conditions (i.e. cloud condensation nuclei concentrations) should be constant across spectral resolution configurations.

To Rachel,

For keeping my feet on the ground and reminding me to pull my head out of the clouds every now and then.

# Acknowledgments

This thesis has been a long labor of love for me, slowly put together over the past 4 years as the various pieces have fallen into place. I must first acknowledge my advisor, Dr. Patrick Chuang, who gave me the opportunity to undertake this endeavor in the first place. Our working relationship has evolved greatly over the last few years, from student-teacher to mentor-mentee to co-collaborators. I especially appreciate your patience during my "only student" phase, when you weathered more than your fair share of "freak out" emails that should otherwise have gone to labmates. It's been a joy learning both from and with you and I look forward to continued exchange of ideas, conversation, good meals and the occasional carbonated beverage.

Next I'd like to thank the remainder of the reading committee, Professors Nic Brummell and Xi Zhang, for their time, energy, and guidance over the years. A special thanks as well to Dr. Gary Glatzmeier and Professor David Romps for serving on my qualifying committee, and to Gary again for further conversations about my career and future at the annual committee meetings.

Beyond the committee, each project I've worked on has been influenced, guided, and developed in collaboration with many others. My earliest collaborator was Dr. Dione Rossiter, who played an invaluable role in my transition from student to scientist. Thank you for taking the time to introduce me to UCSC and the atmospheric science community and for giving me a 5 year head start on Matlab coding. I'm proud to have built on the foundation laid by your work. Dr. Graham Feingold has been an immense influence throughout the years, beginning with our work on the "cloud clock" project and more recently during my LES work, for which Dr. Feingold generously provided code for the RAMS microphysical scheme (Tzivion high resolution collision-coalescence subroutines and kernel coefficient generation algorithm, analytical method of moments condensation/evaporation subroutines) and help understanding all of it. Coincidentally, he also wrote much of the bin microphysics code I use during his own PhD studies. Dr. Jonathan Petters was responsible for my introduction to the vast world of atmospheric modeling, including all the underlying knowledge about how to use computers effec-

tively and keep my output organized (I'm still working on both). Dr. Orlando Ayala provided encouragement, code, technical support with my OpenMP implementation in RAMS, and his deep knowledge. I accomplished more coding in the 4 days of his 2015 visit than I typically get done in a month. I also thank Dr. Lian-Ping Wang for his knowledge and collaboration over the past 4 years. Finally, thanks to Dr. Haflidi Jonsson and the staff and pilots at the Center for Interdisciplinary Remotely-Piloted Aircraft Studies (CIRPAS) for the CIRPAS Twin Otter observations used in Chapters 3-5 of this dissertation, which are freely available through the UCAR Earth Observing Laboratory (http:\\data.eol.ucar.edu\master_list\?project=POST).

The early part of my graduate career involved a number of small projects not mentioned in this thesis, but which must be recognized for the role they played both in my education and in providing funding for my studies. Dr. Ian Faloona of UC Davis provided funding for me during the summer of 2011 to design and implement a meterological monitoring station at Chews Ridge near Carmel Valley, CA. The Office of Naval Research funded our deployment to Diego Garcia to participate in the DYNAMO project from 2011-2012. I also recognize Dr. Nick Guy, whom I met through DYNAMO-related work, for the opportunity to collaborate and get to know one another.

The text and figures of Chapter 2 were previously printed in a peer-reviewed journal: M. K. Witte, P. Y. Chuang, and G. Feingold, "On clocks and clouds," **Atmospheric Chemistry and Physics**, published online July 3, 2014 (doi:10.5194/acp-14-6729-2014). Hongli Jiang ran the simulations used for the analysis. The first co-author listed in the publication (Patrick Chuang) directed and supervised the research which forms the basis for the dissertation. The second co-author (Graham Feingold) provided the simulation output and participated in interpreting the results of the research. I performed the data analysis, produced the figures and wrote the manuscript for Witte, Chuang and Feingold [2014].

My work related to the turbulent collision-coalescence kernel (Chapters 3-5) was generously funded by the National Science Foundation under Grant No. AGS-1139746.

# Chapter 1

# Introduction

Clouds are the visible expression of the continual exchange of heat and moisture between the surface and the atmosphere, the signature of the thermodynamic process of condensation crucial to closing the hydrological cycle. Where clouds occur and how vigorously they return moisture to the surface via precipitation have been matters of obsession for humanity since at least the rise of agriculture [*Anderson*, 2005]. Beyond the hydrological cycle, clouds also play an important role in the earth's radiative balance because of their high albedo relative to the oceans and non-icy land surfaces. Understanding the processes by which clouds evolve has wide-ranging effects on our ability to predict weather and climate, which in turn affect a plethora of human activities, from agriculture to aviation; planning a trip to the beach to planning for future generations.

Human activites also affect clouds, directly and indirectly. On shorter time scales, anthropogenic emissions of aerosols in the form of ship tracks, smoke stacks, and jet exhaust serve as condensation nuclei that extend the lifetime of clouds or even cause them to form in places they wouldn't otherwise. Over longer time scales and primarily due to emission of greenhouse gases, our activities can change patterns of sea surface temperature and large-scale atmospheric circulation to favor certain cloud types over others, with far-reaching effects and climate feedbacks in response. Understanding how clouds respond to such forcings is a primary goal of cloud physics.

Clouds come in many different "flavors," occurring at different heights in the at-

mosphere, some precipitating and some not, composed of differing amounts of liquid and solid condensate and existing over durations as short as a few minutes to as long as months on end. Such variability arises because clouds are emergent phenomena; their existence is intimately tied to the diurnal cycle of solar heating and the turbulent flow of the atmosphere, which occurs across length scales spanning many orders of magnitude. In fact, cloud processes cover an even greater range of scales, from the sub-micrometer scale of the smallest condensation nuclei to the scale of the largest synoptic weather systems, which can cover thousands of kilometers.

The multiscale, turbulent nature of clouds renders them difficult to comprehensively observe and represent in models of the atmosphere. In particular, clouds remain one of the leading sources of uncertainty in projections of future climate [*IPCC*, 2013]. The multiscale issue is not the only difficult aspect of modeling clouds; the diversity of relevant processes that must be taken into account is staggering. Simulating clouds involves accurately representing aerosol chemistry, radiation physics, thermodynamics, chaotic fluid flows over complex topography, surface fluxes and cloud microphysical processes. The complexity of representing clouds is further augmented by the couplings and feedbacks between the various processes, many of which are poorly understood. This work specifically focuses on the coupling of turbulence and one specific cloud microphysical process, collision-coalescence, in marine stratocumulus.

## 1.1 Overview of marine stratocumulus

Stratocumulus is the most prevalent cloud type on the planet by areal coverage. In the annual mean, over a fifth of the planet is covered by these clouds with the majority of the coverage occurring near the eastern margin of cold subtropical and tropical oceans [*Wood*, 2012]. Marine stratocumulus (MSc) most often form in the descending branch of the Hadley and Walker circulations, where they exist as semipermanent cloud decks that can persist for weeks to months on end, as well as forming more transiently in the midlatitudes in cold and/or subsiding regions behind baroclinic systems and in the

undisturbed Arctic region [*Wood*, 2012]. Boundary layers conducive to full cloud-cover conditions are typically confined to at most about a kilometer in depth [*Albrecht et al.*, 1995], so the effective radiative temperature of the clouds capping such boundary layers is close to that of the surface while their albedo is in the range $0.4 \lesssim \alpha \lesssim 0.8$ – much higher than the ocean surface (typical $\alpha \approx 0.1$). The combination of high radiative temperature and high albedo means that MSc radiate in the thermal infrared (or longwave) band at about the same rate as the surface while reflecting a large fraction of incident solar (shortwave) radiation. Therefore they exert a significant cooling effect versus clear sky conditions, approaching $-100\,\mathrm{Wm}^{-2}$ during peak cloud cover conditions [*Klein and Hartmann*, 1993]. To put the magnitude of this cooling effect into perspective, *Slingo* [1990] estimates that an increase in global stratocumulus coverage of only $3-5\%$ would be sufficient to offset the radiative forcing of anthropogenic greenhouse gas emissions.

The dynamics of stratocumulus formation differ considerably from those of the canonical cumulus cloud. Whereas cumulus formation is driven from the surface by solar heating, stratocumulus tend to form in areas of strong lower-tropospheric static stability where convective instability is instead initiated from the top down by longwave radiative cooling. In the classic subtropical marine setting, synoptic-scale subsidence causes warm, dry descending air to form a thermal inversion atop the marine boundary layer. The upper reaches of the moist, cool underlying boundary layer are then able to radiatively cool to space until the air at the top of the boundary layer is denser than the air below. A sort of upside-down circulation then sets up: cool, dense parcels descend from cloud top and allow warmer ones to replace them, only for those new parcels to again begin cooling as they near the inversion. The turbulence induced by this circulation and latent heat release couples the cloud layer to the ocean surface, providing a source of moisture, but also causes entrainment of the overlying warm, dry free tropospheric air through the inversion layer, leading to cloud top evaporation. While the cloud top longwave cooling rate is primarily determined by sea surface temperature (assuming a relatively well-mixed boundary layer), the net cooling rate also depends

on solar heating. Thus the summertime diurnal cycle of stratocumulus with which coastal California residents are familiar: stratocumulus coverage peaks during the early morning hours, followed by thinning or complete dissipation as absorption of solar radiation offsets longwave cooling during the day, and a return of cloud cover in the evening as solar heating wanes.

In non-precipitating stratocumulus evaporation due to entrainment is the primary sink of moisture, yet drizzle is observed in the persistent subtropical stratocumulus regions 20-40% of the time [*Leon et al.*, 2008; *Wood et al.*, 2009] and therefore cannot be ignored. For our purposes we will consider the rain rate to be defined as the integrated sedimentation flux of all drops in a parcel in units of millimeters per day. The terms precipitation, rain and drizzle will be used interchangeably since only warm (i.e. ice-free) clouds are considered here. The precipitation rate of stratocumulus is usually characterized by the value at cloud base, where typical rates in drizzling clouds range from 0.5 to 2 mm day$^{-1}$ [*Wood*, 2012]. Despite such relatively lackluster rates as compared to cumulus-type clouds, where rain rate is usually measured in centimeters per hour, the latent heat release from drizzle production in a moderately precipitating cloud ($R \sim 1$ mm day$^{-1}$) is of comparable magnitude to the cloud top radiative cooling rate, or about 30 Wm$^{-2}$. Hence drizzle is a leading-order term in the energetics of precipitating stratocumulus.

Beyond precipitation's effect on the cloud layer itself, it can also change the dynamics and structure of the boundary layer via subcloud evaporation [*Stevens et al.*, 1998]. As rain falls from cloud base into the subsaturated region below, evaporation causes cooling and therefore stratification of the boundary layer. This can cause decoupling of the cloud layer from the surface source of moisture and promote either cumulus convection below stratocumulus or complete dissipation of the cloud layer.

## 1.2 Microphysical processes in warm clouds

Cloud microphysics is the study of the evolution of the particles (liquid or solid) that make up a cloud. The population of drops is described by the drop size distribution (DSD) which gives the concentration of drops as a function of some measure of size, $N(x)$. In both observations and models, the DSD must be discretized and in order to compare DSDs with different discretizations, the DSD is often normalized by bin width. Here we use spherical particle diameter $D_p$ as the measure of size and normalize by the base 10 logarithm of bin width, $dlog_{10}D_p$, such that the DSD is presented as $dN(D_p)/dlog_{10}D_p$. The particle diameter subscript $p$ is occasionally omitted for visual clarity. As only liquid phase clouds are considered, any processes related to solid condensate may be neglected and cloud particles will be referred to as drops or droplets. The physical processes operating in warm clouds include activation of cloud condensation nuclei (CCN), condensation, collision-coalescence, evaporation and drop breakup. The breakup process is only important in heavily precipitating clouds where the largest drops exceed several millimeters in diameter and will not be included in any of the analyses or modeling studies that follow. Each process is qualitatively described below followed by a general overview of theories of precipitation initiation in warm clouds.

As air is cooled to the dewpoint temperature, it becomes supersaturated with respect to water vapor and cloud drops begin to form. Nucleation of drops from pure water vapor requires supersaturations far beyond what is observed in earth's atmosphere therefore the formation of a cloud drop begins with the activation of a condensation nucleus onto which a drop will grow. Aerosols (suspended particulate matter) serve as these nuclei. Aerosols of all sizes and compositions are able to serve as condensation nuclei given a high enough supersaturation, but species that are water-soluble and hygroscopic are preferentially activated; it is these species that are thought to dominate the CCN spectrum [*Pruppacher and Klett*, 1997]. Activation is not only a function of composition, though. It also depends on the particle radius of curvature such that smaller CCN require a higher supersaturation to be activated given the same chemical composition. Over the oceans,

the most common naturally occuring CCN species are sea salts and sulfates while combustion byproducts such as those responsible for ship tracks are also important locally. The concentration of CCN over the ocean is generally from a few tens to a few hundreds per cubic centimeter, although it can be as high as thousands per cubic centimeter in the vicinity of ship tracks or if there is a continental particulate source nearby. Note that from the microphysical perspective, "polluted" means high aerosol concentration. Most activation in stratocumulus takes place near cloud base, though so-called "secondary activation" near cloud top as a result of entrainment mixing also occurs.

Once drops have been activated, their initial growth is by direct diffusion of water vapor from the immediate surrounding environment. The rate of condensation depends directly on the local supersaturation and inversely on drop size. As such, condensation necessarily slows as a drop grows larger given a constant supersaturation. Under normal conditions the maximum size drops can achieve by condensation alone is about 20-30 μm in diameter [*Pruppacher and Klett*, 1997]. In reality, the theoretical maximum drop size is not always reached; this is common in polluted clouds where even in a thick cloud layer the activation of a large number of CCN limits the supersaturation available for condensation.

Collision-coalescence is the primary process responsible for transforming small cloud drops into rain drops, and the main focus of this work. Consider a uniformly distributed bidisperse population of drops in a quiescent atmosphere. The drops fall at their terminal velocity, which is a monotonically increasing function of drop mass for the size range relevant to MSc, such that the larger drops fall faster than the smaller drops. A large drop will eventually come into contact (collide) with a smaller drop and if the drops merge (coalesce), the large drop grows and is said to have "collected" the smaller drop. The rate at which collision-coalescence occurs can be expressed by the geometric collection kernel, given here in terms of drop radius for clarity:

$$K(r_1, r_2) = E_{coll} E_{coal} \pi (r_1 + r_2)^2 \left| \mathbf{v_2} - \mathbf{v_1} \right| \tag{1.1}$$

where $K$ is the rate of collisions between drops of radius $r_1$ and $r_2$, $E_{coll}$ and $E_{coal}$ are the efficiencies of collision and coalescence, respectively, and $\mathbf{v}$ is drop velocity. The collision and coalescence efficiencies describe particle-particle interactions and are also a function of drop sizes $r_1$ and $r_2$, although the coalescence efficiency is assumed to be unity in most formulations of the kernel (i.e. all collisions result in coalescence). Generally, collision efficiency is very low for small drops such that collision-coalescence is not particularly effective until drops exceed 50-60 μm in diameter. Drops larger than 50 μm grow very efficiently by collision-coalescence. In some cases, the collision efficiency can exceed unity because of phenomena like wake capture; this is most often the case for interactions between large drops ($D \gtrsim 300\,\mu\text{m}$) . The paradox of how drops grow from the maximum size reached by condensational growth ($D \sim 20-30\,\mu\text{m}$) to the minimum size for effective collision-coalescence to produce precipitation on observed time scales remains one of the basic outstanding questions of cloud physics.

The final process we must take into account to explain the evolution of cloud drops in marine stratocumulus is evaporation. While from the most basic standpoint evaporation is simply the reverse of condensation, the application of a given evaporative forcing to a population of drops is complicated by cloud top entrainment. Condensation is nearly always assumed to be spatially homogeneous in nature; in other words, all drops in a volume experience the same supersaturation. Even near cloud base, though, this assumption is not strictly true since the supersaturation field varies due to fine-scale turbulent fluctuations in vertical velocity [*Devenish et al.*, 2012]. In the case of evaporation, on the other hand, entrainment results in subsaturated filaments of free tropospheric air penetrating the cloud top such that large gradients in vapor forcing can occur across relatively small length scales (sub-meter). If the time scale of mixing is short enough that a cloudy volume becomes fully mixed before drops can equilibrate, all drops experience the same subsaturation, equivalent to the homogeneous approach assumed in the condensation process. In this case, all drops are reduced in size but only the smallest drops completely evaporate. On the other hand, if we assume the time scale of mixing is very long, drop evaporation may be so much faster than mixing that

some drops evaporate completely while others experience no subsaturation at all. This is termed "extreme inhomogeneous mixing" and results in the loss of some drops at all sizes (assuming uniform spatial distribution), but no substantial change in the shape of the DSD. In reality, mixing falls somewhere in between the homogeneous and extreme inhomogeneous end members depending on the ambient conditions, but most numerical models (including those employed here) assume homogeneous mixing for evaporation.

### 1.2.1 Theories of precipitation formation

The average drop in a shallow cloud has diameter of order 10 μm, yet rain drops observed at the surface are often larger than a millimeter. Droplet growth over 3 orders of magnitude in diameter must be accomplished in time scales as short as 20 minutes, but none of the processes outlined above are able to open the process rate bottleneck between condensation and collision-coalescence in the diameter range from about 20 to 60 μm. This issue was first recognized in the study of precipitating shallow cumulus because cloud-resolving models were unable to produce precipitation on observed time scales [see *Beard and Ochs*, 1993, for a detailed account]. Discrepancies are also noted in large-scale models (e.g. global circulation models), where process rates relevant to the onset of collision-coalescence must be arbitrarily increased by factors exceeding an order of magnitude to agree with observed precipitation rates [*Pincus and Klein*, 2000]. There are several hypotheses that have been proposed to solve the so-called "warm rain problem:" (1) the existence of ultragiant aerosols that seed the first large drops; (2) turbulent mixing of drops of differing vapor forcing histories; and (3) augmentation of collision-coalescence rates by turbulent air motions and particle-particle interactions. The common thread between each of these hypotheses is that they broaden the DSD, which in turn promotes collision-coalescence growth. A brief summary of each hypothesis follows.

### Giant and ultragiant aerosol

Giant ($1 < r < 10\,\mu m$) and ultragiant ($r > 10\,\mu m$) CCN (GCCN and UGCCN, respectively) are perhaps the most straightforward solution to the warm rain problem since such particles essentially activate into being collisionally-active drops. Because they activate before smaller particles, they can decrease the total number of particles activated and allow those that are activated to grow to larger sizes by condensation [*Johnson*, 1982]. In addition, the concentration of UGCCN is usually several orders of magnitude lower than the smaller, more numerous accumulation mode aerosol ($0.01 < r < 1\,\mu m$) which means that the size differential between the activated ultragiant particles and other drops is exaggerated, thereby accelerating collision-coalescence. While this hypothesis has been shown to be feasible in some modeling studies of shallow cumulus [*Cooper et al.*, 2013], the low concentration at which UGCCN occur makes it difficult to observe them. Furthermore, simulations of stratocumulus by [*Feingold et al.*, 1999] showed that higher overall CCN concentrations required comparably higher UGCCN concentrations to increase drizzle production, which has not been corroborated by the observations. This hypothesis appears to be more relevant in shallow cumulus and continental stratocumulus than for marine stratocumulus, an interpretation reinforced by other recent studies [e.g. *Reiche and Lasher-Trapp*, 2010; *Dagan et al.*, 2015].

### Turbulent mixing

Turbulent mixing is hypothesized to accelerate drizzle production by causing parcels with different supersaturation histories to interact. In the absence of such mixing, the liquid water content (LWC) of a parcel will closely follow a moist adiabat as it ascends. Fluctuations in the water vapor mixing ratio and vertical velocity fields cause variability in the lifting condensation level and therefore in LWC and the DSD without appealing to mixing. The majority of the heterogeneity introduced by turbulent mixing is instead thought to be caused by entrainment at cloud top, where the DSD is broadened by interaction of relatively undilute parcels with others that have undergone varying degrees of evaporation, which leads to faster collision-coalescence growth by broadening the

DSD. The concept of extreme inhomogeneous mixing described above was originally proposed to explain how entrainment mixing could broaden the DSD without reducing mean drop size [*Baker and Latham*, 1979]. A recent study by *Magaritz-Ronen et al.* [2016] pointed out that turbulent mixing may actually slow the onset of collision-coalescence because many of the "new" drops introduced from a diluted parcel are smaller than those in an undiluted parcel and furthermore that the most collisionally-active DSDs in their simulations were those that were least affected by entrainment (i.e. closest to adiabatic). Despite this retarding effect of mixing, *Magaritz-Ronen et al.* [2016] still found it was necessary for drizzle production because of secondary effects of turbulent mixing on aerosol processing and moistening of extremely dry entrained parcels, which prevented the initial growth of large drops in simulations without mixing. On the other hand, modeling work by *Yang et al.* [2016] showed that some parcels may experience super-adiabatic drop growth after entrainment events, thereby enabling drops to grow larger than the generally accepted upper limit of $d \approx 20 - 30\,\mu\text{m}$. The pathways to accelerate drop growth by turbulent mixing are numerous and will require further study to develop a consistent narrative.

**Turbulent collision-coalescence**

Collision-coalescence was described above in the limit of quiescence, but in reality clouds always exhibit some level of turbulence. The role of turbulence in collision-coalescence was already recognized 80 years ago; *Arenberg* [1939] was first in the literature to suggest that turbulence may directly increase collision-coalescence rates, followed by a decade or so of mostly qualitative study on the topic. Pioneering papers by *East and Marshall* [1954] and *Saffman and Turner* [1956] began the effort to quantify turbulent collision-coalescence, with *Saffman and Turner* [1956] introducing the parameterization of turbulent effects as a function of the turbulent kinetic energy (TKE) dissipation rate $\epsilon$. In the 60 years since, numerous workers in both the cloud physics and fluid dynamics communities have pursued the problem of collisions in multiphase turbulent flow with an increasingly sophisticated array of tools. Quantitative studies through

the 1970's and 80's such as *deAlmeida* [1976] and *Maxey* [1987] addressed the topic from a theoretical perspective, but by the 1990's sufficient computational power became available to directly simulate turbulent flows with settling particles. Direct numerical simulation (DNS) studies [e.g. *Ayala et al.*, 2008a] explicitly represent a turbulent flow field, and the parameterization of the collision kernel is developed by evaluating the statistics of drop collisions at a given value of $\epsilon$. The main drawbacks of such studies are that they are often performed using an unrealistically simple bidisperse drop population and the maximum Reynolds number attained is usually orders of magnitude lower than that of the atmosphere due to computational limitations.

Turbulence has three main effects on the collision-coalescence process: (1) drops in a turbulent flow affect the flow fields experienced by other drops, thereby modulating collision efficiency [*deAlmeida*, 1979a; *Pinsky et al.*, 1999, 2007; *Wang et al.*, 2008]; (2) turbulent air motions alter drop trajectory by introducing transient nongravitational accelerations, with the potential to increase or decrease the relative velocity term of the collision kernel [*Maxey*, 1987; *Squires and Eaton*, 1990; *Pinsky and Khain*, 1997b; *Shaw and Oncley*, 2001]; and (3) drops preferentially cluster in areas of low shear, violating the assumption of uniform spatial distribution [*Wang and Maxey*, 1993a; *Pinsky and Khain*, 1997a; *Sundaram and Collins*, 1997; *Reade and Collins*, 2000; *Kostinski and Shaw*, 2001; *Saw et al.*, 2008]. Each of these terms are dependent on drop size and the dissipation rate; there is what may be termed a "Goldilocks zone" in drop size where drops experience maximal deviations from the environmental flow (not too small) yet sediment slowly enough that intermittent turbulent accelerations still have a major effect on drop trajectory (not too big). Under normal turbulent conditions in stratocumulus ($0 < \epsilon \lesssim 10^3\,\mathrm{cm^2 s^{-3}}$) this "Goldilocks zone" (just right) encompasses the process bottleneck size range from approximately 30 to 60 μm in diameter [cf. Figure 1, *Devenish et al.*, 2012].

## 1.3 Summary

The original goal of this thesis was to explore whether turbulence is able to cause effectively cause precipitation formation in MSc, but as with any interesting question, the initial questions we set out to answer led us down unexpected paths. Therefore this thesis has come to be more broadly defined as an exploration of the representation of clouds and cloud microphysical processes in both observations and models of the atmosphere, with a particular focus on collision-coalescence.

The remaining chapters are presented as independent manuscripts with the exception of Chapters 4 and 5, as the modeling framework and case studies developed in Chapter 4 are utilized in Chapter 5. As such, each chapter contains relevant background information, literature review, a detailed description of methods, presentation of results, and discussion of findings. In Chapter 2, the life cycle of shallow cumulus is characterized from large eddy simulation (LES) output to develop an observationally-feasible metric of cloud age from a single measurement; this is the only chapter not devoted to MSc. Chapter 3 develops an analytical framework for estimating collision-coalescence rates from observed drop size spectra and applies the analysis to observations of MSc to test the explanatory power of various theoretical collision kernels and the role of spatial averaging length on DSD representation. Chapter 4 details the implementation of a high spectral resolution bin microphysics scheme in LES and validates the high resolution scheme via simulations of three observational case studies. Chapter 5 utilizes the high resolution microphysics scheme and implements a turbulent collision kernel to generate drop size distributions for comparison with observations using the same case studies developed in Chapter 4. Finally, Chapter 6 concludes the dissertation.

# Chapter 2

# On Clouds and Clocks

## 2.1 Introduction

Looking at the sky reveals immense variability in the properties and evolution of clouds, even those adjacent to one another. Variance among clouds is due not only to spatial variability in quantities such as temperature and humidity, but also to temporal variability, i.e. differences in cloud age. Fortunately, the overall evolutionary arc of clouds is roughly predictable. Shallow, warm cumulus begin as a pulse of positively buoyant air rising up through the boundary layer. As the cloud ages, the liquid water depletion processes (namely entrainment and precipitation) govern cloud dissipation. Past analyses of *in situ* observations have implicitly assumed that temporal variance is minimized by random sampling of many clouds of unknown age to paint a picture of an "average-aged" cloud. Yet inherent to cumulus evolution are distinctive stages defined by the different physical processes active during each. Knowing the age of a cloud then gives insight into which processes are expected to be most important at the time of observation. Furthermore, using *in situ* observations of cumulus to explore cloud-aerosol interactions or test theory is more meaningful if cloud age is known because it allows for testing representations of cloud mechanics at the process level. In his essay *Of Clouds and Clocks*, the philosopher Karl Popper presents clouds as a probabilistic,

nonlinear system:

> "My clouds are intended to represent physical systems which...are highly irregular, disorderly, and more or less unpredictable... On the other extreme...we may [consider] a very reliable pendulum clock, a precision clock, intended to represent physical systems which are regular, orderly, and highly predictable in their behaviour." [*Popper*, 1972]

While it is effectively impossible to predict a priori where an individual cumulus cloud will form or exactly how long it will last, all cumulus follow the same general progression as described above. Given this common framework for cloud evolution, the question then is whether there exists an orderly, predictable clock that is applicable to an unruly cloud population. Observing the evolution of individual clouds in a field of cumulus is challenging. Because cumulus have an average lifetime of less than an hour [*Jiang et al.*, 2006; *Dawe and Austin*, 2011], estimating their age requires repeated observations every ~5 min. Ground-based remote sensors such as radar are capable of sampling at this frequency, but sacrifice sample volume in order to repeat quickly. Even with a 5 min repeat cycle, it may not be easy to accurately track clouds from one scan to the next. Reducing sample volume also increases the risk that clouds will depart the volume before the end of their lifetimes. Furthermore, scanning radar must contend with decreasing spatial resolution at increased distance from the sensor [*Fielding et al.*, 2013]. Lastly, cloud radar can not always accurately deduce critical cloud properties such as cloud liquid water content because measurements are strongly sensitive to the concentration of the largest drops, which is not necessarily correlated with other properties of interest. Nonetheless, cloud radar is likely the most effective observational tool for studying the life cycle of cumulus clouds. Satellites have even stricter limitations for cloud life cycle studies. Geostationary satellite data is currently available at 15 min intervals at best, with horizontal resolution of 1 km in the visible and 4 km in the IR spectrum for GOES. Such long repeat cycles and coarse spatial resolution make such observations unsuitable to examine small cumulus, but are appropriate for studying larger, longer-lasting clouds such as stratocumulus or deep cumulus. Satellites also have a limited arsenal of measurements: primarily droplet effective radius, cloud

fraction, and cloud optical depth. Liquid water path (LWP) can be derived from the cloud optical depth and drop effective radius with the assumption of a liquid water content (LWC) profile. Aircraft are able to make repeated measurements (1-2 min repeat cycle) of the same cloud, but given limits on flight time, repeated observation of just a few targets necessarily limits the ability to compile statistics of a cloud field. Multiple observations also rely on an a priori assumption of cloud age, i.e. the cloud of interest must be young. If the cloud is first observed while dissipating, there may be nothing left for further observation. One key advantage of aircraft is the ability to measure a wide range of relevant cloud properties (temperature, LWC, drop size distribution, turbulence, etc.), but poor understanding of the temporal and spatial context of these measurements is a key limitation. Our goal for this study is to assess whether there exists a method to infer the age of a cloud based on a single observation of that cloud. We define a good cloud "clock" as an observable quantity that assigns age based on a measurement at a single moment in time, regardless of the cloud's history. The most easily observed quantity, time elapsed since cloud nascence, is problematic. Time elapsed is an initial time subtracted from the present time, violating the requirement that age be determined from one measurement. Individual clouds vary greatly in lifetime, even those in close proximity to each other, due primarily to variations in the forcings and environment that each experiences. A 15-min-old cloud could be growing or dissipating. Thus, elapsed time alone provides ambiguous information about what is occurring at the process level. Instead, age is more readily framed in terms of cumulus life cycle phases: growth, maturity and dissipation. During the growth phase, the cloud increases in size, mostly in the vertical direction. As the cloud matures, the rate of growth slows and reverses; any precipitation that develops is strongest during this period. Finally, the cloud dissipates due to a combination of entrainment and precipitation reducing liquid water, while the lack of dynamical support shuts down the production of new liquid water. In order to accommodate clouds of different lifetimes, we use a non-dimensional time $t/\tau$, where $\tau$ is cloud lifetime. All clouds are born at $t/\tau = 0$ and all clouds have fully dissipated by $t/\tau = 1$. If it were possible to follow a cloud in real time, such that birth and dissipation

times were known, non-dimensional time would be an excellent candidate for the ideal cloud clock. Even this measure, though, is not perfect. Cloud life phases do not take equal amounts of non-dimensional time – the dissipation phase can happen gradually or catastrophically; rejuvenating pulses of buoyant air can occur in existing clouds, essentially reverting lucky clouds to the youthful growth phase [*Heus et al.*, 2009]. Exploring whether a useful cloud clock exists is most easily achieved through the use of large eddy simulation (LES) of shallow cumulus fields to follow a diverse population of clouds over the course of their lifetime, from birth to dissipation. This allows evaluation of a wide range of potential clock candidate variables over the lifetime of numerous clouds with a focus on what can be measured *in situ* by aircraft. Some remotely-sensed quantities such as liquid water path can also be deduced from model output. The description of cloud life phases above is most applicable to clouds that experience a single buoyancy pulse. However, some clouds experience multiple buoyancy pulses. Subsequent pulses cause ambiguity because growth in the lower part of the cloud can occur simultaneously with dissipation in the upper part of the same cloud. Thus no single life phase description is applicable. Despite these challenges, it still appears worthwhile to evaluate the possibility of estimating cloud age from a "snapshot" observation. One important application is to approximately classify aircraft-observed clouds by life phase. We emphasize that to be useful, a clock need not be perfect; misclassifcation of some clouds is acceptable if most clouds are appropriately characterized.

## 2.2 Methodology

The study uses previously-reported three-dimensional LES of trade wind cumulus based on cases from the Barbados Oceanographic and Meteorological Experiment [*Xue and Feingold*, 2006a, BOMEX] and the Rain in Cumulus over the Ocean experiment [*Jiang et al.*, 2009, RICO]. The BOMEX simulations are further subdivided into clean and polluted cases. The models and relevant model parameters are described in Table 2.1 and environmental soundings are given in Figure 2.1. Both models use periodic

| | BOMEX Clean | BOMEX Polluted | RICO |
|---|---|---|---|
| Model | UCLA-LES | | Adapted RAMS |
| Grid $\Delta x$, $\Delta y$, $\Delta z$, m | 100, 100, 40 | | 50, 50, 20 |
| Domain $x$, $y$, $z$, m | 6400, 6400, 3000 | | 6400, 6400, 4000 |
| Cell size, $m^3$ | $4 \times 10^5$ | | $5 \times 10^4$ |
| Horizontal buffer, m | 200 | | 100 |
| $\Delta t$, s | 1.5 | | 1.5 |
| Simulation time, h | 6 | | 6 |
| $N_a$, $cm^{-3}$ | 25 | 2000 | 100 |
| Graph trace | Solid | Dash | Dash-dot |

Table 2.1: Model details

boundary conditions and are initiated with instantaneous pseudo-random temperature perturbations near their lowest levels. The first 3 hours of each simulation are discarded as spin-up. Individual clouds are manually tracked over the course of their lifetime. For an overview of small cumulus evolution in LES, see *Dawe and Austin* [2011]. A cloudy cell is defined as having liquid water content greater than $5\text{x}10^{-2}$ g $kg^{-1}$ and a clear air cell is defined by LWC less than $1\text{x}10^{-18}$ g $kg^{-1}$. Any value between the thresholds is excluded from analysis, which accounts for <1% of all cells. Cloud lifetime is defined to be the elapsed time during which the cloud comprises at least 5 contiguous cloudy cells such that clouds may initially form as a small number of nonadjacent cells. We define "contiguous" as sharing an adjoining face. Clouds were chosen such that a clear-air buffer exists around them throughout their lifetime to maintain individual cloud identity. The buffer zone ensures a given cloud will not merge with any other cloud. Clouds that split horizontally into fragments and clouds with a minimum mature phase vertical extent of less than 200 m are also excluded from the study. Each cloudy and clear cell is characterized by the following values: total water mixing ratio $r_t$, liquid water mixing ratio or liquid water content LWC, potential temperature $\theta$, virtual potential tempera-

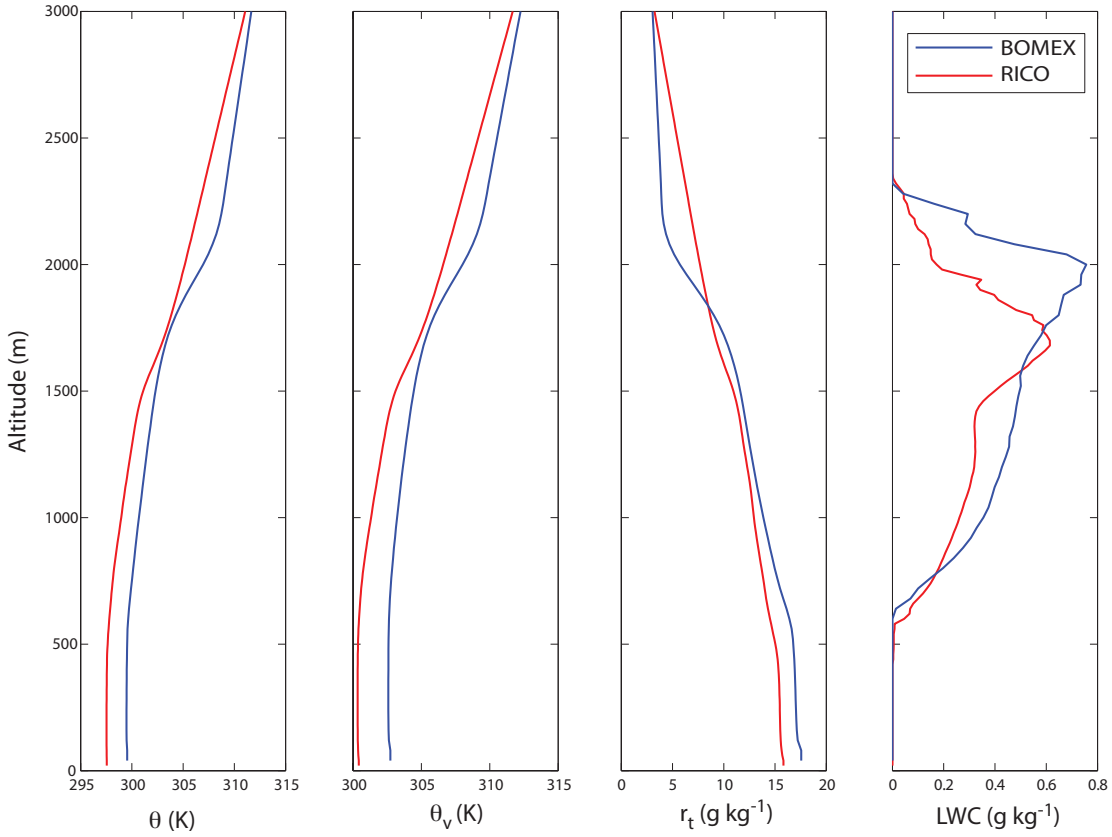



Figure 2.1: Environmental soundings taken over the period of time from which clouds are selected. With the exception of LWC, the profiles are clear-air domain averages.

ture $\theta_v$, and the resolved-scale vertical wind variance $\overline{w'^2}$ which is used as a proxy for turbulent kinetic energy. At each time step, the cloudy cell values are summed to give cloud total $r_t$, LWC, and $\overline{w'^2}$ as a preliminary step to computing cloud averages. The buoyancy perturbation $\Delta\theta_v$ is found by taking the difference between a cloudy value of $\theta_v$ and the clear air mean $\overline{\theta}_{v,clr}$ at the same altitude level. The value $\Delta\theta_v = \theta_v - \overline{\theta}_{v,clr}$ then is the buoyancy of cloudy air relative to the clear air around it. Positive values of cloud-average $\Delta\theta_v$ indicate positive buoyancy while negative values indicate the opposite, which on average are associated with rising and subsiding motion, respectively. In addition, some extrinsic properties of the cloud are determined: cloud volume, surface area, maximum cross-sectional area, depth, liquid water center of mass and liquid water

path. Volume is the sum of contiguous cloudy cells at all vertical levels. Surface area is calculated by counting the number of cloudy cell surfaces abutting non-cloudy cells. Depth is the maximum number of contiguous cloud-populated altitude levels. Center of mass is the sum over the entire cloud of altitude times liquid water mass at each altitude divided by the total liquid water mass of the cloud. Liquid water path is estimated as the cloud-integrated LWC divided by maximum cross-sectional area. To directly compare clouds of varying size and lifetime, we average the cloud total values by the extrinsic cloud properties listed above (cloud volume, surface area, etc.) and normalize time by cloud lifetime $\tau$. In addition to cloud-integated averaging, we derive altitude-specific variable averages to simulate an aircraft pass when cloud depth is greater than 200 m. Altitude averages were taken using normalized cloud height (where $z^* = 0$ corresponds to the instantaneous cloud base, $z^* = 1$ to the instantaneous cloud top) throughout the cloud. The normalized levels used are the nearest whole number altitude levels above cloud base ($z^* = 0.25$), at midcloud ($z^* = 0.5$) and below cloud top ($z^* = 0.75$). Since cloud base and top change over time, the single-level averages vary in absolute altitude over cloud lifetime.

## 2.3 Results and Discussion

### 2.3.1 The clouds

Overall, a total of twelve individual clouds are examined, four of which experienced a second buoyant pulse. Cloud lifetime ranges from 18 to 44 min and maximum volume ranges from $4 \times 10^7$ to $1.4 \times 10^8$ m$^3$ (Fig. 2.2). Cloud base was between 640 m and 680 m for both the BOMEX and RICO simulations. Typical mature-stage cloud depth is approximately 1200 m. Six of the clouds are from the "clean" BOMEX simulation, three are from the "polluted" BOMEX simulation, and three are from the "clean" RICO simulation. Of the twelve clouds, only one (cloud S in Fig. 2.2) exhibits a lifetime-averaged rain rate greater than 1 mm day$^{-1}$. As shown in Fig. 2.2, all clouds grew in volume from nascence until about $t/\tau \sim 0.3$, at which point single-pulse

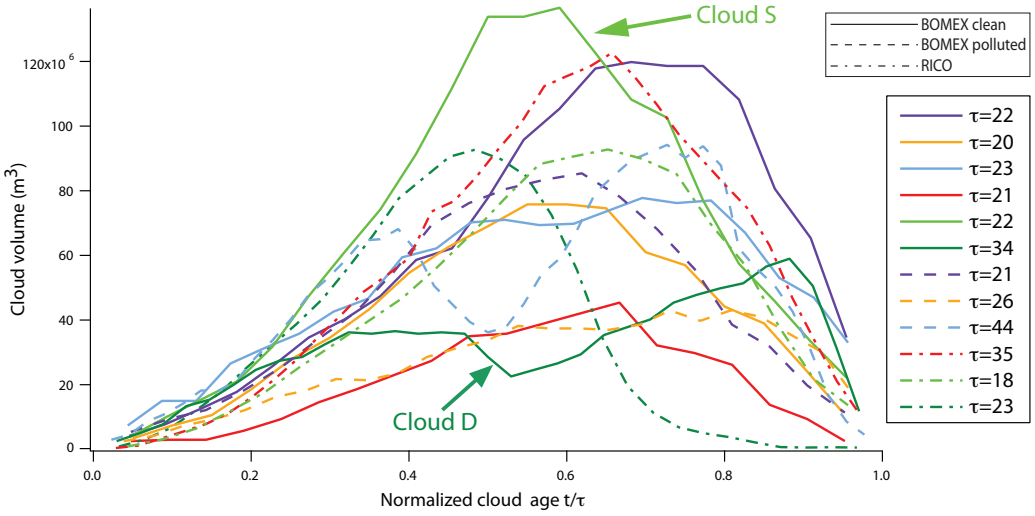



Figure 2.2: Cloud volume vs normalized time. Lifetime $\tau$ is in minutes.

and double-pulse clouds diverged: all single-pulse clouds (e.g. cloud S in Fig. 2.2) continued to grow, reaching a maximum volume in the interval $0.5 < t/\tau < 0.8$ and subsequently dissipated. Double-pulse clouds (e.g. cloud D in Fig. 2.2) experienced some dissipation in the interval $0.4 < t/\tau < 0.6$ followed by a period of renewed growth and eventually dissipation. There are divergent paths by which individual clouds dissipate. For example, clouds can dissipate from the base up, from the top down or from a combination of the two (model results not shown). At any altitude, dissipation along the cloud perimeter exhibits similar variability. This occurs because dissipation is not subject to the same constraints as nascence, whereby all clouds must grow upward from the lifting condensation level. Because there is no consistency in the evolution of clouds near the end of their lifetime, it is unlikely that there exists an accurate clock for this time period. For this reason we omit from our analyses $t/\tau > 0.9$, which corresponds to the final 3 to 5 minutes of cloud lifetime. When a cloud initially forms, the air is warmer and has more water vapor than the surrounding clear air, giving it a strongly positive value of $\Delta\theta_v$ as seen in Fig. 2.3. As the cloud grows older, $\Delta\theta_v$ decreases and eventually becomes negative such that rising motion gives way to subsiding motion. As expected, the time series of $\Delta\theta_v$ in Fig. 2.3 show

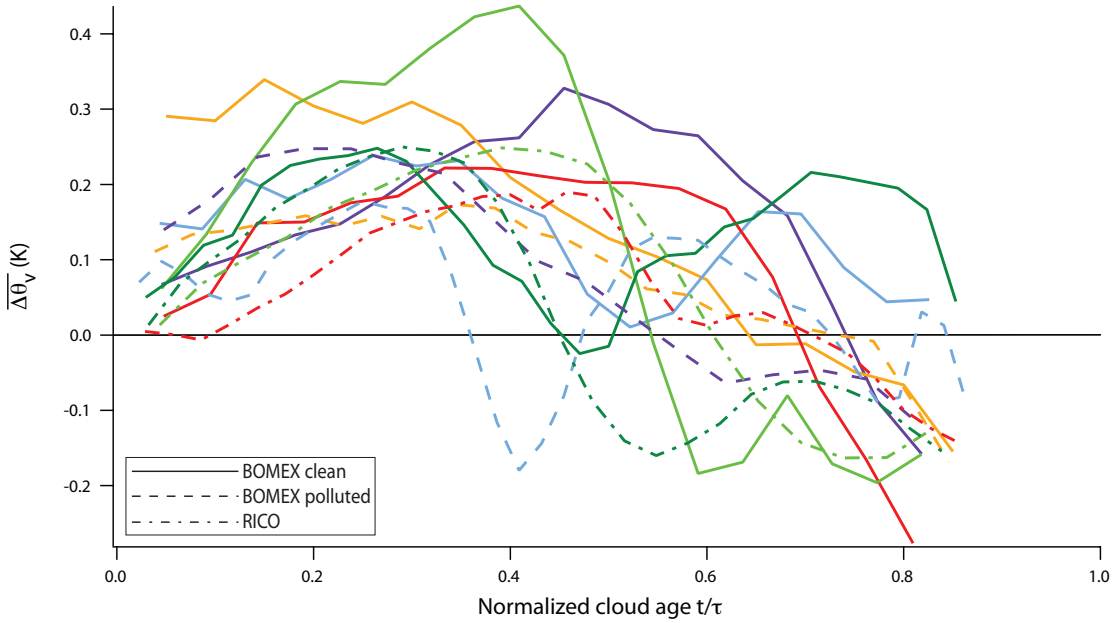



Figure 2.3: Volume-averaged time series of $\Delta\theta_v$.

growth (i.e. $\frac{dV}{dt} > 0$) when the cloud is positively buoyant (i.e. $\Delta\theta_v > 0$ K) and dissipation when the cloud is negatively buoyant. Figure 2.4 illustrates the relationship. Analyzing only points with $|\Delta\theta_v| \geq 0.05$ K, 93% of the analyzed points in Fig. 2.4 lie within the upper-right and lower-left quadrants, indicating a robust correlation between growth and buoyancy. Comparing the volume and $\Delta\theta_v$ time series of cloud D (Figs. 2.2 and 2.3) illustrates that this correlation holds for multiple-pulse clouds.

### 2.3.2 The ideal clock

The ideal cloud clock must account for variation in both cloud extrinsic properties (i.e. lifetime and size) and environmental conditions. The former is minimized by normalizing time and utilizing intrinsic rather than extrinsic cloud properties. Some techniques to account for variability in environmental conditions are explored in section 2.3.4. Schematically, the ideal clock is a monotonic function of time whereby a single measurement of a cloud (by aircraft) can be used to infer a narrow range of *normalized*

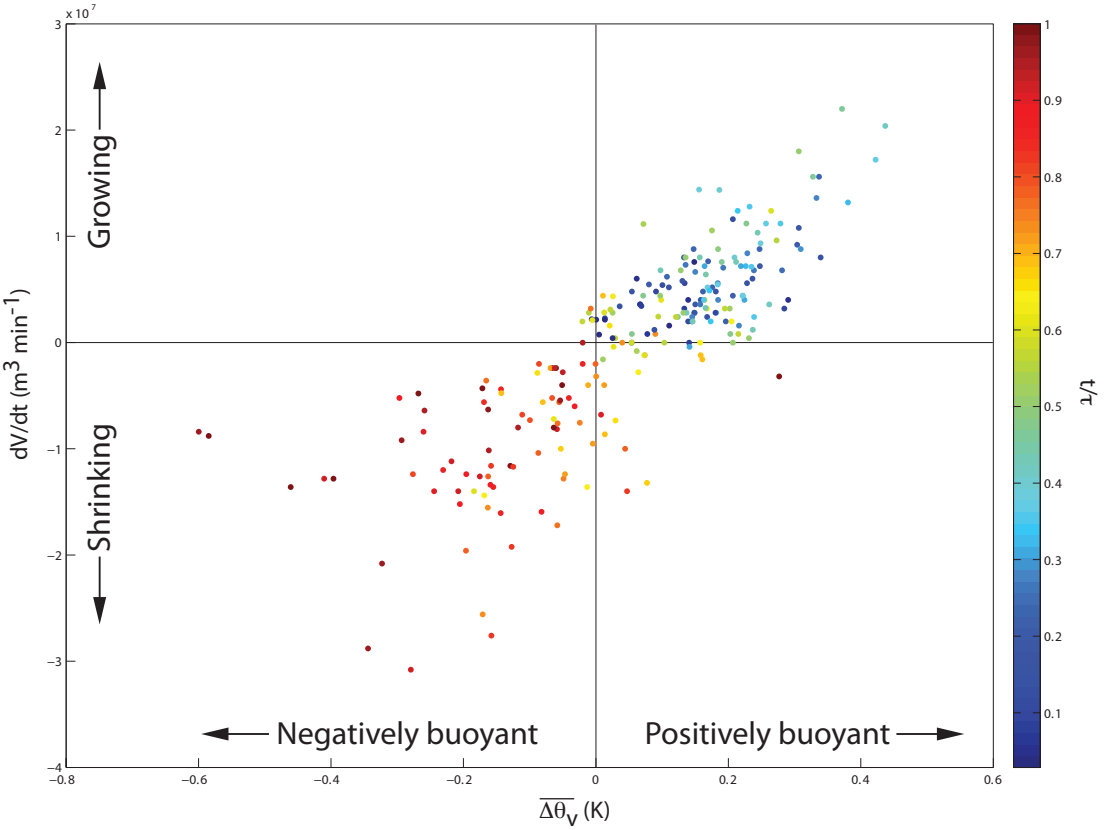



Figure 2.4: Scatter plot of volume-averaged $\Delta\theta_v$ and $\frac{dV}{dt}$.

age.

### 2.3.3 Failures

Table 2.2 lists all the potential clock variables and averaging quantities analyzed. All possible combinations were examined. Potential clock variables fail for a variety of reasons. For example, potential temperature shows a slight increasing trend over time (Fig. 2.5), but the dynamic range is small, with $\theta$ varying by about 1% of the initial value over cloud lifetime. The poor dynamic range implies that a combination of sampling variability and measurement uncertainty translates to a highly uncertain age estimate. The buoyancy perturbation $\Delta\theta_v$ does not work as a clock because the

| Intrinsic | | Extrinsic (relative to cloud) |
|---|---|---|
| Total water mixing ratio | $r_t$ | Depth |
| Liquid water mixing ratio/content | $LWC$ | Area |
| Potential temperature | $\theta$ | Maximum cross-sectional area |
| Virtual potential temperature | $\theta_v$ | Surface area |
| Moist static energy | $MSE$ | Volume |
| Vertical velocity variance | $\overline{w'^2}$ | Liquid water path |
| | | Liquid water center of mass |

Table 2.2: Intrinsic and extrinsic variables examined

individual cloud magnitude is dependent on cloud volume and time series are multi-valued, even for single-pulse clouds (Fig. 2.3). The altitude corresponding to the cloud liquid water center of mass (Fig. 2.6) functions reasonably as a clock because it monotonically increases over time. In practice, though, measuring center of mass *in situ* is not plausible; it could be achieved by rapidly scanning cloud radar and an assumed *Z-LWC* relationship. The latter problem has been explored elsewhere [*Koren et al.*, 2009, e.g.]. As shown in Fig. 2.7, cloud top height operates in a qualitatively similar manner to center of mass, is multivalued for all analyzed clouds, and for older clouds ($t/\tau > 0.3$) estimates cloud age with poor accuracy.

### 2.3.4 Total water as cumulus clock

Assuming adiabatic lifting, the value of the total water mixing ratio $r_t$ at cloud base during cloud nascence is approximately equal to the mixed layer value $r_{t,ml}$. Normalizing time series of $r_t$ by the domain-average mixed layer value $\overline{r_{t,ml}}$ yields the normalized total water $r_t^* \equiv r_t/\overline{r_{t,ml}}$ which allows for comparison between different atmospheric conditions. Initial values of $r_t^*$ are approximately unity because clouds form from pulses of buoyant mixed-layer air. It is possible that initial values of cloud-average $r_t^*$ may be greater than unity because of spatial variability in the $r_t$ field. For all clouds, the

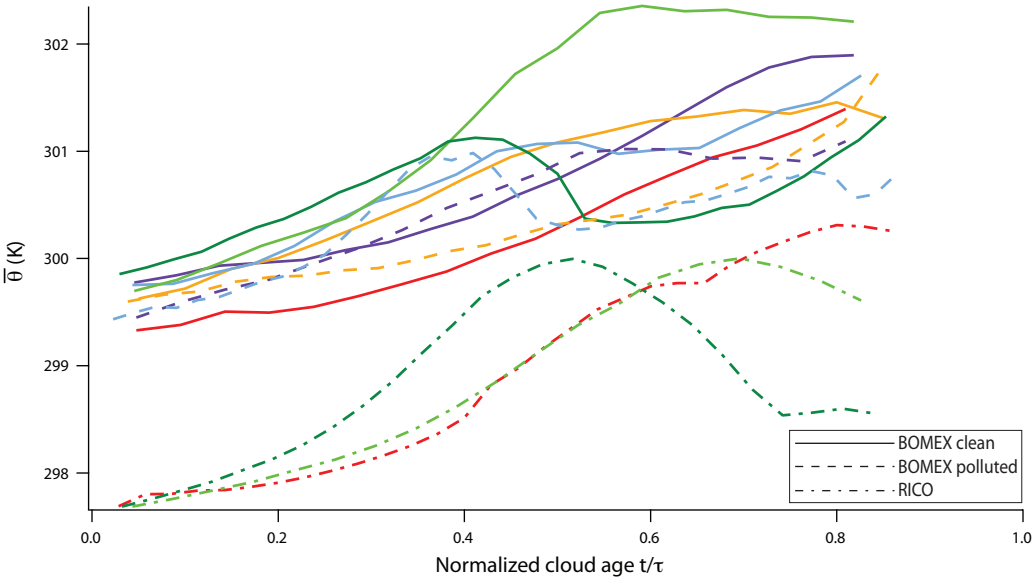



Figure 2.5: Time series of volume-averaged potential temperature.

volume-averaged time series of $r_t^*$ initially ($t/\tau < 0.4$) decreases monotonically (Figure 2.9, upper left). We attribute this decrease to entrainment rather than precipitation. For shallow trade-wind convection [*Stevens*, 2005], environmental $r_t$ generally decreases with altitude above the surface mixed layer. Hence mixtures of entrained and mixed-layer air will have lower $r_t$ than the pure mixed-layer air that initially comprises the cloud. If the decrease were instead due to precipitation, $r_t^*$ would be approximately constant during the growth phase and only begin to decrease during the mature phase when the cloud is sufficiently deep for precipitation to develop. However, $r_t^*$ begins to decrease immediately indicating that entrainment likely dominates the $r_t^*$ trend. We further address the impact of preciptiation in section 2.3.5.

#### 2.3.4.1 Single-pulse clouds

For single-pulse clouds, $r_t^*$ monotonically decreases throughout cloud lifetime as shown in Fig. 2.8 . The clouds dissipate once total water is less than saturation. In be-

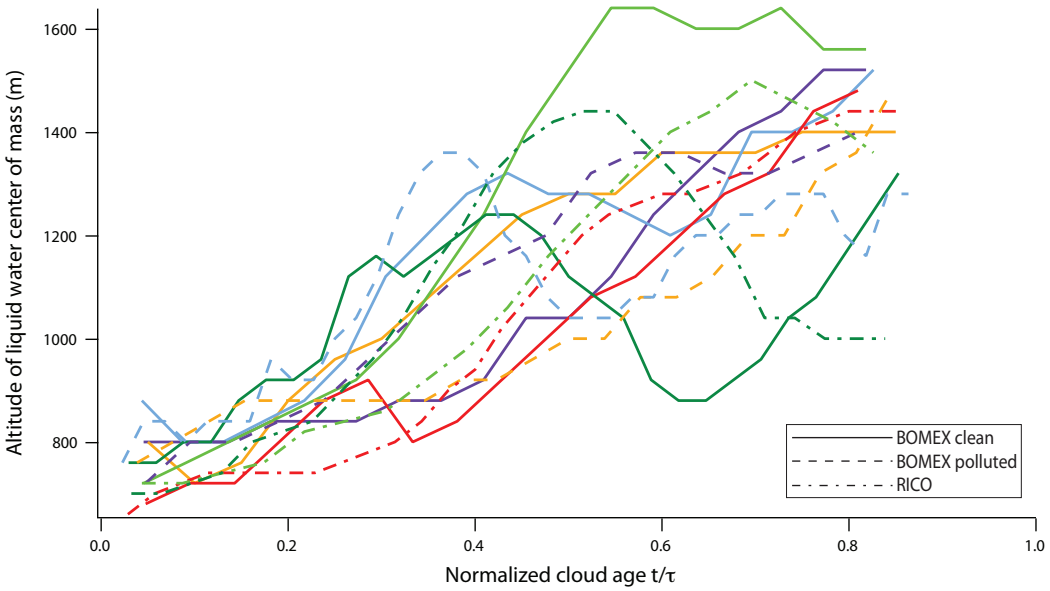



Figure 2.6: Time series of the altitude of liquid water cloud center of mass.

tween, the slope of $r_t^*$ is fairly linear [1] ($R^2 = 0.88$) among single-pulse clouds: the mean slope and standard deviation are $-0.23 \pm 0.06$ with $R^2$ for individual clouds ranging from 0.88 to 0.97. This indicates that entrainment causes drying at an approximately fixed rate with respect to normalized time, independent of maximum volume and lifetime. In some respects, this is not surprising. All clouds begin around $r_t^* \sim 1$, while the final $r_t^*$ value should be the saturation water vapor mixing ratio. Over the lifetime of each cloud, the decrease in $r_t^*$ is constrained between these two values. Thus the slope with respect to normalized time is not able to vary widely. Some variance of the slope is expected due to variation in final $r_t^*$ values. This occurs because clouds dissipate at different altitudes, corresponding to different temperatures and hence different saturation mixing ratios.Because $r_t^*$ monotonically decreases in an approximately linear fashion, we propose that it can be used as a cumulus clock. As illustrated in Fig. 2.8, a cloud

[1] The data are better fit by a parabola ($R^2 = 0.93$), but we chose to use the simplest possible fit because of the small sample size. One possible explanation for a parabolic curve is that when a cloud is young and shallow, the difference between enviromental and cloud $r_t$ is small while as the cloud ages and deepens, the $r_t$ contrast grows.

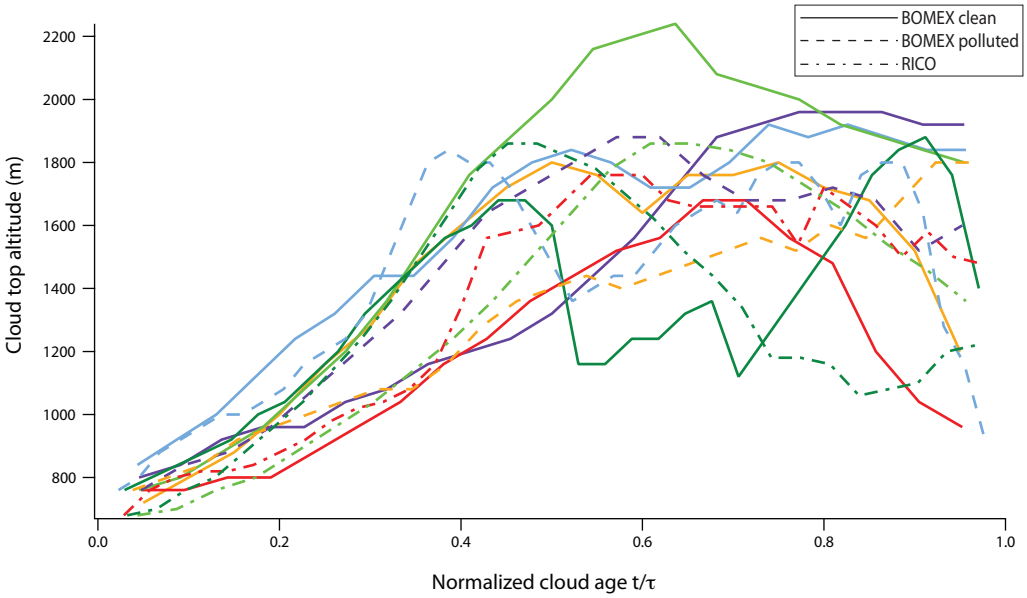



Figure 2.7: Time series of cloud top altitude.

with mean $r_t^* = 0.9$ is predicted to have an approximate age of $t/\tau = 0.48 \pm 0.10$. This age uncertainty of $\Delta(t/\tau) \sim 0.1$ represents approximately one standard deviation and is consistent over cloud lifetime. This uncertainty is sufficiently low for reasonable estimation of the life phase of single-pulse clouds. The age model applies equally to the RICO and BOMEX meteorological soundings, the clean and polluted BOMEX clouds, and to clouds of differing lifetime and volume, suggesting that it may be generalizable to shallow cumulus in a variety of environments. Further study is necessary to better understand the range of environmental conditions to which the clock may be applied. Up to this point, the $r_t^*$-based clock has used cloud average $r_t^*$ values. However, for aircraft observations, it is desirable to infer cloud age from a single aircraft pass. The monotonic decrease in $r_t^*$ with time evident in the cloud-averaged time series (Fig. 2.8) is also seen in the time series of $r_t^*$ at selected normalized cloud layer levels $z^* = 0.25$; 0.50; and 0.75 where $z^* = 0$ corresponds with instantaneous cloud base and $z^* = 1$ is instantaneous cloud top (Fig. 2.9). The variability of $r_t^*$ among single-pulse clouds is also similar between cloud-averaged and single-level time series. The primary

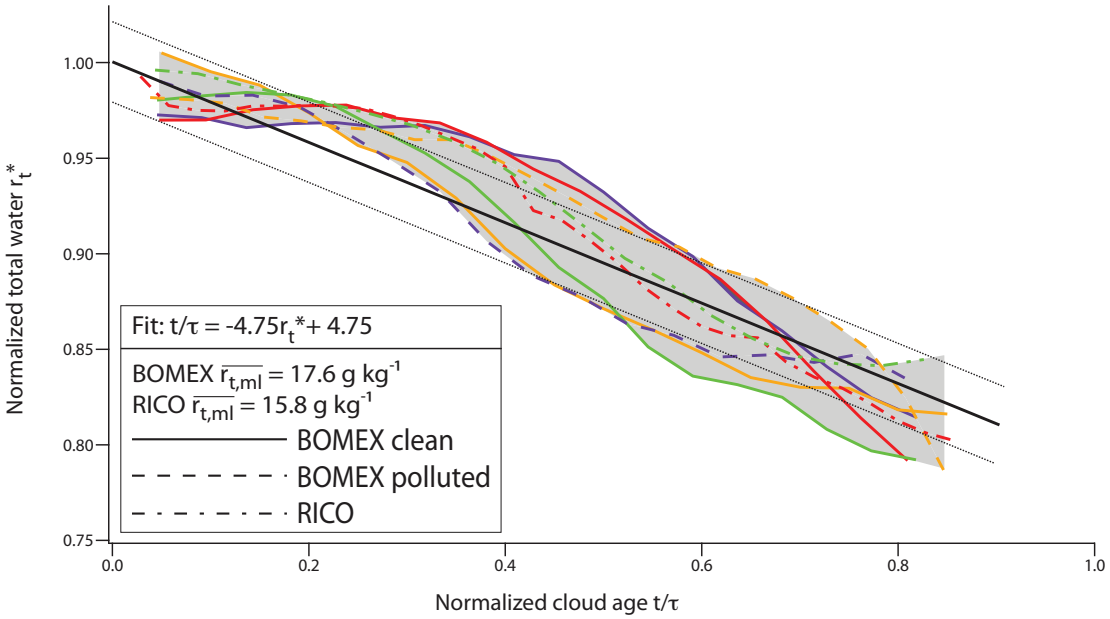



Figure 2.8: The time evolution of $r_t^*$ is well fit by linear regression. The solid black line is the fit and the dashed black lines are approximately one standard deviation from the mean slope.

difference among the different levels is that the final value of $r_t^*$ decreases with altitude because environmental $r_t$ decreases with altitude. In addition, the colder temperatures near cloud top can sustain saturation at lower $r_t^*$ values than near cloud base. As a result, there is greater dynamic range in the time series of $r_t^*$ at cloud top than at cloud base. The time series at $z^* = 0.50$ closely follow the cloud-average time series upon which the clock is based, suggesting that it is most accurate to infer cloud age from single-level cloud passes at mid-cloud.

#### 2.3.4.2 Multiple-pulse clouds

In those periods where a cloud exhibits increases in $r_t^*$ with time, the cloud is experiencing a second buoyancy pulse, bringing with it moisture-rich mixed layer air. Cloud average $r_t^*$ cannot return to its initial value near unity because it is a cloud-integrated value with "memory" of past entrainment drying. After the influx of moisture,

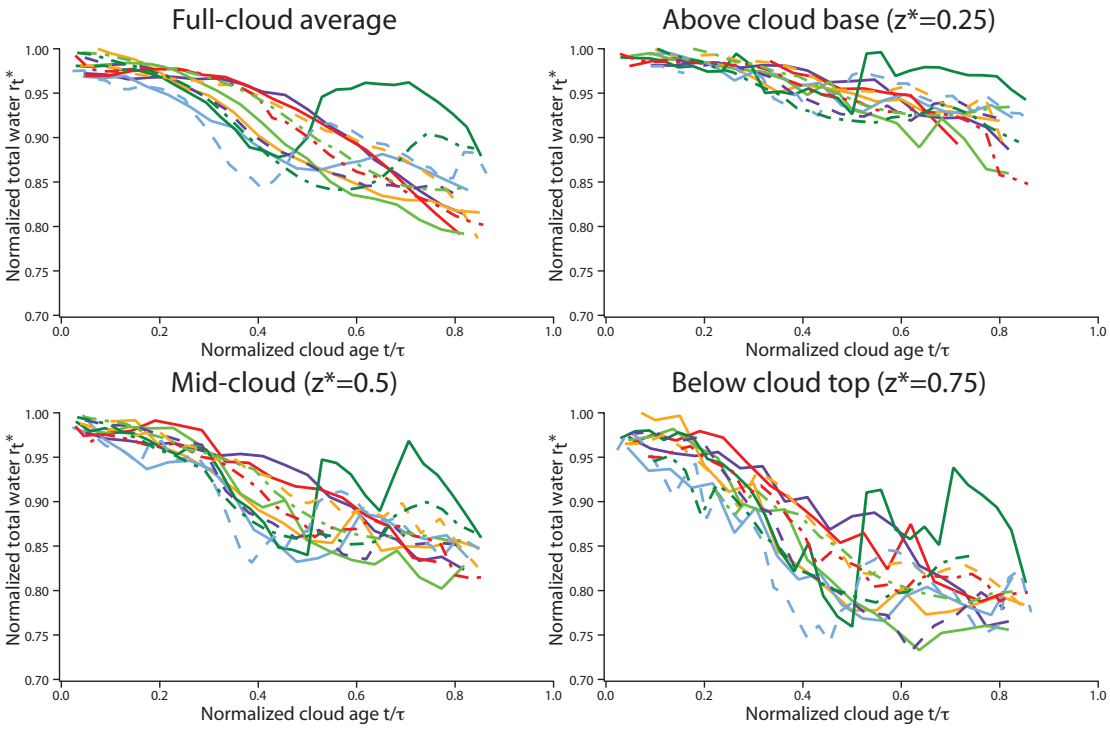



Figure 2.9: Individual altitude time series of $r_t^*$ show the same general trend as the full-cloud average, but higher altitudes exhibit a larger dynamic range.

$r_t^*$ again decreases via entrainment until cloud dissipation. Multiple pulses appear to extend cloud lifetime. The median lifetime of the single-pulse clouds analyzed is 22 min, with a range of 18 to 35 min. The two most obvious multiple-pulse clouds last for 34 and 44 minutes. While multiple-pulse clouds have a longer lifetime than single pulse clouds, they are still constrained to an intial value of $r_t^*(0) \sim 1$ and a dissipation value approaching the saturation vapor mixing ratio. Interpretation of inferred age is more complicated for multiple-pulse clouds. Figure 2.10 illustrates $r_t^*$ and $\Delta\theta_v$ for one multiple-pulse cloud with a "measurement" of $r_t^* \approx 0.90$. The single-pulse age model predicts an age $t/\tau \approx 0.5 \pm 0.1$, while the cloud exhibits $r_t^* \approx 0.90$ at 3 times ($a_1 \sim 0.3$, $a_2 \sim 0.5$, $a_3 \sim 0.6$, where $a_i$ are the times at which hypothetical measurements were taken over cloud lifetime). *Heus et al.* [2009] (hereafter H09) interpret and analyze multiple pulses within a single cloud as independent events.

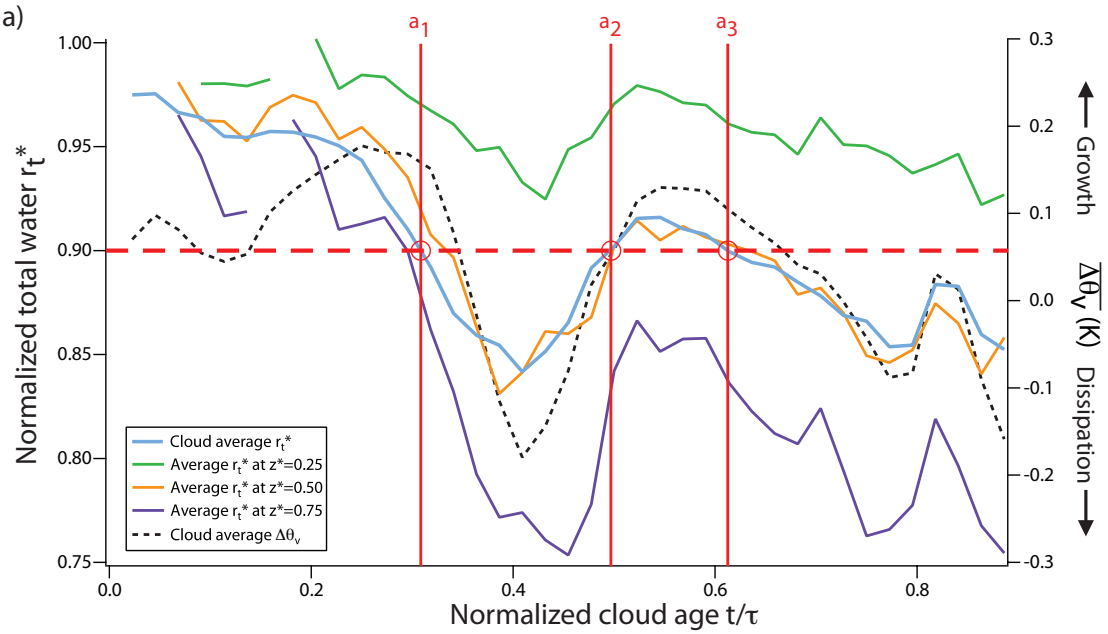



Figure 2.10: Time series of $r_t^*$ averaged over the entire cloud and at individual levels. Cloud average $\Delta\theta_v$ is shown for comparison.

Following the interpretation of H09, the inferred ages at times $a_1$ and $a_3$ can be viewed as *equivalent ages* for independent single pulses. This interpretation is supported by comparison of the cloud average $r_t^*$ and $\Delta\theta_v$ in Figure 2.10 which shows similar behavior at times $a_1$ and $a_3$. In both cases, $\Delta\theta_v$ is similar in value and decreasing from a local maximum, suggesting *dynamical similarity*. Thus it is appropriate that the inferred clock age should be the same at times $a_1$ and $a_3$. Assuming the two pulses are independent, we can determine an independent single pulse age associated with each pulse. The times $a_1$ and $a_3$ can be expressed as single pulse ages $b_1$ and $b_2$, respectively. In Fig. 2.11, we approximate the respective single pulse time axes and roughly estimate the independent pulse ages $b_1 \approx 0.6 \pm 0.1$ and $b_2 \approx 0.4 \pm 0.1$. The estimates for $b_1$ and $b_2$ agree reasonably well with the inferred single-pulse age $t/\tau \approx 0.5 \pm 0.1$. In the time period surrounding time $a_2$ ($0.4 \lesssim t/\tau \lesssim 0.5$, Fig. 2.10), $r_t^*$ increases with time. The increase occurs gradually not only in the average, but also at individual levels of the cloud (Fig. 2.10), albeit for different durations (between 3-6 min). Although $r_t^*$

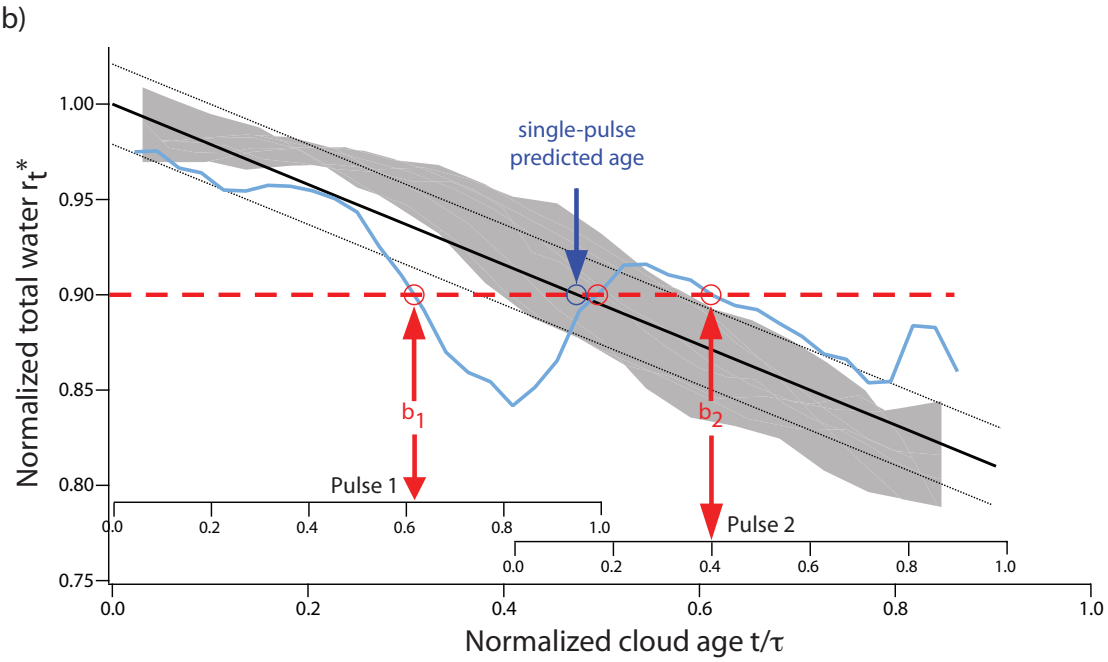



Figure 2.11: A cloud average $r_t^*$ time series for a double-pulse cloud. The solid black line is the single-pulse fit, the dashed black lines are the fit $t/\tau \pm 0.1$, and the gray area envelops the single-pulse cloud data. The Pulse 1 and Pulse 2 time axes show the independent pulse ages associated with times $b_1$ and $b_2$, respectively.

begins to increase at different times for different levels, the second peak in $r_t^*$ is reached at approximately the same time ($t/\tau \sim 0.5$) at each individual level shown in Fig. 2.10. Detailed examination of cloud evolution shows that there are multiple reasons for the $r_t^*$ increase. The second pulse begins near cloud base and propagates upward, bringing high $r_t^*$ air to the cloud. At the same time, dissipation is occurring at cloud top, which removes the lowest $r_t^*$ values from the cloud because these values are found at the coldest temperatures/highest altitudes. No single age appropriately captures the dynamical complexity during the increase in $r_t^*$ because, unlike the initial pulse that created the cloud, growth and dissipation occur concurrently at different regions in the cloud. The time period surrounding $a_2$ is neither a clear growth nor dissipation phase. The $r_t^*$ clock can be used to sort clouds by life phase, in conjunction with the knowledge that a cloud is growing when $\Delta\theta_v > 0$ K and dissipating when $\Delta\theta_v < 0$ K (Fig. 2.4).

We propose that clouds can be designated as being in the growth phase when $r_t^* > 0.95$ and $\Delta\theta_v > 0$ K, and in the dissipation phase when $r_t^* < 0.85$ and $\Delta\theta_v < 0$ K. The variable space in between these boundaries is by default classified as the mature phase. Applying these criteria to all the clouds, 113 of 350 total sampled cloud time steps are classified as "growth" phase and 73 of 350 are classifed as "dissipation" phase. The remaining 177 time steps are classified as mature. Of the 113 growth phase time steps, 103 are associated with cloud age $t/\tau < 0.4$ and the remaining 10 time steps with the second pulse of a multiple-pulse cloud. Of the dissipation phase time steps, 60 of the 73 are associated with cloud age $t/\tau > 0.7$ and the remaining 13 with dissipation preceding the second pulse of two multiple-pulse clouds. The advantage of classifying clouds by life phase is that it resolves the issue of attributing a unique normalized age to multiple-pulse clouds, enabling diagnosis of multiple growth and dissipation phases in a single lifetime. Most subsequent pulses will be classified as mature phase, though, because of the dynamical complexity inherent to multiple-pulse clouds discussed above. In summary, the normalized age model inferred from time series of cloud average $r_t^*$ predicts normalized age within $\Delta t/\tau \sim 0.1$ for single-pulse clouds and sorts all clouds into the growth and dissipation phases. The $r_t^*$ clock is applicable to multiple-pulse clouds if the evolution of such clouds is viewed as a series of independent single pulses, i.e. if cloud lifetime is subdivided into pulse lifetimes as in Figure 2.11. From this perspective, each successive measurement of the same $r_t^*$ value corresponds with a unique independent pulse age, regardless of the cloud's history. The transition period (or periods) between pulses during which $r_t^*$ increases is dynamically complex and does not fit in the simple three phase view of the cumulus life cycle, as clouds can display characteristics of all three phases during those timespans.

### 2.3.5 Caveats and limitations

We attribute the loss of total water over cloud lifetime mainly to entrainment. However, this loss can also be expressed as an equivalent lifetime-average rain rate on the order of 1 cm hr$^{-1}$. Rain rate was derived using the relationship $R \sim LWP^{\alpha} N_D^{\beta}$ with $\alpha =$

2.5 and $\beta = -1$ [*Jiang et al.*, 2010]. Of the 12 clouds analyzed, 9 exhibit lifetime-average $R \ll 1$ mm hr$^{-1}$ and thus precipitation is negligible compared to entrainment. The most heavily precipitating cloud exhibits lifetime-average $R \sim 2$ mm hr$^{-1}$, which is a factor of five smaller than the entrainment equivalent water loss. From these results, we infer that entrainment and not precipitation is the primary mechanism for liquid water depletion for the clouds sampled. Whether or not the $r_t^*$ clock is applicable to deeper, more heavily precipitating clouds remains an open question. We speculate that heavy precipitation would not substantially affect the utility of the $r_t^*$ clock. As discussed above, the slope of the clock depends on the initial and final values of $r_t^*$. The initial value is constrained to be near unity, while the final value depends on the saturation vapor mixing ratio, which is a function of temperature. Cloud dissipation dominated by entrainment can lead to cooler temperatures relative to dissipation dominated by precipitation. Entrainment mixes colder environmental air into the cloud and causes cloud drop evaporation. Precipitation reduces the potential for evaporative cooling by cloud droplet evaporation, leading to warmer cloud dissipation temperatures. We estimate that heavy precipitation would increase the final value of $r_t^*$ by a few hundredths at most, less than the variabilty observed among the analyzed clouds (Fig. 2.8). Hence heavy precipitation would not dramatically alter the slope of $r_t^*$ with respect to normalized time (but presumably would reduce cloud lifetime $\tau$) and thus the $r_t^*$ clock may also be applicable in such situations. There are some caveats associated with the results of this study. First, the effective dynamical age inferred from the $r_t^*$ clock does not accurately represent time-integrative processes like collision-coalescence which are not reversible by subsequent buoyancy pulses. While such pulses act to "turn back" the $r_t^*$ clock, the cloud drop size distribution does not experience a similar reversal, i.e. the large drops formed by collision-coalescence are unlikely to shrink or disappear. The twelve clouds examined are not a large set from which to draw generalized conclusions about all small cumulus. Since the clouds were selected by a human observer, it is possible that the selection process was biased. In particular, the clouds chosen for the study were more spatially isolated than the average cloud in the domain. While the selection was biased toward

more isolated clouds, a BOMEX simulation by *Dawe and Austin* [2011] found that the majority of clouds form and decay in isolation (75% and 89% of all simulated clouds, respectively). To gain a more statistically robust sampling, the cloud tracking algorithm of *Dawe and Austin* [2011] could be employed. Furthermore, the differences between modeled and real small cumulus may impact these results. For example, there is disagreement in the representation of entrainment and detrainment mixing among different LES models [*de Rooy et al.*, 2013]. Because the $r_t^*$ clock relies on moisture reduction, differences in how entrainment mixing and subsequent drying are represented may alter the operation of the clock.

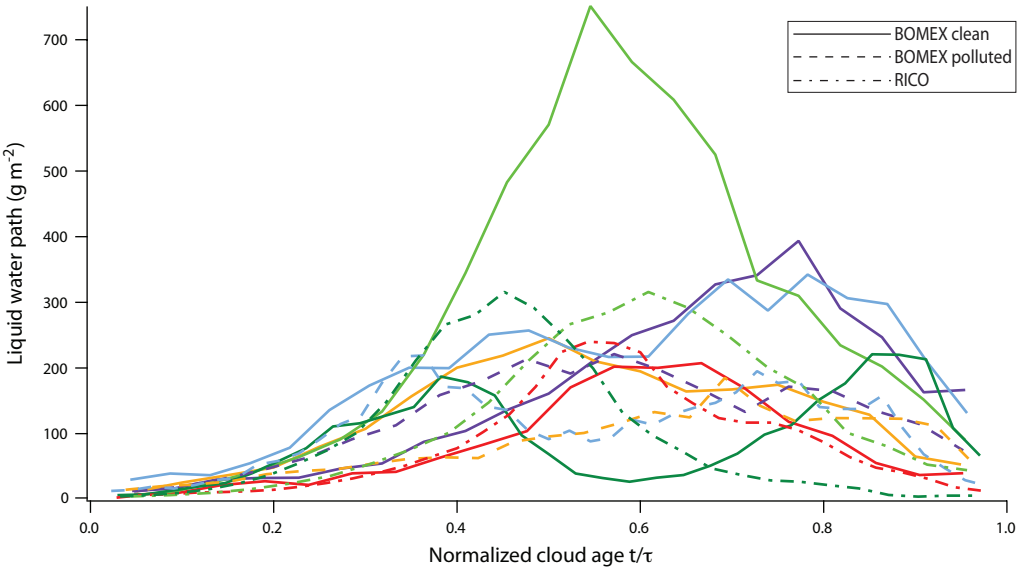



Figure 2.12: Time series of liquid water path. Liquid water path is the cloud-integrated LWC divided by maximum cross-sectional area.

## 2.4 Conclusions

The goal of this study is to find an observationally-relevant, single-measurement cumulus clock. The purpose of the clock is to classify clouds by life phase, hence giving temporal context to observations of such clouds. We find that for LES-modeled

shallow trade wind cumulus clouds, the normalized total water mixing ratio $r_t^*$ (defined as the measured total water mixing ratio $r_t$ normalized by the average mixed layer value $\overline{r_{t,ml}}$) can be used as a clock. It works because the cloud is initially moisture-rich ($r_t^* \sim 1$), but over time, entrainment of surrounding, drier environmental air causes $r_t^*$ to decrease with time. The simulated clouds exhibit low lifetime-average rain rates ($R < 3$ mm d$^{-1}$). The operation of the clock is insensitive to aerosol loading, environmental sounding and extrinsic cloud properties such as lifetime and volume. In the simplest case of a single-pulse cloud, interpretation of the clock provides a basis for classification of clouds by life phase. Clouds can be designated as being in the growth phase when $r_t^* \gtrsim 0.95$ and $\Delta\theta_v > 0$ K, and in the dissipation phase when $r_t^* \lesssim 0.85$ and $\Delta\theta_v < 0$ K. In between, clouds are by default classified as mature. Interpretation of the age model is more complicated for multiple-pulse clouds. The effect of subsequent pulses generally acts to increase the buoyancy contrast $\Delta\theta_v$, altering the growth rate of the cloud and causing $r_t^*$ to increase with time for some duration before entrainment again dominates the evolution. During periods when $r_t^*$ is decreasing, we interpret the clock as an approximate "pulse-age" rather than "cloud-age" following *Heus et al.* [2009] who describe pulses as independent entities. The degree to which pulses can be considered independent, such that the influence on the cloud of older pulse(s) is minimal relative to the most recent pulse, is still an open question. During periods when $r_t^*$ is increasing, the bottom and top portions of the cloud are dynamically distinct so no single "cloud-age" or life-phase description is sensible. Such cases confound the simple growth/mature/dissipation classification system. We find the clock to be robust for the modeled clouds sampled, but we emphasize that the small, potentially biased population analyzed here does not provide sufficient evidence that the $r_t^*$ clock can be applied universally to all small cumulus. Most importantly, the functionality of the clock in heavily precipitating conditions is unclear. Secondly, the $r_t^*$ clock is not able to accurately record time-integrative processes such as collision-coalescence. Finally, splitting and merging clouds were intentionally not characterized. The applicability of the $r_t^*$ clock may be limited in conditions conducive to significant splitting and

merging among the cloud population. The utility of the clock and the seriousness of the caveats identified here could be tested by repeated aircraft sampling of a single cloud over its lifetime. While the $r_t^*$ small cumulus clock is not perfect, especially in the case of multiple-pulse clouds, it does appear to accurately classify the clouds sampled for this study in the growth and dissipation phases. In between, clouds classified as "mature" exhibit a wider range of behavior and thus dynamical (and other) similarity is not guaranteed. Even this basic classification, confounding Karl Popper's juxtaposition of clouds and clocks, could provide important and useful context for *in situ* cloud observations.

# Chapter 3

# Estimating collision-coalescence rates from observations of marine stratocumulus

## 3.1 Introduction

Low clouds such as trade cumulus and stratocumulus are often observed to precipitate despite their muted dynamics in comparison with deep convection [*Lau and Wu*, 2003; *Wood*, 2012]. In the absence of ice, collision-coalescence is the primary mechanism by which cloud droplets grow from the small sizes attainable by condensation alone (typically diameter $d < 30\,\mu\text{m}$) to become drizzle particles (diameter of order a few hundred μm), but the rate of growth of droplets of size $d \sim 20 - 60\,\mu m$ is at a minimum with respect to both condensation and collision-coalescence, begging the question of how the first large drops are formed. This bottleneck in growth rate, often referred to as the "warm rain problem" in the reference frame of shallow cumulus, has garnered much attention in the cloud physics community over the years [e.g. *Beard and Ochs*, 1993]. Several solutions to explain the discrepancies between observations and numerical modeling results have been proposed, among which are the existence of ultragiant

cloud condensation nuclei [*Johnson*, 1982; *Knight et al.*, 2002; *Reiche and Lasher-Trapp*, 2010], broadening of the drop size spectrum due to turbulent mixing [*Baker and Latham*, 1979; *Cooper et al.*, 2013], and a direct role of turbulence in increasing collision rates [*Wang and Grabowski*, 2009]. It is immensely challenging to directly observe collision-coalescence *in situ* because of limited instrument sampling volume and statistics in addition to the near impossibility of tracking individual sedimenting drops in real time. Most observational studies attempting to quantify the collision-coalescence process took place in the laboratory during the mid-20th century [*Hocking and Jonas*, 1970; *Shafrir and Gal-Chen*, 1971; *Davis*, 1972; *Jonas*, 1972; *Klett and Davis*, 1975; *Lin and Lee*, 1975] and involved overly-idealized experimental configurations (e.g. bidisperse drops in quiescent conditions) that were unable to reproduce the complexity or turbulent nature of the atmosphere. Even modern-day direct numerical simulations of hydrometeors in incompressible turbulence, considered the gold standard for studies on the role of turbulence in drop size evolution, are unable to reproduce the range of Reynolds numbers relevant to weakly-turbulent stratocumulus [*Ayala et al.*, 2007].

Climate models are sensitive to the representation of clouds and precipitation because of their effects on the energy and moisture budgets of the atmosphere [*Medeiros et al.*, 2008]. Clouds affect the planet's radiative budget by reflecting sunlight and modulating outgoing longwave radiation, and small changes in global cloud cover or albedo of just a few percent could have a radiative forcing on par with that of anthropogenic greenhouse gas emissions [*Slingo*, 1990]. Precipitation affects numerous aspects of human life as well as modulating cloud dynamics and lifetime; accurately predicting where and how much precipitation will fall to the surface remains a grand challenge in meteorology. Observational constraints on collision-coalescence rates are therefore needed to validate parameterizations of microphysical process rates to improve model prediction of cloud and precipitation amount as well as spatiotemporal distribution.

Models represent cloud processes using several different approaches. The two most commonly used schemes either assume that the size distribution of cloud particles follows some fixed distribution (bulk schemes) while the other allows the particle size

distribution to evolve freely, but at much greater computational expense (bin schemes). Bulk microphysical schemes employed in large-scale models use a threshold size (typically $d \sim 40 - 50\,\mu\text{m}$) to divide liquid water drops into "cloud droplet" and "rain drop" categories such that the collision-coalescence process is subdivided into three regimes: autoconversion (production of rain drops by collisions of cloud drops), accretion (growth of rain drops by scavenging of cloud drops) and hydrometeor self-collection (growth of rain drops by collisions with other rain drops). *Austin et al.* [1995] analyzed aircraft observations of the drop size distribution (DSD) taken off the coast of California to estimate the autoconversion rates necessary to reproduce observed precipitation rates using an equilibrium model that also took into account the effects of condensation, accretion, sedimentation, and turbulent mixing. For a precipitation-producing DSD, the authors found that autoconversion rates 2 orders of magnitude greater than predicted were required to match the observed precipitation flux [*Austin et al.*, 1995]. There are several factors that may contribute to such large enhancements. For example, the cloud microphysical measurements were performed using a Forward Scattering Spectrometer Probe (FSSP), which is known to overcount large drops and undercount small drops due to coincidence of small drops in the instrument view volume [*Chuang et al.*, 2008], which may have resulted in overestimation of autoconversion rates given the observed DSDs. In addition, only three "representative" 60-second average spectra were analyzed by *Austin et al.* [1995], and the shape and concentration of the DSD in the autoconversion regime were held constant throughout the depth of the modeled cloud. The assumption of constant shape and concentration precludes the effects of vertical development; *in situ* observations of stratocumulus show an increase in DSD mode diameter with increasing height, while a widening of the right tail of the DSD is observed when descending from cloud top [*Rossiter*, 2012].

A qualitatively similar result to that of *Austin et al.* [1995] was found by *Pincus and Klein* [2000] in their analysis of the "tuning parameters" used to modulate autoconversion rates in large-scale models, where rate enhancements up to a factor of 15 are needed to reach agreement with observations. *Pincus and Klein* [2000] attribute the cause of

autoconversion rate underprediction to subgrid scale variability in the quantities used to calculate process rates, such as vertical velocity or liquid water mixing ratio, and the nonlinear relationship between those quantities and process rates. This insight led to the development of statistical "upscaling" schemes that integrate over an assumed probability density function of subgrid-scale variability to more accurately predict process rates [e.g. *Larson and Griffin*, 2013]. Despite such advances in representing the effects of small-scale variability, the definition of a "local" length scale with respect to the drop size distribution remains ill-defined; a recent review of microphysical process parameterizations suggested 100 m as sufficient [*Khain et al.*, 2015], but this figure was derived from modeling studies and has not been observationally derived.

In this study we seek to retrieve collision rates in the bottleneck size regime ($d \sim 20 - 60\,\mu$m) from *in situ* aircraft observations of stratocumulus and explore the role of small-scale variability in the DSD in controlling retrieved rates. In particular, we focus on the first few collisions that drops undergo by using observations of the cloud top region, where the fewest large drops are found and of the stratocumulus top region where drizzle is initiated [*Vali et al.*, 1998; *Stevens et al.*, 2003]. The analysis is applied to observations averaged over two length scales: the length of an entire observational leg ($\sim$ 30 km) and a single penetration through cloud top ($\sim$ 1.5 km), which could alternately be viewed as integrating over several boundary layer-spanning eddies versus sampling a single coherent large eddy.

## 3.2 Method

### 3.2.1 Observations

We use observations from the Physics of Stratocumulus Tops (POST) flight campaign which took place during July and August 2008 off the central California coast. Flights were conducted by the Center for Interdisciplinary Remotely-Piloted Aircraft Studies (CIRPAS) Twin Otter aircraft with dynamic, thermodynamic, and microphysics instrumentation (details available in *Carman et al.* [2012] and *Gerber et al.* [2013]).

The flight plans were designed approximately to follow a Lagrangian air mass in the horizontal direction while sampling the interface between the stratocumulus layer and the free troposphere in the vertical direction [*Malinowski et al.*, 2013]. To this end, the Twin Otter primarily sampled the cloud top region in a sawtooth pattern, repeatedly ascending and descending from $\sim$ 100 m below cloud top to $\sim$ 100 m above at a vertical rate of change of $\sim 1.5\,\mathrm{m\,s^{-1}}$. Each leg was composed of 4-5 sawtooth maneuvers that took about 10 minutes total and covered roughly 30 km. We refer to the individual ascents and descents of each leg as "segments," and will use these segments as the smallest coherent sampling unit in our analyses. In between the cloud top legs, surface and below-cloud flux legs were executed as well as at least one vertical sounding at the beginning and/or end of each flight.

There were 17 total research flights flown during POST that sampled a range of meteorological and microphysical conditions, inversion strength, rain rate, aerosol loading, time of day, etc. (cf. Table 3.1 herein and Table 1 in *Gerber et al.*, 2013). All flights are considered in this study except TO9 and Leg 1 of TO11 because the observed cloud layers were too low and thin to yield adequate cloud observations, yielding a total of 50 flight legs for analysis. For this analysis we use 1 Hz cloud drop size distributions (DSDs) inferred from an Artium Flight Phase Doppler Interferometer [*Chuang et al.*, 2008] which measures drops up to diameter $d$ $\sim$100 μm. The Twin Otter was also equipped with a DMT Cloud Imaging Probe (CIP) that samples drops of diameter 25 to 1550 μm, but its resolution is too coarse to be included in the analysis. We convert from number to mass concentration assuming spherical drops and calculate liquid water content (LWC) by integrating over the PDI distributions as well as sedimentation flux (or rain rate $R$). This method of calculating LWC compares well with the Twin Otter-standard Gerber PVM-100A LWC after accounting for differences in drop size range measured [*Carman et al.*, 2012]. LWC is used to identify cloud top, here defined as the highest altitude with LWC $> 0.05\ \mathrm{gm^{-3}}$ during a given leg. Cloud top rain rate $R_{CT}$ is calculated from leg composite merged DSDs (i.e. combined PDI and CIP data) with an instrument crossover diameter at $d_{cross} = 64\,\mu\mathrm{m}$.

For the analysis, the drop size distribution within 40 m of estimated cloud top height is averaged to give a leg composite mean DSD, which we assume is representative of the mean cloud state. Examination of leg mode diameter $d_0$ in Table 3.1 shows minimal variability among legs (typically $d_0$ varies by <2 μm per flight, corresponding to about one PDI bin) but substantial variability between days ($d_0$ ranges from 12.8 to 30.3 μm). Each segment can also be analyzed individually, thus reducing the averaging distance from 30 km to ∼ 1.5 km. Individual segments were subject to slightly different criteria to be included in the analysis: we require segment mean $LWC > 0.05\,\mathrm{gm}^{-3}$ and mean $N_D > 5\,\mathrm{cm}^{-3}$. An alternate leg composite DSD can then be calculated by taking the mean over the individual segment DSDs from a given leg. The effects of using this alternate composite are explored in Section 3.4.3. As might be expected, there is somewhat more variability in $d_0$ when derived from segments than from the standard leg composite, with 6 of 50 legs exhibiting standard deviation in segment $d_0$ greater than 3 μm. This is mostly due to using the mode statistic for the characteristic size.

### 3.2.2 Rebinning of the DSD

Drop size distributions near cloud top typically exhibit a single peak followed by a rapid decrease in concentration on either side of the peak as measured by both the PDI and CIP. An example DSD is shown in Figure 3.1. For POST DSDs, the PDI accurately counts drops up to 50-75 μm in diameter depending on the case, above which sampling volume is insufficient for robust drop counting statistics. Heavily drizzling cases (i.e. cases with more large particles) have a broader usable sampling range for both cloud probes, while for non-drizzling cases very few drops greater than about 100 μm are observed. As 50 μm is a widely accepted threshold diameter for efficient drop growth by collision-coalescence [*Pruppacher and Klett*, 1997], the drop size regime sampled by the PDI is ideal for investigating the onset of the collision-coalescence process. In order to more closely examine the first few collisions drops undergo and the rates at which these collisions occur, it is helpful to rebin the DSD in terms of the number of collisions a drop has experienced. This approach was first proposed by *Rossiter* [2012].

| Flight # | Date | $z_{CT}$(m) | $d_0$ (μm) | $N_D$ (cm$^{-3}$) | $\beta$ | $R_{CT}$ ($mm\,d^{-1}$) |
|---|---|---|---|---|---|---|
| TO1 | 2008-07-16 | 505, 515, 515 | 18.3, 18.3, 18.3 | 127, 115, 146 | 3.20, 3.07, 2.91 | 0.84, 0.76, 0.75 |
| TO2 | 2008-07-17 | 505, 515, 465 | 18.3, 18.3, 14.7 | 91, 110, 110 | 2.59, 2.50, 2.72 | 0.44, 0.59, 0.30 |
| TO3 | 2008-07-19 | 455, 475, 455 | 14.7, 14.7, 14.7 | 159, 201, 242 | 2.43, 2.52, 2.45 | 0.46, 0.56, 0.64 |
| TO4 | 2008-07-21 | 975, 955, 925 | 26.2, 26.2, 24.4 | 46, 53, 37 | 3.06, 3.15, 2.74 | 0.95, 1.34, 1.34 |
| TO5 | 2008-07-28 | 426, 415, 505 | 17.0, 18.3, 18.3 | 59, 82, 92 | 3.12, 3.05, 2.93 | 0.19, 0.36, 0.39 |
| TO6 | 2008-07-29 | 655, 585, 535 | 18.3, 18.3, 18.3 | 165, 144, 137 | 3.19, 2.86, 2.71 | 0.77, 0.59, 0.46 |
| TO7 | 2008-07-30 | 325, 345, 315, 365 | 28.2, 24.4, 24.4, 24.4 | 27, 24, 28, 34 | 3.03, 2.88, 2.71, 2.86 | 1.27, 0.92, 1.01, 0.73 |
| TO8 | 2008-08-01 | 365, 385, 425, 285 | 26.2, 21.2, 30.3, 21.1 | 19, 17, 15, 38 | 2.65, 1.75, 3.21, 2.24 | 0.96, 0.89, 1.15, 0.48 |
| TO10 | 2008-08-04 | 633, 645, 585 | 18.3, 18.3, 14.7 | 130, 106, 100 | 2.54, 2.59, 2.31 | 1.01, 0.70, 0.54 |
| TO11 | 2008-08-06 | 496, 575, 555, 515 | 12.8, 12.8, 12.8, 12.8 | 74, 115, 116, 111 | 2.82, 3.37, 3.27, 3.10 | 0.09, 0.12, 0.13, 0.13 |
| TO12 | 2008-08-08 | 704, 725, 685 | 16.4, 17.0, 16.4 | 103, 118, 124 | 3.42, 3.34, 3.11 | 0.29, 0.36, 0.29 |
| TO13 | 2008-08-09 | 555, 605, 635 | 28.2, 28.2, 26.2 | 26, 29, 32 | 3.43, 3.23, 3.84 | 1.35, 1.42, 1.69 |
| TO14 | 2008-08-12 | 495, 495, 495 | 24.4, 24.4, 24.4 | 64, 78, 56 | 3.05, 3.09, 3.17 | 1.46, 1.68, 1.79 |
| TO15 | 2008-08-13 | 415, 435, 475 | 18.3, 17.0, 18.3 | 55, 80, 79 | 2.33, 2.45, 2.40 | 0.58, 0.60, 0.76 |
| TO16 | 2008-08-14 | 395, 435, 425 | 22.7, 22.7, 21.9 | 59, 54, 62 | 3.21, 2.97, 3.09 | 0.91, 0.80, 0.74 |
| TO17 | 2008-08-15 | 415, 405, 435 | 21.1, 21.1, 21.1 | 86, 68, 80 | 3.16, 2.96, 2.81 | 0.92, 0.49, 0.64 |

Table 3.1: Microphysical characteristics of POST flights calculated from top 40 m of cloud. Order of values corresponds to leg number. Monomer diameter $d_0$, total concentration $N_D$ and slope parameter $\beta$ calculated from PDI only.

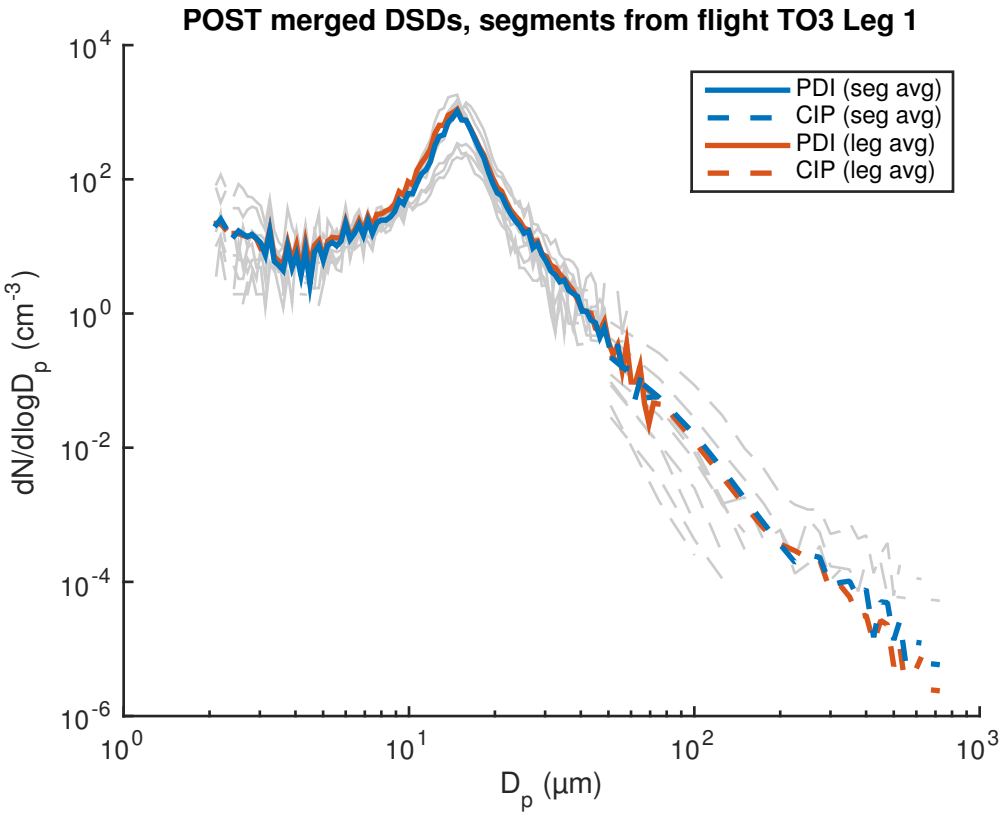



Figure 3.1: Typical DSD observations from both cloud probes (PDI and CIP) from TO2 Leg 1. Despite the relative smoothness of the leg composite DSD for $D_p > 10\,\mu m$ (average over 30 km, red traces), note the variability in the segment DSDs (averaged over 1.5 km, gray traces). There is an overlap size region in which both instruments measure (25-100 μm; first CIP bin measuring drops smaller than 50 μm not shown). In the mean these observations overlap but this is not true of most individual segments. Discontinuities are primarily due to the low probability of observing "large" drops in the PDI view volume.

We assume that a leg-mean DSD can be interpreted as the steady state distribution representative of the mean state of the cloud top region. The mode diameter of the DSD represents the maximum size to which drops may grow by condensation and all drops smaller than the mode diameter are assumed to grow by condensation alone. Conversely, for drops larger than the mode diameter condensation is assumed negligible and all growth is due to collision-coalescence. Sedimentatation, evaporation due to entrainment mixing and drop breakup are neglected. The drops considered here ($d < 100\,\mu m$) are too small for breakup to be important and the validity of the choice to neglect evaporation and sedimentation will be addressed in Section 3.4.4.

Next we assume that all collisions involve a drop of about the mode size $d_0$ (henceforth termed "monomers") and rebin the DSD assuming all drops larger than the mass $m_0$ of monomer-sized drops are formed by a linear combination of monomers. These assumptions are based on the dominant number concentration of near-monomer-sized drops and have the benefit of minimizing the number of closure parameters necessary to estimate collision rates. The validity of the assumptions will be evaluated in Section 3.3. We place all drops of mass $[\frac{1}{2}m_0, \frac{3}{2}m_0)$ in the first bin. The remainder of the right tail of the DSD is further rebinned by integer multiples of the monomer mass $(i+1)m_0$ with bin width $[(i+\frac{1}{2})m_0, (i+\frac{3}{2})m_0)$. Power law fits to the right tail of the observations are used to initialize the box model (see Section 3.3.1).

### 3.2.3 Estimating rate constants from a DSD

A simplified collisional growth equation can be given by:

$$\frac{dn_i}{dt} = k_{i-1}n_0n_{i-1} - k_in_0n_i \tag{3.1}$$

where $n_i$ is the concentration of drops in the *i-th* bin and $k_i$ is the rate constant for collisions between monomers and drops in bin $i$. This equation excludes collisions between non-monomers. When applied to observations, we assume the drop size distribution is at steady state such that $\frac{dn_i}{dt} = 0$. This results in a linear system of $n$ equations with $n+1$ unknowns. To close the system, we specify $k_0$ which can be

interpreted as a source term to replenish monomers lost by collision. Further details about the analytical framework are contained in Appendix A.

It is important to stress that we have intentionally chosen the term "rate constant" rather than "collision kernel" to describe the quantity estimated. This is because a) we have (by assumption) neglected the majority of collision possibilities in order to reduce the number of closure parameters necessary, b) the kernel fundamentally depends on local concentrations but the rate constant analysis is applied to observed DSDs averaged over ones to tens of kilometers and c) conceptually, the quantity is more accurately framed by the "rate constant" terminology with which chemists are familiar: it depends solely on number concentrations without reference to any physical mechanism, while the collision kernel is rooted in the physics of the collision-coalescence process.

## 3.3 Validation against a collision box model

### 3.3.1 Description of the model

Before applying the rate constant analysis to observations, we characterize the rate constant using known DSDs and collision rates. We use the zero-dimensional collisional growth model of *Bott* [1998] (hereafter referred to as the Bott model) to derive rate constants and compare various formulations of the collision kernel. The initial DSD closely matches the observations: for drops of $m < 1.5m_0$, the distribution is lognormal centered at $d_0$ with $\sigma = 1.2$; drops with $m \geq 1.5m_0$ follow a power law with slope parameter $\beta$ as fit to the observations. The model was run for each observed pair of $d_0$ and $\beta$ with all collisions allowed (i.e. including collisions between non-monomers) and the monomer number concentration is held constant. The assumption that allowing all collisions does not unduly affect results will be addressed in the next section.

For later comparison with both theory and observations, the model was run with two different collision kernels: the Hall and Ayala hydrodynamical collision kernels [*Hall*, 1980; *Ayala et al.*, 2008b]. The Hall kernel assumes quiescent background flow while the Ayala kernel takes turbulence into account in the calculation of collision

efficiency, radial relative velocity, and a clustering coefficient that describes deviations from uniform random spatial distribution. These effects are parameterized according to *Ayala et al.* [2008b] as nonlinear functions of the turbulent energy dissipation rate $\epsilon$. At the lower limit of quiescence, the Ayala kernel reduces to the Hall kernel. Here the Ayala kernel is calculated for discrete values of dissipation rate relevant to shallow clouds, $\epsilon = \{3, 10, 30, 100, 300\}\,\mathrm{cm^2 s^{-3}}$.

### 3.3.2 Derived rate constants

The Bott model gives drop concentration as a function of time. Using Equation 3.1, rate constants are calculated. The closure parameter $k_0$ is taken as the maximum intrabin kernel value for the 0th bin such that $k_0 = K(0.5m_0, 1.5m_0)$ where uppercase $K$ indicates the collision kernel. This is the most conservative choice of $k_0$ and minimizes derived observational rate constants (see Section 3.4.4). Computed rate constants from all POST legs using the Hall kernel are shown in Figure 3.2 as a function of "collector drop" diameter $D$, where $D = d_0 i^{1/3}$.

Rate constants are lowest for the first collision and increase significantly (by 1-4 orders of magnitude) with collector drop size. This is expected because kernel values are at a minimum for collisions of similar size drops due to low relative velocity. In addition, the rate constant magnitude correlates positively with monomer size and negatively with slope parameter. Results using the largest calculated kernel values (Ayala kernel with $\epsilon = 300\,\mathrm{cm^2 s^{-3}}$, hereafter A300) are qualitatively similar, with rates about 2-5 times greater across all collector drop sizes (see inset, Figure 3.2). Rate constants using intermediate values of the Ayala kernel display similar behavior with values that fall in between the extrema of dissipation rate (Hall and A300).

While the behavior of these cases instills confidence that the rate constant analysis retrieves a quantity of some relevance to the collision process, the benchmark test is to compare with the kernel values used to drive the Bott box model. The calculated rate constants were divided by kernel values corresponding to discrete pairs such that $K_i(i > 0) = K(m_0, m_i)$ for each collision kernel realization. Results for the Hall kernel

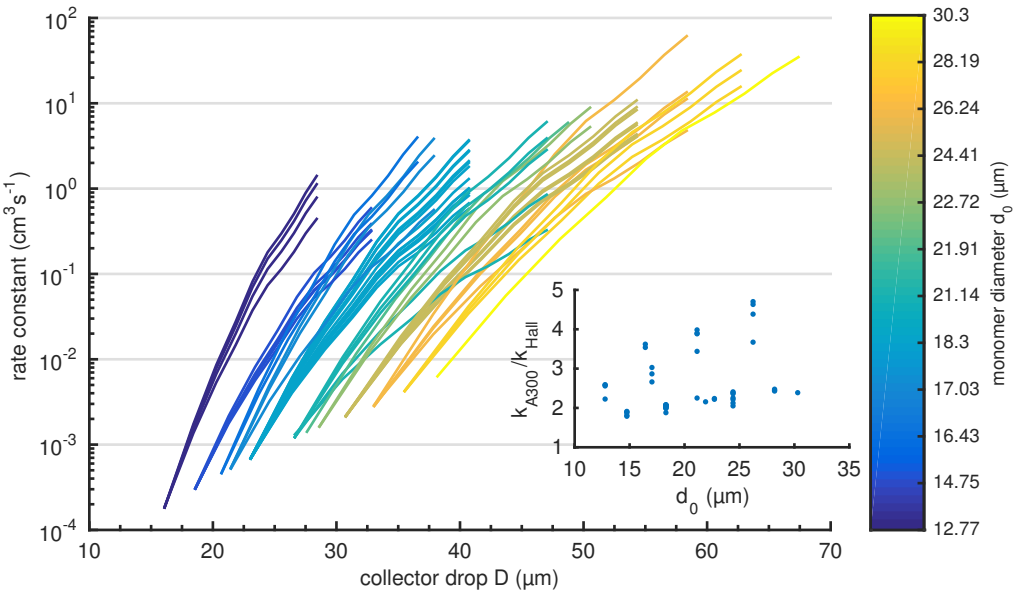



Figure 3.2: Rate constant as a function of collector drop diameter from the Bott model using the Hall kernel. Color coding is by monomer diameter, showing a strong relationship between monomer size and rate constant. Inset shows the ratio of rate constants derived using A300 versus the Hall kernel as a function of monomer diameter.

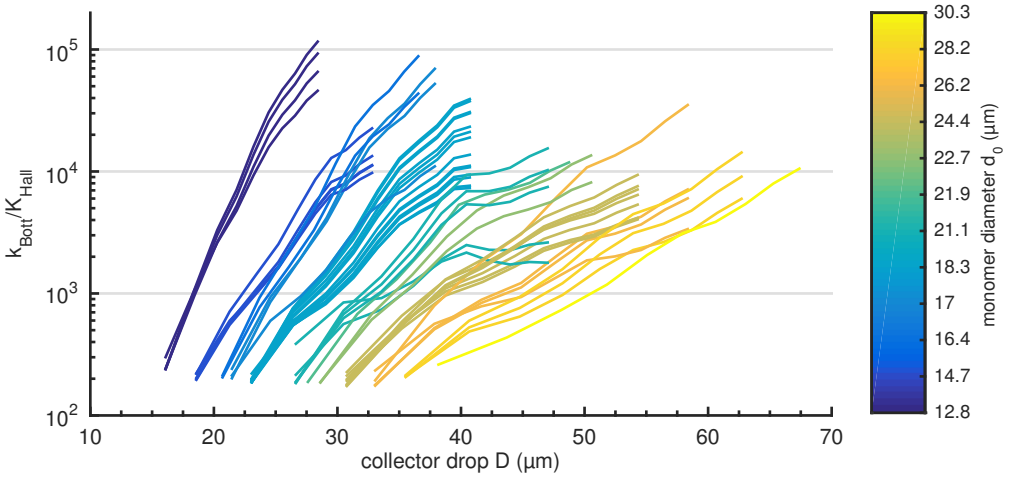



Figure 3.3: Bott model rate constants relative to corresponding Hall kernel values. Rate constants increase much faster than kernel values with increasing size differential.

output are shown in Figure 3.3. Results of comparison of Bott model rate constants with the Ayala kernel are relatively invariant with respect to the Hall kernel results: any particular $k_i/K_i$ typically varies by less than a factor of 2 and overall by less than a factor of 10, hence the Ayala kernel comparison is not shown. Variability is due to the nonlinear nature of the Ayala kernel. This lack of variability between kernel realizations is another indicator that the rate constant analysis captures real variability in collision rates.

It is immediately apparent from Figure 3.3 that rate constants are much greater than kernel values for all collision pairs. As such, the rate constant cannot be used interchangeably with a collision kernel, but this result is expected for several reasons. First, it must be reiterated that rate constants are calculated using number concentrations while kernel values are derived from physical principles. Thus there is no *a priori* reason that they should be expected to be equal. Second, the Bott model uses interpolated kernel values for discrete drop pairs while the rate constant analysis bins together multiple discrete pairs. The final division by kernel values then returns to the discrete pair framework, but uses drop sizes and concentrations that bear little resemblance to those used in the model. Furthermore, the pairs used for the theoretical kernel predictions in

the final comparison step do not necessarily correspond with the average drop size in the monomer-relative rebinning scheme, an additional source of error. A more accurate method would be to generate comparison kernel values as they are calculated in the model (i.e. interpolate over a nearest-neighbor stencil) and integrate over all possible collisional pairs weighting by concentration.

The contribution of collisions of non-monomers to changes in concentration in the analyzed size range must also be considered. It is tempting to interpret the increase of $k_i/K_i$ with increasing $D$ in Figure 3.3 as evidence of this, but the assertion cannot substantiated by the shape of the curves alone. As a more rigorous test, the Bott model was run with only monomer collisions permitted and the resulting rate constants compared with the "all collision" model output. Deactivating non-monomer collisions changed calculated rate constants by less than 1% for all kernels tested over relevant time scales (not shown). Differences between "all collision" and "monomer only" runs decrease with increasing turbulence as the collision rates of similar-sized drops increase more for pairs of small size differential than for pairs of substantially different size, all other things being held equal.

In the Bott model, collision-coalescence is the only process modifying the drop size distribution. The rate constants calculated from model output transform a theoretically derived collision kernel into an observable quantity, with no added uncertainty due to other physical processes. Therefore, when the rate constant analysis is applied to the observations we will scale the results by the Bott model output to compare observed rate constants with the "collision-only" rate constants derived from the Bott model. This allows us to quantitatively evaluate the role of collision-coalescence in shaping observed DSDs.

## 3.4 Results

### 3.4.1 Closure assumption

When applying the rate constant analysis to observations of the cloud top DSD, we define the closure parameter $k_0$ as the monomer source rate balancing the loss of drops to higher bins. We interpret this as the vertical rate of advection of monomers to the cloud top region. Given a mean updraft velocity $\overline{w_\uparrow}$ (defined as mean $w > 0.01\,\mathrm{ms}^{-1}$), cloud top layer of thickness $h$ and mean monomer concentration $n_0$ just below the cloud top layer, the monomer source rate is given by $k_0 = \dfrac{\overline{w_\uparrow}}{n_0 h}$. A cloud top layer of thickness 40 m is chosen. Mean updraft velocity and $n_0$ were diagnosed using data from 40-80 m below cloud top to calculate leg-specific $k_0$ values, which range from $3.4 \times 10^{-5}\,\mathrm{cm}^3\mathrm{s}^{-1}$ to $4.9 \times 10^{-4}\,\mathrm{cm}^3\mathrm{s}^{-1}$ with a mean of $1.2 \times 10^{-4}\,\mathrm{cm}^3\mathrm{s}^{-1}$.

### 3.4.2 Estimated rate constants and enhancement factors from leg composites

Estimated rate constants from DSDs averaged over 30 km legs are shown in Figure 3.4 . Rate constants increase with increasing collector diameter. The magnitude of the rate constants generally increases with monomer size (color coding of traces in Figure 3.4), although this size sorting is not perfect. Such sorting is expected because larger monomers collide more effectively all else being equal.

We define the enhancement factor (EF) to be the ratio of the rate constants estimated from observations relative to those calculated from Bott model output. If the sampled volume is uniform (homogeneous DSD) and the kernel is accurate, then we expect the EF to be unity. Deviations from unity may be caused by processes unaccounted for in the Bott model (most notably condensation/evaporation and sedimentation), errors in kernel formulation, or spatial heterogeneity in the DSD. EF with respect to the Hall kernel is shown in Figure 3.5 , with values ranging from 0.1 to 25. EF is inversely related to monomer size, and some of the large monomer cases exhibit values less than unity.

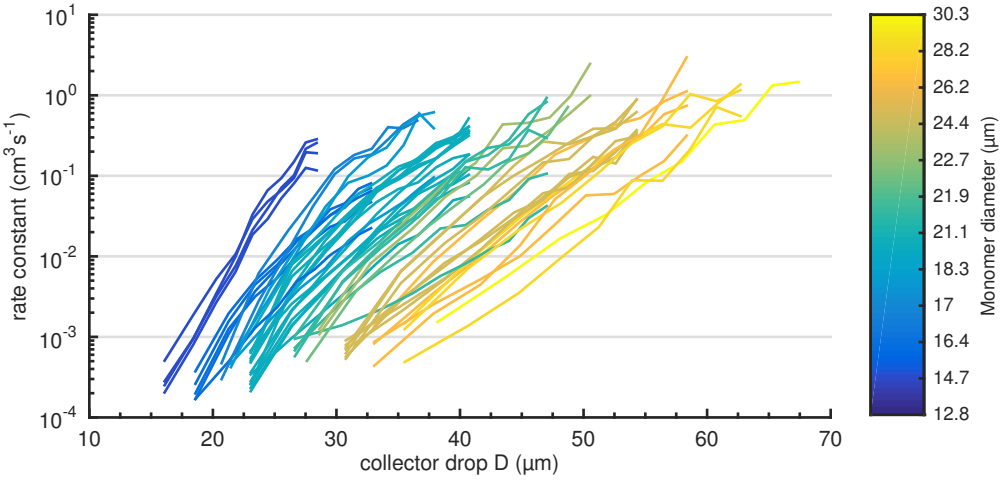



Figure 3.4: Rate constants as calculated from POST PDI observations.

One possible explanation is that we have assumed that the monomer diameter is reached by condensation alone. In reality, collision may alter the shape of the DSD such that the monomer diameter in the absence of collision-coalescence is smaller than the observed mode diameter. This effect will be more pronounced for larger mode diameters.

Correlation tests were performed for enhancement factor and leg-mean liquid water content, rain rate, adiabaticity, and turbulent dissipation rate. No statistically significant correlation was found between any of these quantities and enhancement factor. One leading explanation for EF greater than unity is spatial variability in the DSD. This notion will be further explored in the following section.

### 3.4.3 Enhancement factors from individual segments

The leg composite DSD averages used in the previous section were calculated from 8-10 discontinuous segments. Each of these cloud top segments were about 1.5 km in length for a total of 30 km sampled per leg, which includes time spent above cloud and below cloud top. We now perform the same analysis over each 1.5 km segment to resolve smaller scale heterogeneity in the DSD. Counting statistics preclude analyses

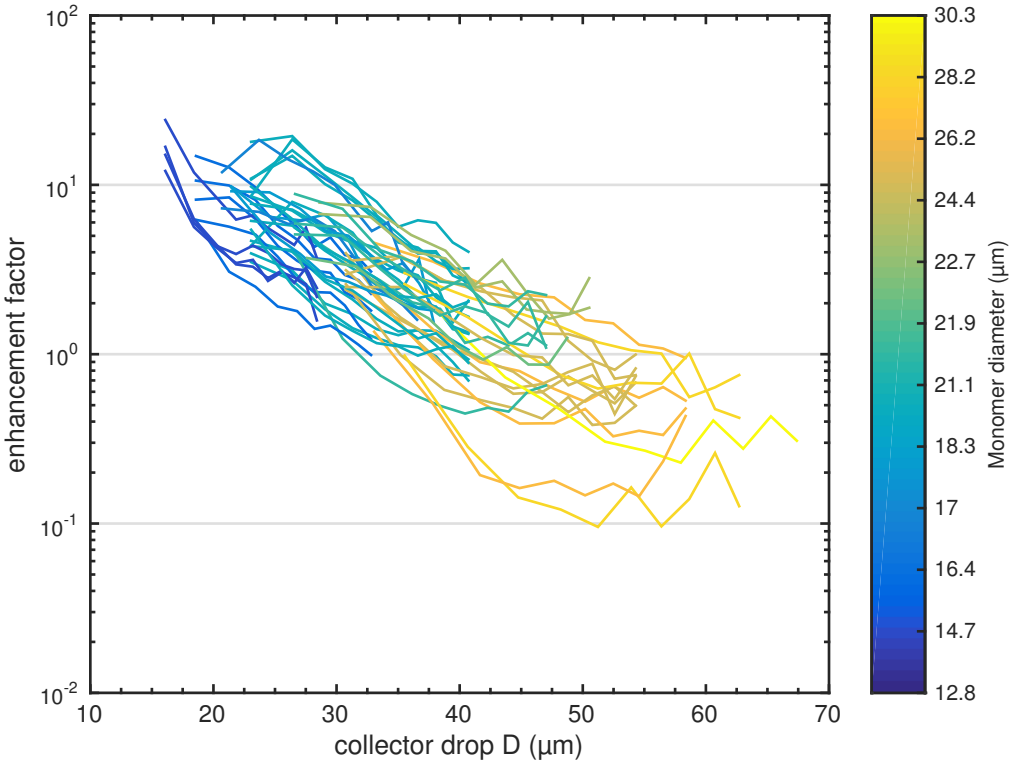



Figure 3.5: Observed rate constants normalized by Bott model output using the Hall kernel. For several of the largest monomer cases, observed rate constants are less than those predicted by the Bott model.

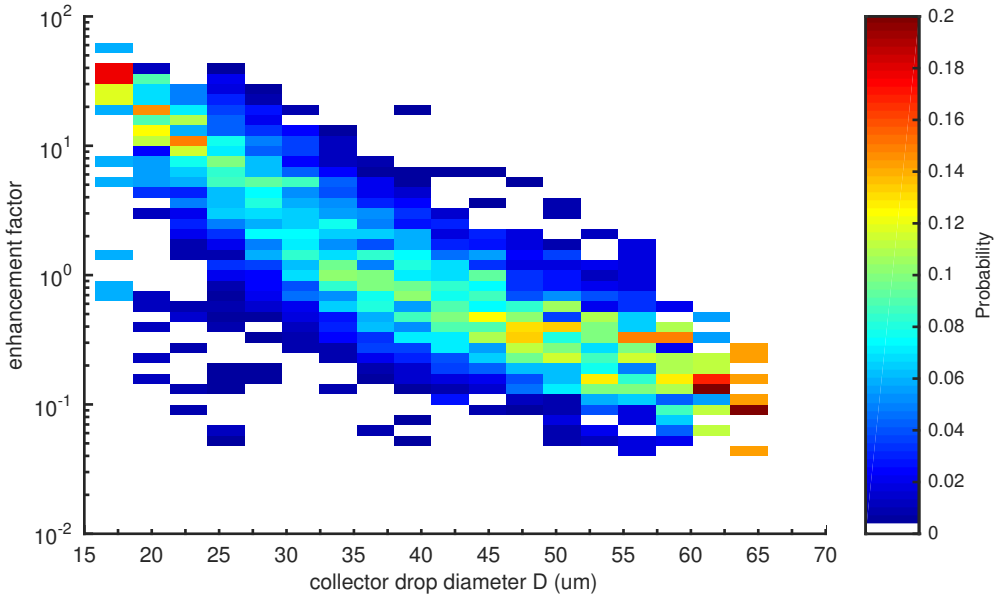



Figure 3.6: Probability density functions of enhancement factor from segments conditioned on collector drop diameter.

at averaging lengths much shorter than this. Segments with mean $LWC < 0.05\,\mathrm{gm}^{-3}$, $N_D < 5\,\mathrm{cm}^{-3}$ or maximum drop size sampled $m_{max} < 8m_0$ are excluded, for a total of 303 usable segments out of 449 total segments from 50 flight legs. Not surprisingly, the population of 303 segments exhibits greater variability than the 50 leg averages in nearly all relevant characteristics of the DSD, e.g. total concentration, mode diameter, and DSD shape parameter $\beta$.

Rate constants and enhancement factors are calculated from segments using leg composite $k_0$ values. Figure 3.6 shows PDFs of enhancement factor relative to the Hall kernel conditioned on collector drop diameter (i.e. Fig. 3.6 does not present a joint PDF; each column sums to unity). Despite the greater diversity in DSDs sampled, segment mean EFs do not exhibit a broader range of values relative to leg mean EFs (cf. Fig. 3.5). Results from both leg composites and individual segments display about an order of magnitude of variability in EF regardless of collector drop size, suggesting that an average over 1.5 km remains too coarse a spatial resolution to accurately describe

collision-coalescence.

The population of anomalously low EF with $D < 25\,\mu m$ are mostly associated with TO10 Leg 3, which was itself anomalous and certainly not at steady state: the cloud was thinning during this leg. We attribute the low enhancement factors with small $d_0$ value to a flattening of the DSD slope as the cloud thinned and the mode diameter became less well-defined. A marked shift in DSD metrics for TO10 Leg 3 as compared to Legs 1 and 2 corroborate this interpretation (see Table 3.1).

### 3.4.4 Sensitivity of results to process representation

Enhancement factors from leg mean DSDs using the A300 kernel are shown in Figure 3.7 . EFs are lower across the board than in Figure 3.3, ranging from $3 \times 10^{-2}$ to 11 with nearly all large monomer cases ($d_0 > 24\,\mu m$) exhibiting enhancements less than unity. Despite the unrealistically high value of dissipation rate in the context of stratocumulus (especially as a mean value over a 30 km leg, *Siebert et al.*, 2010) it is notable that EFs remain of order 10 for several small monomer cases. The large monomer cases are particularly ill-described by this "fastest" realization of the Ayala kernel, requiring a decrease in EFs of up to a factor of 30 to match observations.

The rate constants and enhancement factors presented here should be viewed as lower bounds on actual values. Inclusion of other drop loss processes such as evaporation and sedimentation would serve to increase rate constants because of the steady state assumption: an increase in the rate of drop loss from a bin must be compensated by a commensurate increase in the collisional production rate and therefore rate constants. Mass-weighted sedimentation flux was added to the steady state system of equations to examine the quantitative impact of neglecting this process. Sedimentation increased the resulting rate constants by at most a few percent. This should not come as a great surprise; the largest drops considered in the analyis ($d \sim 65\,\mu m$) have a sedimentation velocity of order $10\,cm\,s^{-1}$.

*Austin et al.* [1995] performed a similar study where they estimated autoconversion rates from observations of marine stratocumulus. They found enhancements up to a

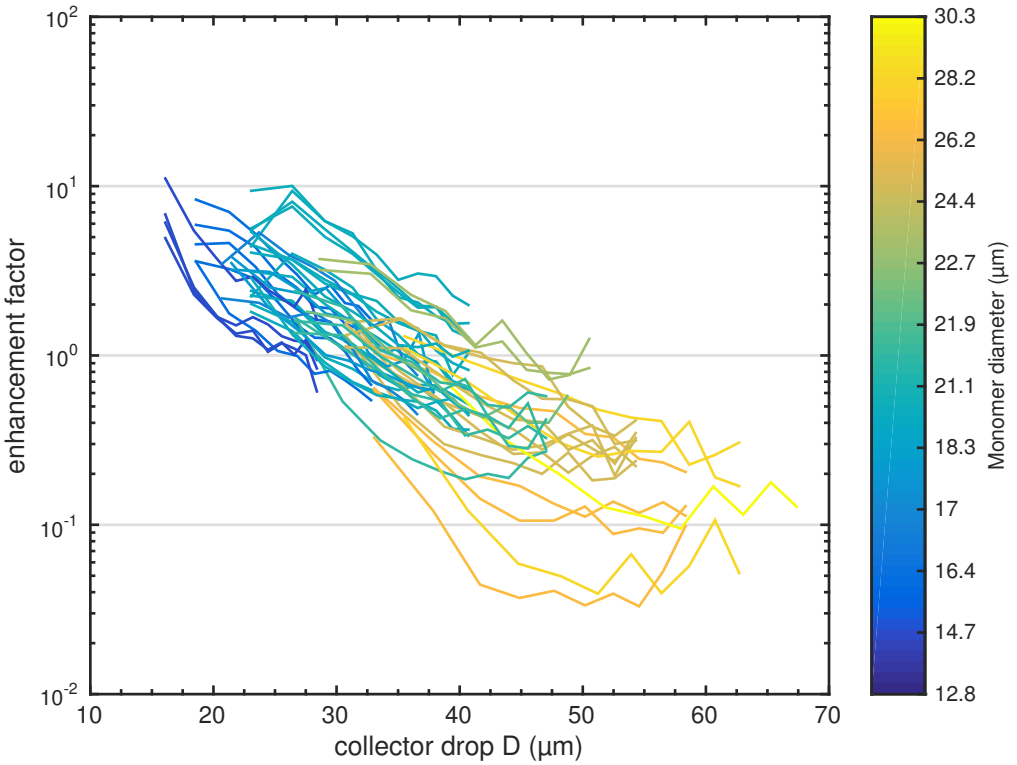



Figure 3.7: Observed rate constants normalized by Bott model output using the Ayala kernel with $\epsilon = 300\,\mathrm{cm\,s^{-3}}$.

factor of 200 were necessary to reproduce the observations. If the same method of calculating $k_0$ from the Bott model had been used for the observations (maximum intrabin kernel value), EFs would be greater by approximately a factor of $10^2$, making these results consistent with those of *Austin et al.* [1995].

## 3.5 Discussion

Aircraft *in situ* observations of the cloud drop size distribution from the POST field campaign were analyzed to retrieve collision-coalescence rate constants in marine stratocumulus. The rate constant framework allows evaluation of the effect of collision-coalescence on the evolution of the drop size distribution by characterizing the size of the DSD by observed mode diameter and assuming the right tail of the DSD to be at steady state. Retrieved rate constants are nondimensionalized by rate constants derived from a collision-coalescence box model using either a quiescent or turbulent hydrodynamic collision kernel to control for variability in mode diameter and DSD shape.

Compared to the quiescent Hall kernel, the rate constant analysis shows that DSDs with a small mode diameter ($d_0 \lesssim 24\,\mu\text{m}$) generally require enhancement factors greater than unity to match theoretically predicted rates while those with a large mode diameter ($d_0 > 24\,\mu\text{m}$) tend to produce drops faster than predicted by theory. The turbulent kernel decreases enhancement factors, but even for an unrealistically high turbulent dissipation rate ($\epsilon = 300\,\text{cm}^2\text{s}^{-3}$) it is unable to bring small mode diameter cases in line with predicted collision rates. This result is robust across averaging distances of $\sim 1.5$ and 30 km, indicating the importance of sub-kilometer scale heterogeneity.

The decreasing relationship between enhancement factor and drop size is a further indictment of the "one size fits all" approach to microphysical parameterization tuning [*Pincus and Klein*, 2000; *Rotstayn*, 2000]. Such an approach may in fact help explain the formation of an aphysical bimodal distribution of precipitation in large-scale models: given a single tuning parameter, a cloudy column may not have a sufficient autoconversion rate to develop precipitation (small characteristic size), or autoconversion may be

too fast and a column will develop stronger precipitation than expected (large characteristic size). In other words, a single uniform tuning parameter will only be relevant to a specific microphysical context.

The results presented in this study generalize the warm rain problem: not only do models have trouble producing precipitation on observed timescales in shallow cumulus, but collision-coalescence is not satisfactorily able to explained observed DSDs even in the lightly or non-precipitating marine stratocumulus sampled during POST. As opposed to the idealized analytical framework developed here, clouds in nature are never at steady state and collision-coalescence does not occur in isolation; rather it occurs simultaneously and continuously with the other microphysical processes affecting the evolution of the DSD. Small variations in radiative cooling, entrainment, and in-cloud turbulence cause inhomogeneities that are not resolved at kilometer length scales that ostensibly allow populations of drops with different histories to interact, perhaps thus increasing the efficacy of collision-coalescence in a manner that we are not presently able to resolve in the observations. This work highlights the need for innovative cloud sampling strategies and instrumentation as currently available aircraft-mounted cloud probes are faced with a tradeoff between statistical significance and physical process relevance due to small sampling volume and the inability to sample a Lagrangian air mass. To evaluate the idea that a length scale of 100 m is sufficient for a "local" description of the DSD, statistically sound observations on length scales shorter than 100 m are necessary.

# Chapter 4

# The role of microphysical spectral resolution on large eddy simulations of marine stratocumulus

## 4.1 Introduction

The evolution of a cloudy boundary layer in a numerical model of the atmosphere is closely tied to the representation of populations of cloud particles therein and the microphysical processes that modify those particles. Two broadly accepted approaches exist to represent microphysical processes [*Khain et al.*, 2015]: (i) bulk parameterizations assume a particular form of the particle size distribution for the various species of hydrometeors represented (liquid drops, pristine ice, aggregates, graupel, etc.) and operate on moments of the distributions; (ii) explicit bin or spectral microphysics schemes subdivide the particle size distribution into discrete size categories and allow each size category to evolve independently. Bulk schemes are computationally efficient due to their reduction of the particle size distribution to a few prognostic variables representing one to three moments of the particle size distribution. Bin microphysics schemes are often orders of magnitude more computationally expensive to run but make no *a priori*

assumptions about the shape of the size distribution and therefore are not limited in relevance to any particular meteorological context because the physics describing the evolution of each size category are universal. Studies seeking to elucidate the effect of specific microphysical processes on the particle size distribution and any potential feedbacks of those processes on the dynamics of the simulations in which the cloud particles are embedded are therefore well-suited to the use of the bin microphysics approach.

A subject which has received relatively little attention over the past few decades is the choice of discretization in bin microphysics schemes, which determines the resolution of the particle size spectrum as well as the number of prognostic variables necessary to represent a given particle size range. For reasons rooted in early observations of clouds [*Defant*, 1905; *Telford et al.*, 1955], straightforward mathematical representation of the underlying physics [*Berry and Reinhardt*, 1974] and computational expedience, size categories are typically spaced by a constant logarithmic factor equal to a doubling of particle mass (such that $m_{i+1} = 2m_i$ or more generally, $m_i = m_0^{2(i-1)}$), although some studies considered the possibility of finer spacing [e.g. *Bleck*, 1970; *Tzivion et al.*, 1987].

The process underlying the choice of mass-doubling bin spacing is the collisional growth of liquid drops, which is thought to be the primary pathway to precipitation in the absence of ice whereby sedimenting drops collide and coalesce to form larger drops. Only liquid phase clouds are considered in the remainder of the study so we will refer to cloud particles as drops and the particle size distribution as the drop size distribution (DSD) or spectrum. The drop size grid of a bin microphysics scheme must encompass the full range of drop sizes attainable by collision-coalescence and is limited only by drop breakup – a range spanning several orders of magnitude in diameter from $10^{-6}$ m to over $10^{-3}$ m. Given such a broad range and finite computing resources, it becomes apparent why a logarithmic binning approach is preferable and rather coarse spectral resolution is acceptable for many applications.

This study's motivation for re-examining spectral resolution also relates to collision-coalescence and precipitation formation, but in the context of comparing numerical

model results with observations. *In situ* observations of the DSD are taken at much finer resolution than in most numerical models. For example, the Artium Flight Phase Doppler Interferometer [PDI, *Chuang et al.*, 2008] measures drops from 2 to 150 μm diameter in 128 bins with a logarithmic bin spacing factor of approximately $2^{1/5}$ in mass space (specifically, $m_{i+1} = 1.14m_i$), which corresponds to about 6 times higher spectral resolution than mass-doubling bins. The drop size range relevant to the onset of collision-coalescence (i.e. the autoconversion regime) is from about 20 to 60 μm diameter; the PDI has 29 bins measuring drops in this size range while a mass-doubling size grid contains only 5 such bins. In order to directly compare PDI observations and standard bin microphysics output, the observations must be rebinned to the coarser resolution of the microphysics scheme and much of the information in the observations is lost.

Ideally, altering model spectral resolution would only affect the computational expense of running a simulation and leave the output relatively unchanged. But this is not necessarily the case because the discretization of the analytical equations driving the collision-coalescence process depends on the spectral resolution [*Tzivion et al.*, 1999]. We will explore the effects of changing bin microphysics spectral resolution in large eddy simualations (LES) of three observationally-based case studies of marine stratocumulus during the POST field campaign [*Carman et al.*, 2012; *Gerber et al.*, 2013]. Model output will be compared from simulations using two different values of the bin spacing factor $p$: the standard mass-doubling resolution ($p = 2$) and a higher resolution that is chosen to be roughly comparable to the size resolution of PDI observations ($p = 2^{1/4}$). Although our eventual goal is to compare simulation output with observations, this is the first study of which the authors are aware that employs enhanced bin spectral resolution in a dynamical model and as such we will focus on differences between the low and high resolution configurations at the expense of validating results against the observations. Our *a priori* expectation is that the DSD should be narrower in the high resolution simulations due to a reduction in numerical diffusion, but that the general outcome of the simulations should not be a strong function of spectral resolution, as the

physics and initial conditions are ostensibly identical to the low resolution simulations.

The remainder of the paper is organized as follows: in Section 4.2 we describe the LES model and modifications made to the model to accommodate enhanced spectral resolution. In Section 4.3 the observational case studies used to derive simulation boundary conditions are briefly examined. We present and compare simulation results in Section 4.4 followed by a discussion of the implications of our findings in Section 4.5.

## 4.2 Model description

The ultimate goal of this study is to implement a high spectral resolution bin microphysics scheme embedded in a dynamical model such that simulation output can be used to quantitatively evaluate the role of turbulence in precipitation formation in warm clouds. LES is a suitable modeling approach for these purposes because it allows assessment of interactions between microphysics and dynamics. We seek to test the hypothesis that changes in spectral resolution do not affect the dynamical state of the boundary layer, therefore fixing dynamics or requiring them as an input as is done in approaches like Lagrangian-Eulerian modeling [e.g. *Magaritz-Ronen et al.*, 2016] is not desirable.

We use the Regional Atmospheric Modeling System (RAMS) version 4.3 in LES mode as described in *Petters et al.* [2013, hereafter P13]. RAMS has been used for numerous studies of stratocumulus microphysics in the past [*Feingold et al.*, 1994, 1996; *Harrington*, 1997; *Harrington and Olsson*, 2001; *Stevens et al.*, 1996a, b, 1998]. The model configuration is nearly identical to that of P13 (see their Table 1) with the exception of boundary conditions, the microphysics scheme and a minor change to the radiation scheme of *Harrington and Olsson* [2001] to accommodate changes in microphysics, as detailed below. Notable differences in configuration from P13 are detailed in Table 4.1. Changes not related to microphysics include refinement of the vertical mesh in the boundary layer, a reduction of the imposed large-scale subsidence rate from $5 \times 10^{-6}\,\mathrm{s}^{-1}$ to $3 \times 10^{-6}\,\mathrm{s}^{-1}$, and different boundary conditions (upper air soundings, sea surface

| Model component | Setting | Notes |
|---|---|---|
| grid resolution | 50 m horizontal, 5 m vertical through inversion top, logarithmically stretched above | finer resolution in boundary layer than *Petters et al.* [2013], onset of logarithmic stretching case dependent |
| domain size | 3.4 km on a side, 1.2 km in vertical | |
| model timestep | 1 s | meets CFL criterion |
| subsidence | $3 \times 10^{-6} \cdot z\,\mathrm{ms}^{-1}$ | $z$ is altitude |
| radiation | binned cloud optical properties | HI run DSD rebinned to mass doubling |
| | upper air soundings | KOAK radiosondes |
| sea surface temperature | constant for each case | NDBC buoy 46042 (Monterey Bay) |
| surface fluxes | constant for each case | see text for calculation method |

Table 4.1: Model configuration and settings for RAMS-LES.

temperature, surface fluxes). The vertical grid resolution was increased throughout the boundary layer because nonphysical discontinuities in fluxes were noted in the cloud layer when a resolution change occurred therein. The subsidence rate used here is lower than that used in past LES intercomparisons of marine stratocumulus based on observations of California stratocumulus ($3.75\times10^{-6}$ s$^{-1}$, *Stevens et al.* 2005; *Ackerman et al.* 2009), but we find the results insensitive to using the higher value. Other deviations from the P13 configuration in our choice of boundary conditions will be discussed in Section 4.3 when the observational cases are introduced.

### 4.2.1 Modifications to microphysics

The microphysics scheme uses the multi-moments method of *Tzivion et al.* [1987]. The default configuration uses 33 mass doubling bins to represent the zeroth and first moments of the drop size distribution (number and mass mixing ratio, respectively) such that the average mass of a drop in a bin is allowed to freely evolve. In addition to the 66 scalar variables necessary to represent the drop size distribution, an additional two scalars are required to hold the number mixing ratio of cloud condensation nuclei (CCN) and vapor excess, for a total of 68 extra scalar variables. For non-precipitating cases, 25 bins (covering 3.125 μm to 1.008 mm diameter) suffice [*Feingold et al.*, 1994]. Simulations using the default bin spacing are denoted LO.

The high resolution size grid increases resolution by a factor of 4 such that the logarithmic spacing factor $p = 2^{1/4}$. A precipitating case therefore requires 132 bins and 266 extra scalar variables and a non-precipitating case requires 100 bins and 202 extra scalar variables. The added expense of running high resolution simulations is significant. Simulations using the high resolution configuration are denoted HI.

The processes represented in the microphysics scheme are activation of CCN, condensation and evaporation, collision-coalescence and sedimentation, all of which depend on drop size and are therefore affected by a change in spectral resolution. Only liquid phase condensate is considered and because this model configuration is not intended to simulate deep convection or heavy precipitation, drop breakup is not represented.

Activation follows the method of *Stevens et al.* [1996a] and is the only microphysical process not directly affected by a change in bin spacing. CCN concentration is held constant throughout a simulation (i.e. no consumption or production), which is a reasonable assumption in the absence of precipitation but is possibly problematic under precipitating conditions because CCN are not conserved due to collisional consumption. We do not explore this possibility here in the interest of simplifying the analysis and interpretation of results as in *Stevens et al.* [1998]. The activation scheme assumes CCN are composed only of ammonium sulfate with a lognormal size distribution centered at $D_p = 0.12\,\mu\text{m}$ and $\sigma_g = 1.5$ [*Xue and Feingold*, 2006b; *Petters et al.*, 2013].

Sedimentation and activation require no major changes in the increased resolution configuration, but those processes describing responsible for changes in drop size (in this case, condensation/evaporation and collision-coalescence) must be more extensively reworked. The vapor diffusion subroutine developed by *Stevens et al.* [1996a] and extended by *Stevens et al.* [1998] is the default algorithm for condensation and evaporation. This subroutine was written assuming mass-doubling bins, therefore we used the analytical condensation and evaporation subroutines of *Tzivion et al.* [1989]. All results presented here use the *Tzivion et al.* [1989] subroutines.

Adapting collision-coalescence for high resolution simulations was considerably more involved. Collision-coalescence is modeled by the Smoluchowski or stochastic collection equation (SCE):

$$\frac{\partial n(x,t)}{\partial t} = -\int_0^\infty K(x,y)n(x)n(y)dy + \int_0^{x/2} K(x,x-y)n(x)n(x-y)dy \qquad (4.1)$$

where $n(x,t)dx$ is the number concentration of drops between size $x$ and $x + dx$ at time $t$ and $K(x,y)$ is the collision kernel which gives the rate of collisions of drops of size $x$ and $y$ per unit volume of air. Discretization of the SCE into $I$ bins according to the method of *Tzivion et al.* [1987] results in a system of equations for the time rate of change of the $J^{th}$ integral moment of bin $k$ of the size distribution of the form

$$\frac{dM_k^J(t)}{dt} = -\sum_{i=1}^{I} \int_{y_i}^{y_{i+1}} n_i(y,t)dy \int_{x_k}^{x_{k+1}} x^J n_k(x,t)K(x,y)dx \qquad (4.2)$$
$$+ \int_{x_k}^{x_{k+1}} x^J dx \int_{x_1}^{x/2} n(x,t)n(x-y,t)K(x,x-y)dy$$

where $n_i$ and $n_k$ are the size distributions in bins $i$ and $k$, respectively, and $x_1$ is the smallest drop size represented. Already, the factor of $x/2$ in the final integral of equation 4.2 naturally suggests that the choice of mass-doubling bins ($p = 2$) will be a special case, and indeed results in the most straightforward discretization. For $p = 2$, the final system of equations for the evolution of the first moment of the DSD consists of 5 integral terms.

The necessity that each integral maps to a single bin requires additional terms for finer spectral resolution than mass-doubling bins because integrals over partial bins must be considered. In the case of $p = 2^{1/4}$, 33 integral terms are required of which 19 integrate over partial bins. The algorithm for collision-coalescence with $p = 2^{1/4}$ used in this work was developed by *Tzivion et al.* [1999] and to our knowledge has not previously been applied in a dynamical model. The calculation of kernel coefficients is also different at high resolution because of the numerous partial bin integrals. Kernel coefficients are calculated offline using the quiescent hydrodynamical kernel of *Hall* [1980] for both low and high resolution simulations and stored in a lookup table for use during the simulations.

Beyond the microphysics routine, a minor modification was also made to the radiation code. The *Harrington and Olsson* [2001] radiation scheme calculates the contribution of condensed phase water to radiative fluxes as a function of the drop size distribution. This scheme was programmed only to accept DSDs with mass doubling bins as input because size-dependent optical coefficients are generated offline and stored in a lookup table. We were unable to obtain the original code to generate new optical coefficients. Therefore the DSD is rebinned to mass doubling resolution for use in the radiation routine. The rebinning is straightforward since the higher spectral resolution

bins are simply a subdivision of the default resolution. Results shown in Section B indicate that differences in radiative properties due to rebinning are negligible.

## 4.3 Case studies

The case studies presented here are derived from the Physics of Stratocumulus Tops (POST) experiment, which took place off the coast of Monterey, California during July and August 2008 [*Carman et al.*, 2012; *Gerber et al.*, 2013; *Malinowski et al.*, 2013]. Research flights sampled a wide range of stratocumulus conditions, from a nascent, optically thin cloud layer measuring less than 100 m deep to heavily precipitating layers over 400 m thick ($R_{CB} \approx 2\,\mathrm{mm\,d^{-1}}$) and flight-mean cloud top liquid water content (LWC) range of 0.2 to 0.6 $\mathrm{g\,m^{-3}}$ [see Table 1, *Gerber et al.*, 2013]. Given such a broad selection of cases from which to select case studies, we attempted to span the observed parameter space while choosing cases that exhibited a minimal change in boundary layer height over the course of the observational period ($|dz_i/dt| < 0.1\,\mathrm{cm\,s^{-1}}$). The latter criterion eliminates all but 4 of the 17 research flights of which one sampled a thin boundary layer of thickness less than 200 m which we also exclude. The remaining 3 flights (2008-07-30, TO7; 2008-08-12, TO14; and 2008-08-15, TO17) were chosen as the basis for the case studies simulated. For the remainder of the paper, the case studies will be referred to by the 4 digit date (MMDD) on which they were flown (i.e. 0730, 0812, and 0815).

The thermodynamic soundings used to initialize simulations of each case are shown in Fig. 4.1 and were calculated as piecewise linear fits to flight-mean observations. The 0730 and 0815 cases were daytime flights (from 10:15 to 17:15 local time) and 0812 an evening/nighttime case (flight from 18:00 to 23:00 local time). The surface potential temperature and moisture are fairly constant among the three cases, clustering around 286 K and 9.6 $\mathrm{g\,kg^{-1}}$, respectively (Fig. 4.1a,b). The inversion and free troposphere structure are more variable across cases, though, with the weakest inversion observed for the 0730 case and the strongest for 0815, with 0812 falling in between. The depth

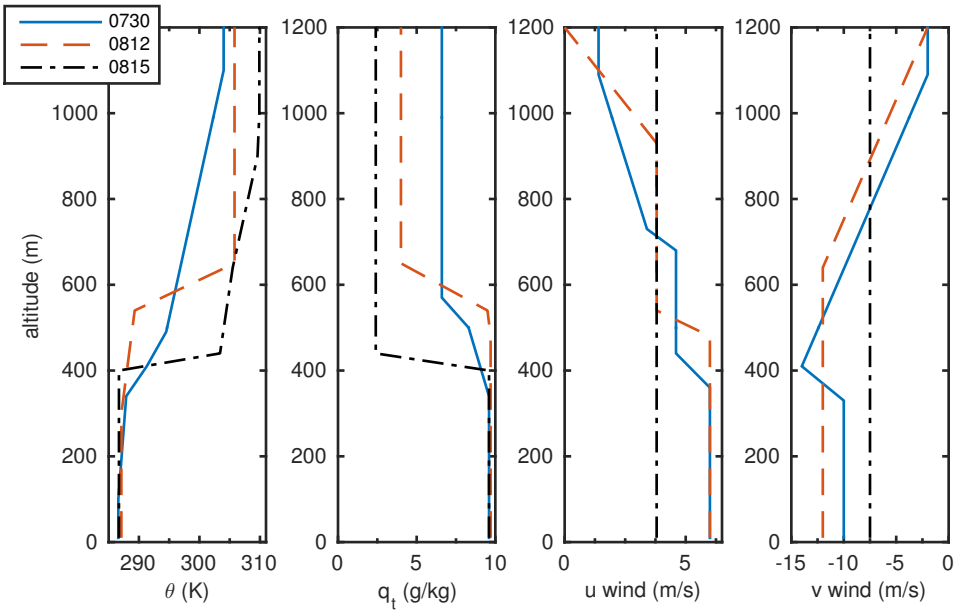



Figure 4.1: Initial soundings. From left to right: a) potential temperature $\theta$, b) total water mixing ratio $q_t$, c) $u$ wind component (west-east), d) $v$ wind component (north-south).

of the boundary layer is also approximately 150 m deeper for 0812 than for the other two cases. None of the cases are strongly shear-driven ($U_s \leq 0.1\ \mathrm{s}^{-1}$) although there are indications of differential advection just above the boundary layer in the 0730 and 0815 cases. Differential advection serves as a continental aerosol source in the 0815 case, where a haze layer was observed just above the boundary layer during the research flight. In the 0815 case, we chose to represent neither the differential advection because it does not cause significant shear nor the increased CCN concentration above the boundary layer because of the crudeness of the activation scheme. The CCN number mixing ratios used for each case were estimated to match the observed total drop concentration within 40 m of cloud top and are shown in Table 4.2.

Surface fluxes of latent and sensible heat were held constant and calculated by assuming that the boundary layer budgets of moisture and sensible heat are closed by the entrainment flux from the top of the cloud. If entrainment is the only diabatic process sinking moisture, this is a reasonable assumption. Each flux is calculated based

| Case | SHF ($Wm^{-2}$) | LHF ($Wm^{-2}$) | SST (K) | $N_{CCN}$ ($g^{-1}$) |
|---|---|---|---|---|
| 0730 | 0.95 | 10.5 | 286.7 | 80 |
| 0812 | 0.95 | 17.6 | 286.1 | 160 |
| 0815 | 0.95 | 15.8 | 285.8 | 260 |

Table 4.2: Boundary conditions for each simulated case. SHF is surface sensible heat flux, SHF is surface latent heat flux, SST is sea surface temperature and $N_{CCN}$ is CCN number mixing ratio

on the temperature and moisture jump of the initial soundings such that $LHF = \overline{w_e q_t'} \approx K \left(\frac{\partial q_t}{\partial z}\right)_{inv} = 0.2 \left(\frac{\Delta q_t}{\Delta z}\right)_{0,inv}$ where K is an eddy diffusivity calculated using the von Karman constant and assuming an entrainment layer depth of 20 m and likewise for $\overline{w_e \theta'}$. Surface fluxes for each case are given in Table 4.2 . Sea surface temperatures were also held constant and obtained from NDBC buoy 46042 observations (located at 36.791 N 122.452 W) at the time of research flight takeoff for each case, also shown in Table 4.2.

RAMS is equipped with a standard "subtropical summer" upper air sounding from *McClatchy et al.* [1971] for radiative fluxes above the model domain (from the maximum model altitude to the top of the atmosphere), but P13 found that using an observationally constrained and locally relevant upper air sounding substantially altered the results of their simulations of SE Pacific marine stratocumulus. Inspection of radiosondes launched from Oakland International Airport (KOAK, nearest radiosonde launch site to POST sampling area) revealed substantial deviations from the *McClatchy et al.* [1971] soundings such that observed soundings often contained a relatively moist layer aloft. Upper air soundings were generated for each case from the KOAK sounding launched closest to the takeoff time of research flights and used in the calculation of upper atmosphere radiative fluxes in the model.

## 4.4 Results

Output from simulations with mass doubling and high resolution bins (denoted LO and HI resolution simulations, respectively) are compared for the three case studies simulated. We begin by comparing bulk thermodynamical properties of the simulations followed by drop size distributions, which are directly affected by increasing spectral resolution, and conclude with a discussion of changes in turbulence-related quantities. A comparison of radiative fluxes can be found in Appendix B. Profiles are derived by averaging over the horizontal domain during the final hour of simulation time at 5 minute intervals. Time series are derived from full domain means at 5 second intervals. In all average profile and time series figures, LO simulations are plotted in blue and HI simulations in red. Differences (profiles and time series) are calculated as $\Delta x = \text{LO} - \text{HI}$ and relative differences are computed relative to the LO simulation, i.e. $\Delta x/x = (\text{LO} - \text{HI})/\text{LO}$. Differences (absolute and relative) are plotted in blue because the LO simulation is the control case against which HI simulation results are compared. All profiles are truncated at 600 m altitude to focus on changes in the boundary layer and because no significant differences above this height are noted in any of the variables examined.

### 4.4.1 Basic characterization of output

The thermal structure of the boundary layer is comparable across resolution in all cases, as shown by the profiles of $\theta$ in Fig. 4.2 . The greatest change between LO and HI simulations is seen in the 0815 case (Fig. 4.2c), where the increase in $\theta$ characterizing the beginning of the inversion is higher in the LO simulations by 20 m for 0815-LO simulation. The opposite is true of the 0812 case (Fig. 4.2b), where the 0812-LO inversion begins 10 m lower than in 0812-HI. The 0730 simulations are within 1 K of each other throughout the depth of the domain. Profiles of total water mixing ratio $q_t$ tell a similar story (Fig. 4.3): the 0730 simulations are nearly indistinguishable; the 0812 case displays a slightly moister boundary layer in the HI simulation above $z = 200\,\text{m}$

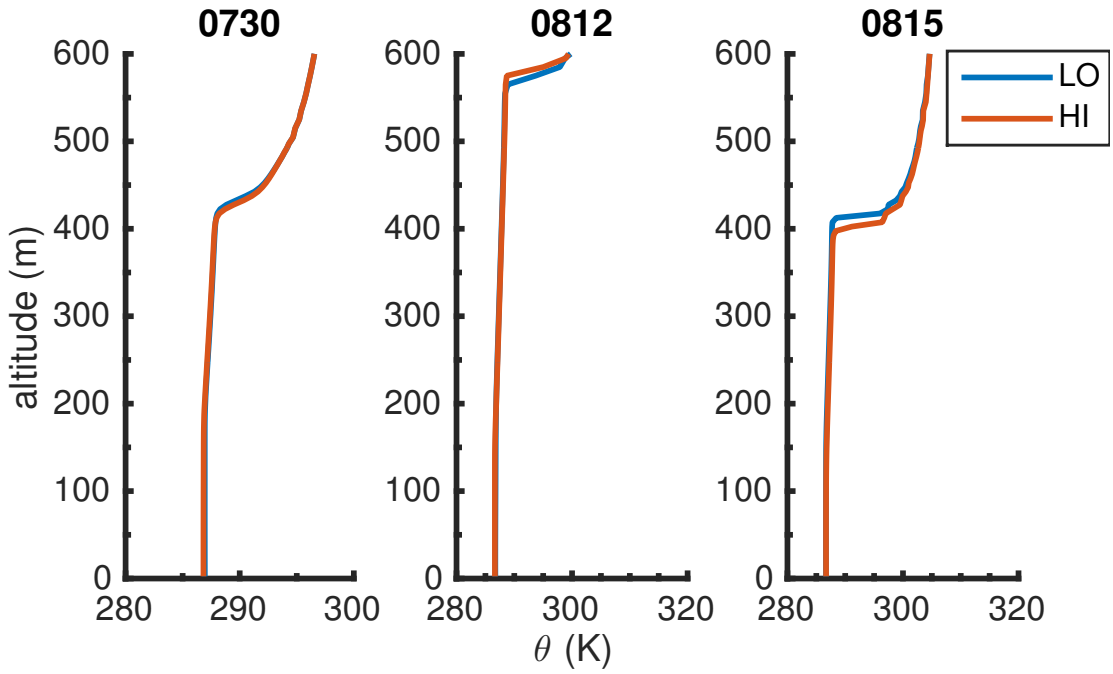



Figure 4.2: Profiles of potential temperature $\theta$

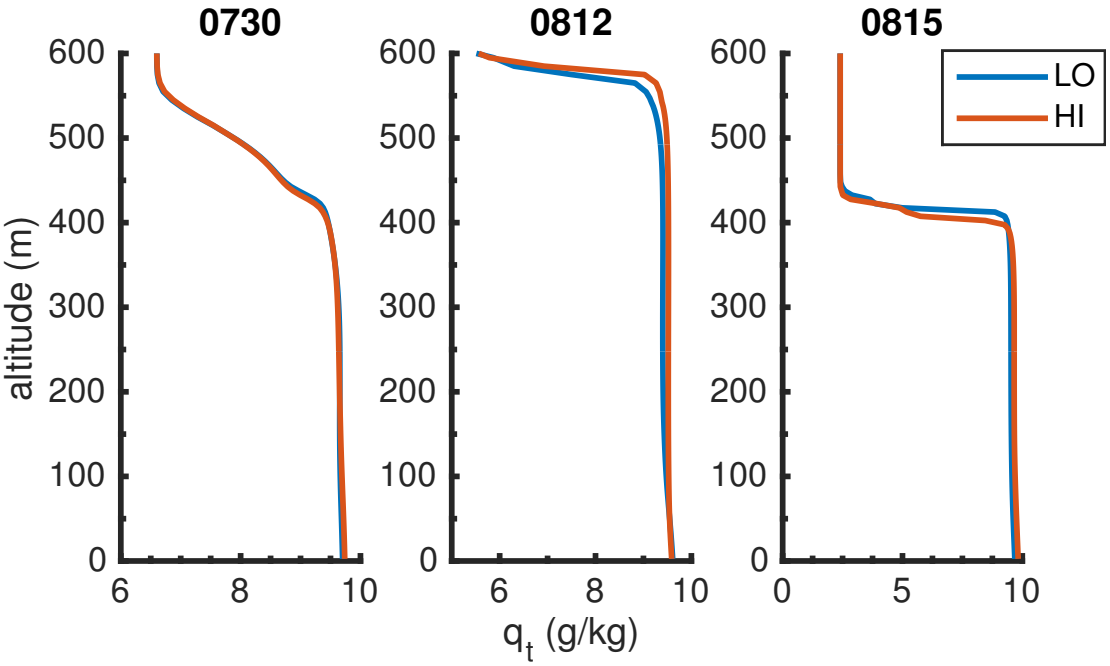



Figure 4.3: Profiles of total water mixing ratio $q_t$

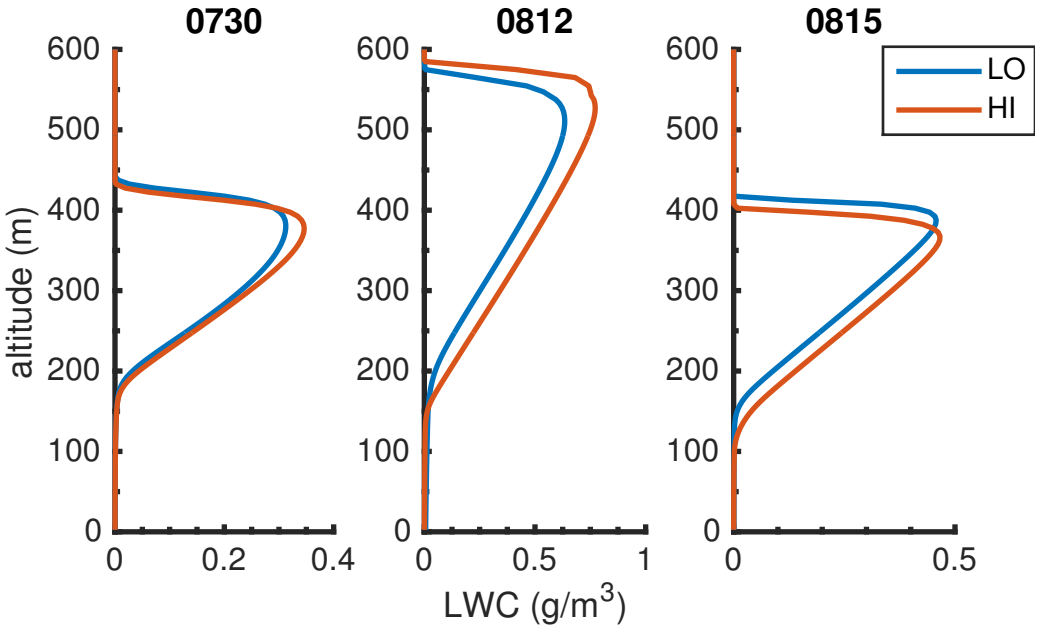



Figure 4.4: Profiles of LWC

and a higher altitude moisture jump by 10 m; and the 0815 case again has a higher altitude moisture jump in the LO simulation by 20 m.

Greater differences are apparent in the profiles of LWC in Fig. 4.4. The 0730 simulations are most similar, displaying only minor differences in LWC throughout the cloud layer (Fig. 4.5a) and making this particular case ideal for direct comparison between the LO and HI resolution simulations. The 0812-HI simulation (Fig. 4.4b) has greater LWC throughout the entire boundary layer. This is a surprising result and will be considered further throughout the remainder of the chapter. The non-drizzling 0815 simulations are also comparable through most of the boundary layer, but 0815-LO LWC peaks at a slightly higher altitude and magnitude than 0815-HI, in line with other evidence for a 20 m deeper boundary layer in the LO simulation. The increased LO simulation cloud top height is matched by an increase in cloud base height. For reference, cloud base and top heights for each simulation are provided in Table 4.3.

Differences in the profiles of LWC are corroborated by time series of LWP (Fig. 4.6). After experiencing a 40% drop in LWP in the first hour after spinup (starting at $t \approx$

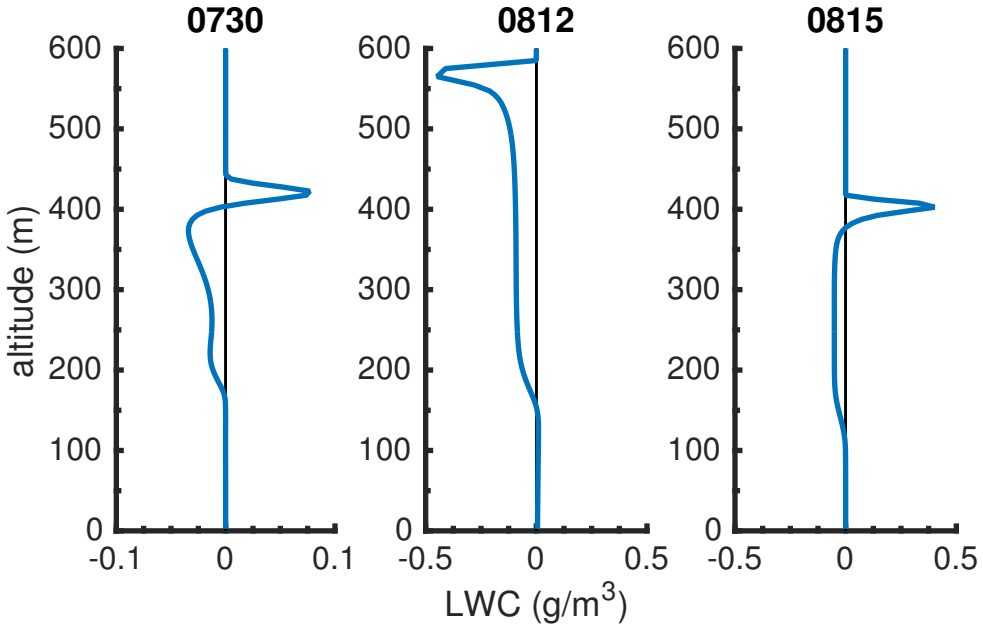



Figure 4.5: Difference profiles of LWC

| Case | Simulation | Cloud base (m) | Cloud top (m) |
|---|---|---|---|
| 0730 | LO | 187.5 | 432.5 |
| | HI | 182.5 | 427.5 |
| 0812 | LO | 182.5 | 565 |
| | HI | 152.5 | 575 |
| 0815 | LO | 157.5 | 412.5 |
| | HI | 127.5 | 397.5 |

Table 4.3: Cloud base and top heights for each simulation, defined as the first and last level with liquid water mixing ratio $\overline{q_l} > 0.01\,\mathrm{g\,kg^{-1}}$

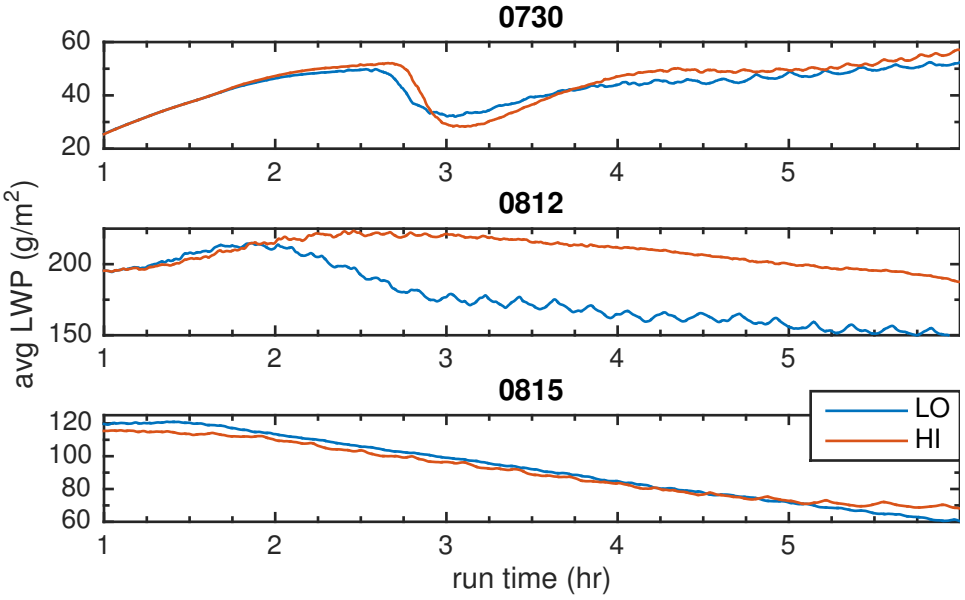



Figure 4.6: Time series of domain average LWP

2.75 hours), the 0730-HI simulation (Fig. 4.6a) has consistently greater LWP over the final 2 hrs of the simulations. The greater LWC in 0812-HI in Fig. 4.4c is clearly seen in LWP as well (Fig. 4.6b), where the difference between 0812-LO and 0812-HI exceeds 40 g m$^{-2}$ for much of the simulation (Fig. 4.7b ). Finally, the 0815 case shows a somewhat more nuanced trend (Fig. 4.6c) in which LWP is higher for 0815-LO for the first 4 hours of the simulation at which point 0815-LO LWP continues to decrease at a nearly linear rate while the decreasing LWP trend in 0815-HI flattens. By the final half hour of the 0815 simulations, the difference in LWP (recall ΔLWP=LO-HI) dips as low as $-10$ g m$^{-2}$ (Fig. 4.7c), a considerable discrepancy considering that LWP at the end of 0815-LO is only about 60 g m$^2$. Such broad variability in the evolution of LWP for the three cases suggests we should expect to find discrepancies among other model variables as well.

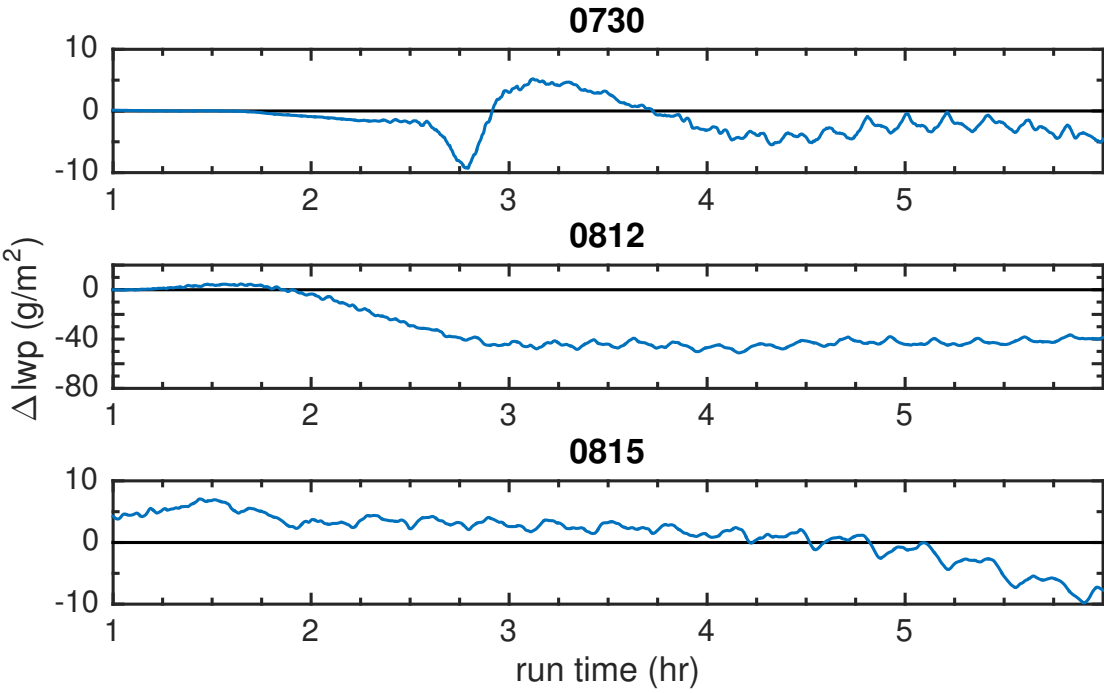



Figure 4.7: Time series of differences of domain mean LWP

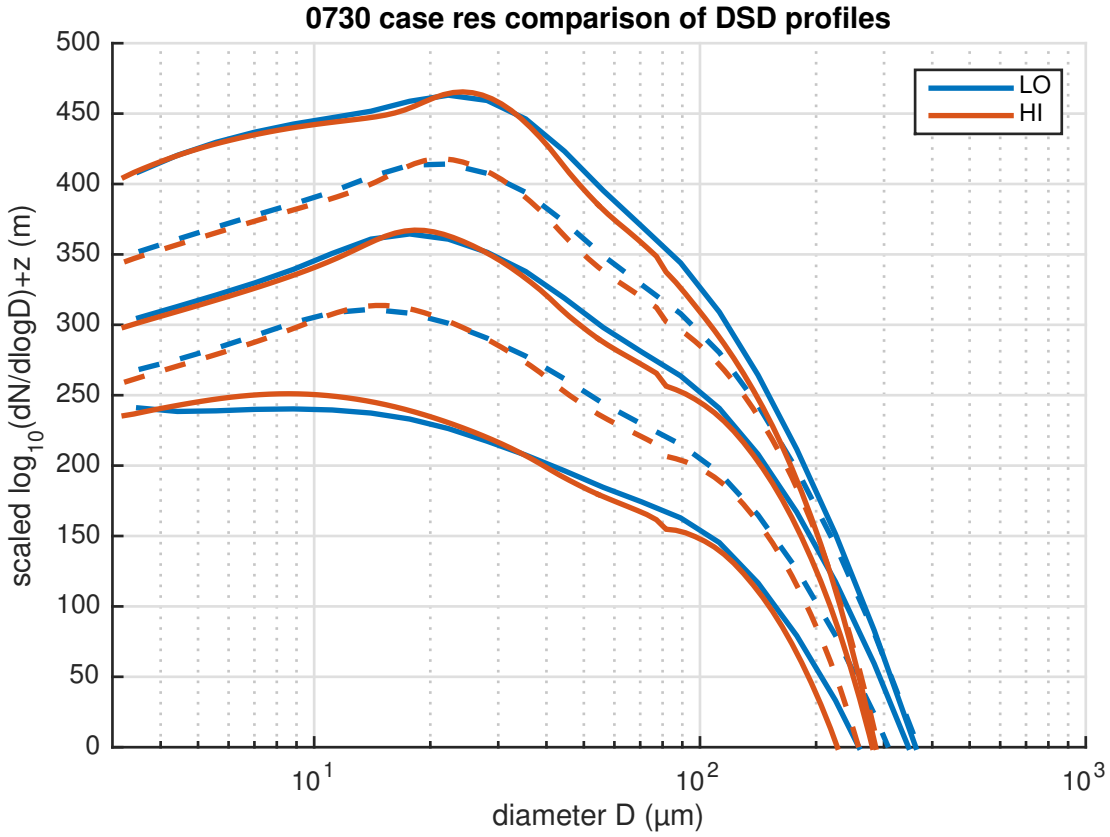



Figure 4.8: Profile of the DSD as a function of altitude at 30 m intervals in cloud ($\overline{q_l(z)} > 0.01\,\mathrm{g\,kg^{-1}}$), 0730 case. Alternating solid and dashed lines for visual clarity. Lowest level plotted is $z = 197.5$ m and the highest level plotted is $z = 397.5$ m.

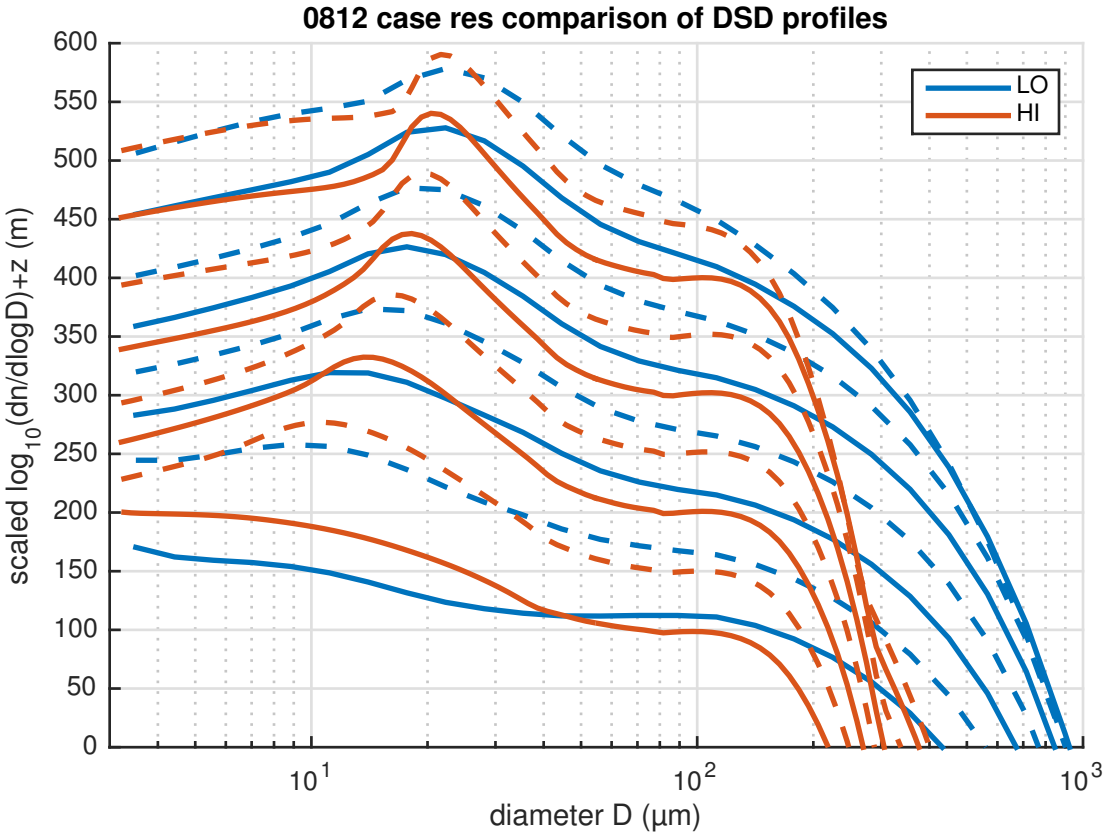



Figure 4.9: Profile of the DSD as a function of altitude at 30 m intervals in cloud ($\overline{(q_l(z)} > 0.01\,\mathrm{g\,kg^{-1}}$), 0812 case. Alternating solid and dashed lines for visual clarity. The lowest level plotted is $z = 147.5$ m and the highest level plotted is $z = 497.5\,\mu$m.

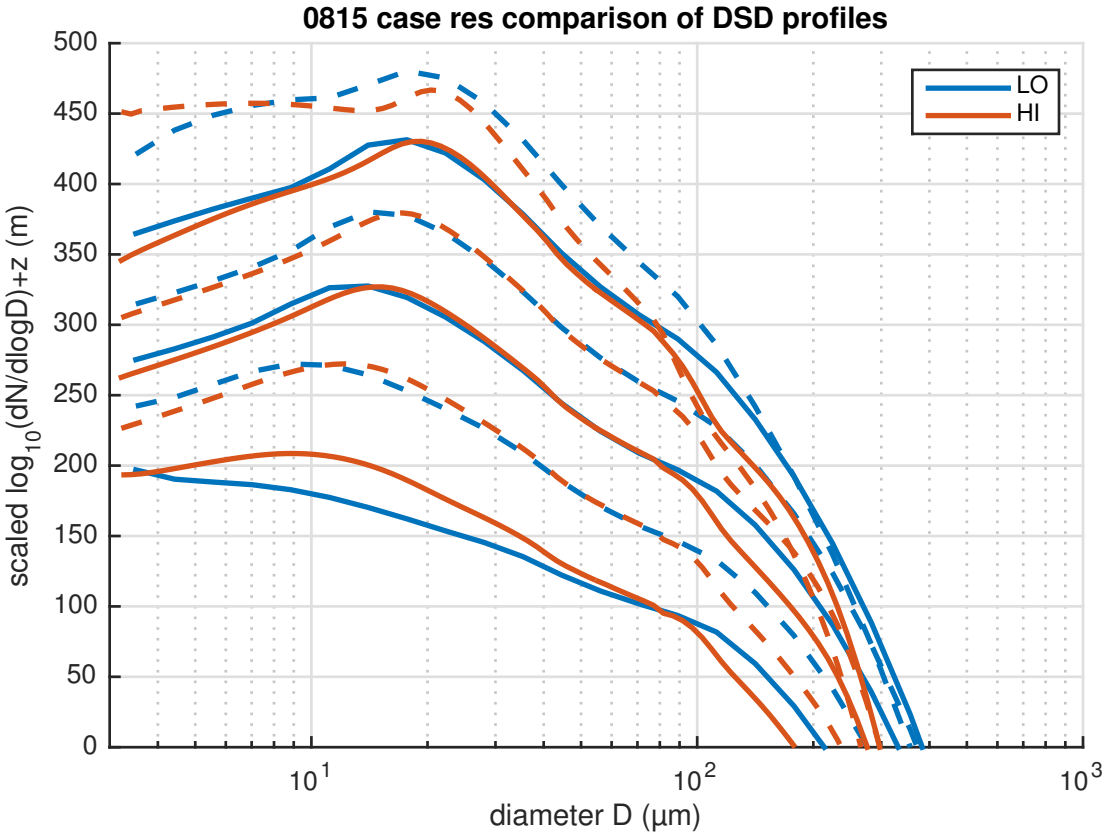



Figure 4.10: Profile of the DSD as a function of altitude at 30 m intervals in cloud ($\overline{q_l(z)} > 0.01\,\mathrm{g\,kg^{-1}}$), 0815 case. Alternating solid and dashed lines for visual clarity. Lowest level plotted is $z = 147.5$ m and the highest level plotted is $z = 397.5$ m.

### 4.4.2 Changes in the drop size distribution

The DSD varies with altitude based on the relative importance of microphysical processes such that qualitative inferences may be drawn from the vertical structure of the DSD. Profiles of the DSD are shown for each case at 30 m vertical intervals in Figs. 4.8-4.10. Several general contrasts can be made between LO and HI resolution simulations for all cases. First, differences in the left tail of the DSD are generally minor. This indicates that condensation is operating in roughly the same manner in the two resolution configurations. Second, the mode of the DSD occurs at a higher concentration and slightly larger size in the HI simulations. The 0815-HI cloud top DSD is an exception, with a larger mode diameter than 0815-LO but lower concentration. This DSD is located at $z = 397.5\,\mathrm{m}$, well within cloud in the 0815-LO profile but at the cloud top level in 0815-HI (Tab. 4.3), where the effects of entrainment mixing are apparent. The high concentrations in the smallest size bins ($D_p < 10\,\mu\mathrm{m}$) are the signature of a well-known problem in LES termed "spurious supersaturation at cloud edge" [*Grabowski*, 1989; *Stevens et al.*, 1996b], which is caused by an "all-or-nothing" approach to condensation in a grid cell that does not allow "partly cloudy" conditions to exist. Secondary activation of CCN occurs as a result, biasing the DSD toward too many small drops. This issue is not related to spectral resolution.

The right tail of the DSD exhibits a much steeper decrease in concentration at higher resolution for all HI simulations. The 0730 and 0815 cases have noticeable right tail discrepancies (Figs. 4.8 and 4.10) while the 0812 case shows markedly different behavior between simulations with a pronounced shoulder between 100 and 200 μm in the HI simulation (Fig. 4.9). Differences due to the coarser size grid used in the 0812-LO simulation cause the formation of large drops (i.e. drizzle) that are not observed in the corresponding HI simulation. This assessment is confirmed by comparison of the profiles of precipitation rate (Fig. 4.11b): the HI simulation obtains a greater precipitation rate at cloud top due to higher LWC, but the LO simulation cloud quickly begins to precipitate more heavily. This occurs because larger drops contribute more than small drops to precipitation rate due to their greater mass, higher fall speed, and

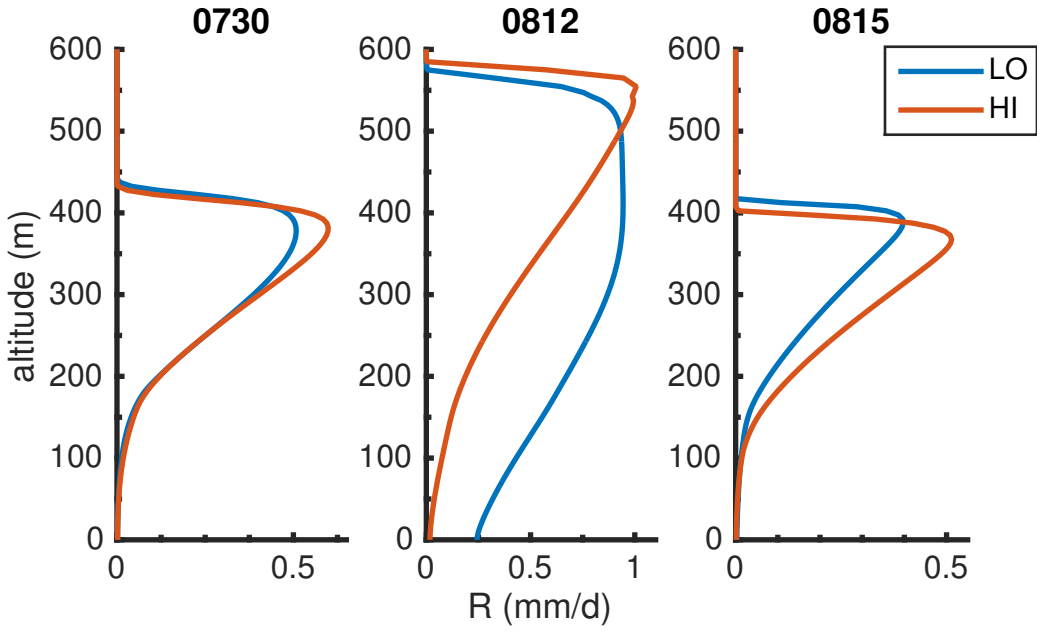



Figure 4.11: Profiles of rain rate $R$

reduced evaporation rate (due to their lower surface area to volume ratio). In the cases without surface accumulation of precipitation (0730 and 0815, Fig. 4.11a,c), the profiles of rain rate are similar, with differences due to the less pronounced discrepancies in concentration in the right tail of the DSD.

Percentile diameters are a useful metric for focusing on differences in a specific feature of the DSD among simulations. The 99th percentile size of the mass DSD ($d_{99}$) can be interpreted as a proxy for the right tail of the DSD, profiles of which are shown in Fig. 4.12. The 0730 case displays no major differences. The 0812 case displays much greater differences, with greater $d_{99}$ in 0812-LO through the bottom ~400 m of the domain. The difference is particularly pronounced below cloud base, where collision-coalescence and evaporation are the only processes modifying the DSD. The increase in $d_{99}$ and the difference between the two simulations suggests that differences in the DSD are primarily due to artificial acceleration of collision-coalescence. In the 0815 case, $d_{99}$ is greater in the HI simulation in the cloud layer yet the LO simulation still has greater $d_{99}$ throughout much of the subcloud layer with some small amount of

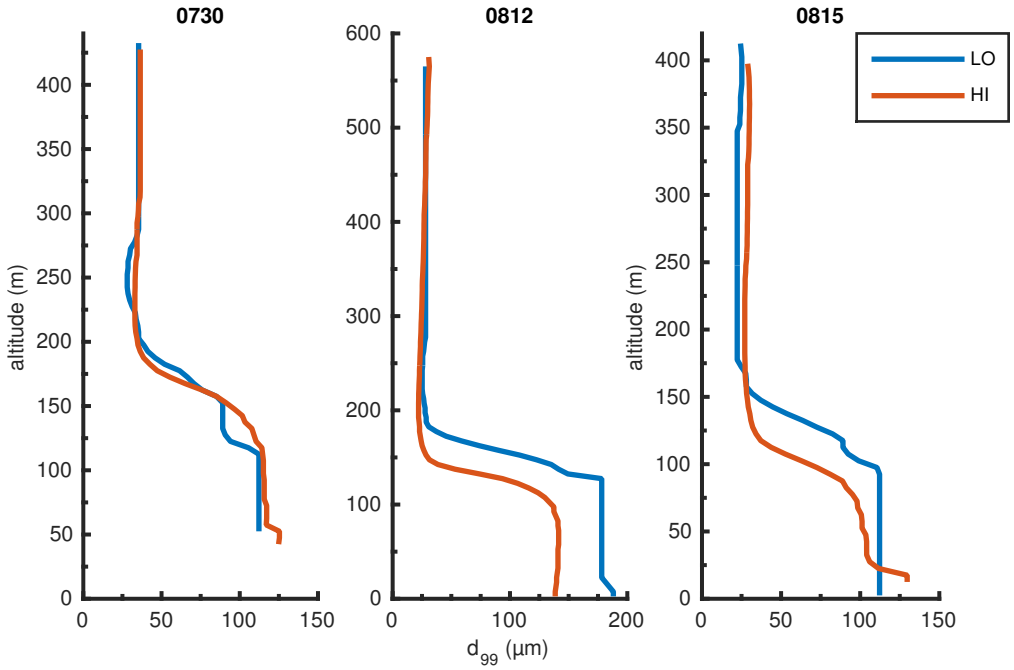



Figure 4.12: Profiles of the 99th percentile size of the mass DSD. Levels with $\overline{N_D} < 1\ \mathrm{cm}^{-3}$ per grid cell are excluded.

surface accumulation, whereas 0815-HI has none.

### 4.4.3 Changes in the vertical structure of turbulence

In the stratocumulus-topped boundary layer (STBL), the cloud is coupled to the surface source of moisture by by turbulent transport. Turbulent kinetic energy (TKE) is primarily generated near cloud top through buoyancy production due to cloud top radiative cooling. In some cases shear production of TKE can be important. Sedimentation of cloud drops has been shown to influence turbulence [*Stevens et al.*, 1998; *Ackerman et al.*, 2004; *Bretherton et al.*, 2007] by altering the partitioning of the TKE budget in the boundary layer. Increasing spectral resolution decreased sedimentation flux in the precipitating 0812 case and increased it in the two non-precipitating cases (0730 and 0815), thus we might expect the vertical structure of turbulence also to have changed. To assess whether changes in DSD discretization affect the structure of turbulence, we begin by comparing profiles of TKE in Fig. 4.13. As with other quantities examined,

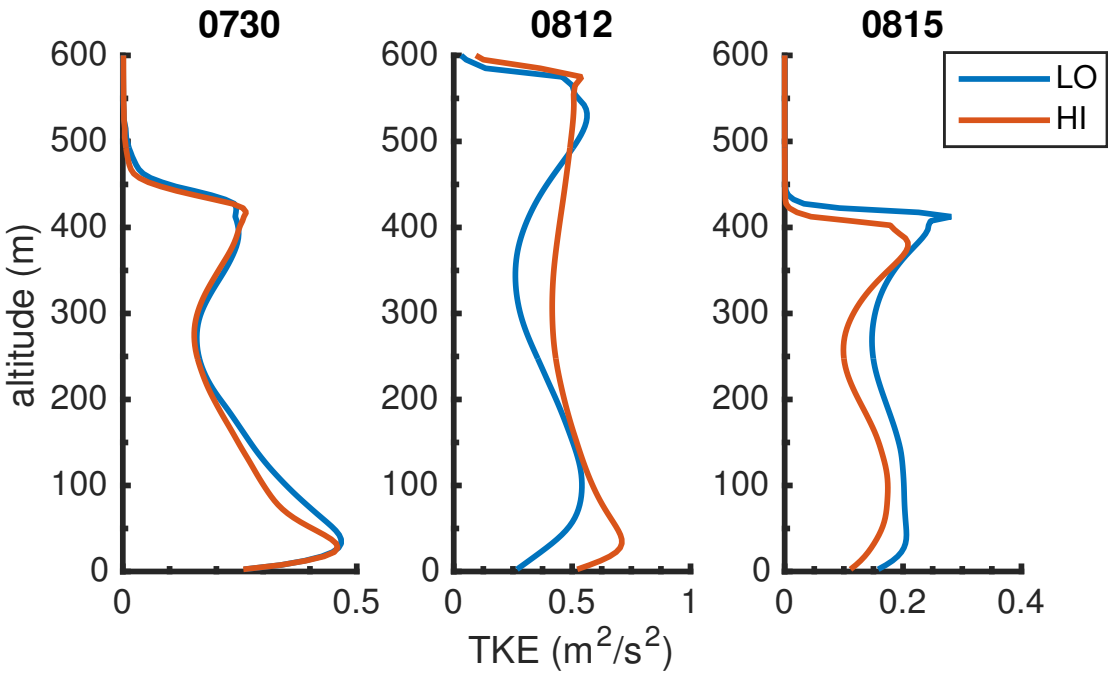



Figure 4.13: Profiles of average TKE

TKE is nearly indistinguishable between the 0730 simulations through much of the boundary layer. In the 0812 and 0815 cases, the changes in the HI simulation are in opposition (higher TKE in 0812-HI, lower TKE in 0815-HI) and where differences are evident in the 0730 case, the HI simulation behaves similarly to 0815-HI. Altogether, these outcomes suggest different responses to changing resolution under precipitating versus non-precipitating conditions.

Differences in vertical TKE structure can be attributed to specific processes by partitioning the TKE budget into its component terms. The time rate of change of TKE for a given altitude layer is given by

$$\frac{dTKE}{dt} = \frac{g}{\theta_0}\overline{w'\theta_v'} - (\overline{u'w'}\frac{d\overline{u}}{dz} + \overline{v'w'}\frac{d\overline{v}}{dz}) - \frac{d\left[\overline{w'(TKE' + p'/\rho_0)}\right]}{dz} - \epsilon \tag{4.3}$$

where the terms on the right-hand side represent, in order: buoyancy production, shear production, turbulent transport and dissipation rate. Strictly speaking, there should also be an advective term, but the mean vertical velocity is negligible in the PBL and thus

this term is omitted. Shear production is negligible for all simulated cases.

Buoyancy production depends on the turbulent flux of virtual temperature, which is defined as

$$\theta_v = \theta(1 + 0.61q_v - q_l) \tag{4.4}$$

and can be thought of as a temperature proxy for density, with warmer values corresponding to lower density air. Buoyancy production is typically at a maximum just below cloud top and is driven by longwave radiative cooling. Positive values of buoyancy production indicate relatively warm parcels ascending and cool parcels descending thereby converting gravitational potential energy into convective motion and, ultimately, turbulent kinetic energy. If such circulations are able to reach the surface, the moisture lost by the cloud layer to entrainment and/or precipitation can be replenished by turbulent fluxes of moisture. If not, the cloud layer is said to be "decoupled" from the surface, and will either dissipate or be replenished in a more intermittent fashion by those surface-driven updrafts strong enough to reach the cloud layer.

Profiles of buoyancy production are shown in Fig. 4.14 and show several robust features in the 0812 and 0815 cases. Starting at the top of the boundary layer, the two cases exhibit buoyancy consumption (i.e. negative buoyancy production) at cloud top due to entrainment (warm air above the cloud being turbulently dragged downwards into the cold boundary layer, which costs TKE). Entrainment consumes more TKE in the LO runs. The expected maximum in buoyancy production is present $\sim 50$ m below cloud top, below which buoyancy production is greater in the LO simulations. This is followed by a crossover near cloud base where the LO simulations again display lower local minima as was the case at the inversion interface. This lowest-altitude minimum is most pronounced in the 0812 case but is also present in the 0730 case, which is otherwise relatively invariant with resolution besides a slight offset in the 0730-HI profile due to slightly lower cloud top height.

The robust response of buoyancy production to increased resolution suggests that changes in the DSD exert a significant effect on this process. The differences near

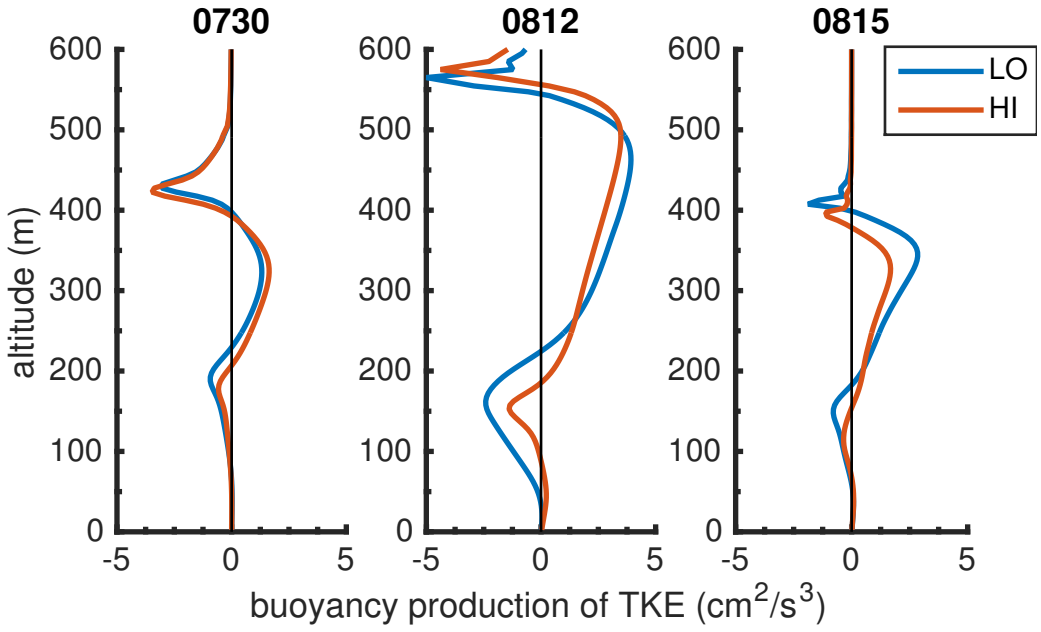



Figure 4.14: Average profiles of buoyancy TKE production

cloud top that lead to greater maximum buoyancy production in the LO simulations can be explained by a coupling of sedimentation and entrainment, an idea proposed by *Ackerman et al.* [2004] and extended by *Bretherton et al.* [2007]. They argue that sedimentation of drops at cloud top reduces entrainment warming which therefore accentuates buoyancy contrasts (i.e. cold downdrafts will be colder). This argument seems most plausible in the 0812-LO case, where $\overline{w'^2}$ (Fig. 4.15) is lower than 0812-HI by a factor of 2 or more throughout the boundary layer (including at cloud top), implying that increased variability in $\theta_v$ rather than turbulence drives the increased buoyancy production, and consistent with the finding that turbulence is less intense in precipitating boundary layers [*Stevens et al.*, 1998]. The observed changes in $\overline{w'^2}$ between simulations are in opposition to the findings of *Bretherton et al.* [2007], who do not find a difference in turbulence when sedimentation is deactivated. We speculate that this is due to their use of a bulk microphysical scheme, which does not allow the more defined size sorting of the DSD caused by sedimentation in a bin scheme.

Negative extrema in buoyancy production at or below cloud base are related to

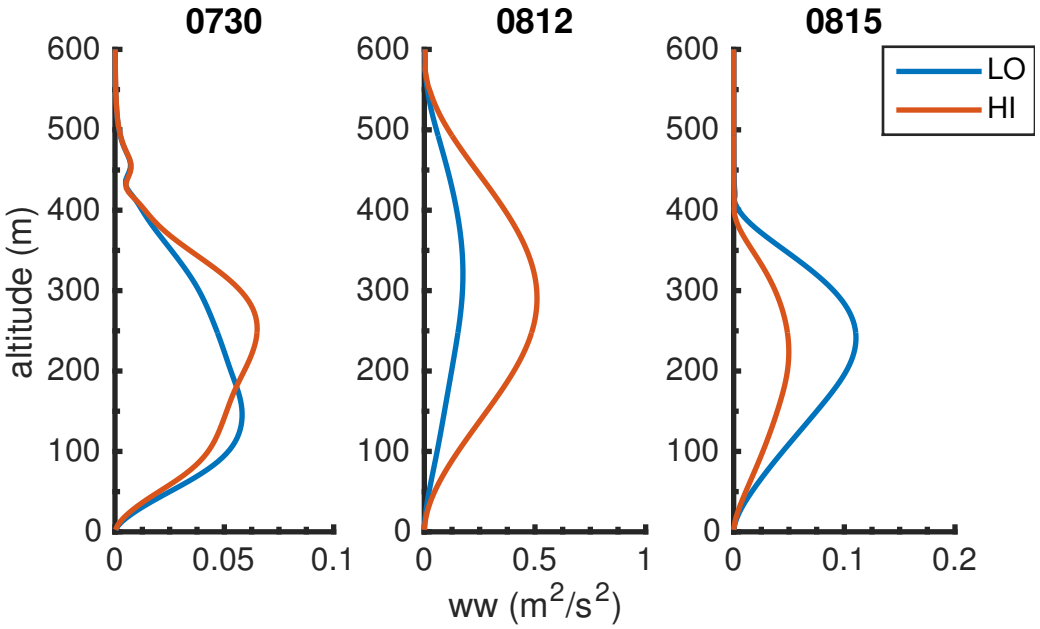



Figure 4.15: Profiles of $\overline{w'^2}$

subcloud evaporation, which causes stratification of the subcloud layer. Even in the absence of surface accumulation of precipitation, sedimentation will cause drops to fall below cloud base. We may then expect a greater cooling for larger drops and/or a drier subcloud layer. Both larger drops and a drier subcloud layer (subcloud layers are on average $-0.02$, $-0.05$, and $-0.1\,\mathrm{g\,kg^{-1}}$ drier for the 0730, 0812, and 0815 LO simulations, respectively) are observed in the LO simulations. Profiles of net latent heating rate in the bottom 300 m of the domain are shown in Fig. 4.16 and confirm that minima in the domain average latent heating rate correspond with minima in buoyancy production in the 0730 and 0815 cases as well as the 0812-HI simulation (see Fig. 4.14), with stronger evaporative cooling in the 0730 and 0815 LO simulations. However, this is not true of 0812-LO, which has no single well-defined minimum in evaporative cooling. The much stronger minimum in buoyancy production cannot be related to the instantaneous evaporation rate in this case.

*Stevens et al.* [1998] propose that asymmetries in saturation height between updrafts and downdrafts can explain the vertical structure of buoyancy production in a drizzling

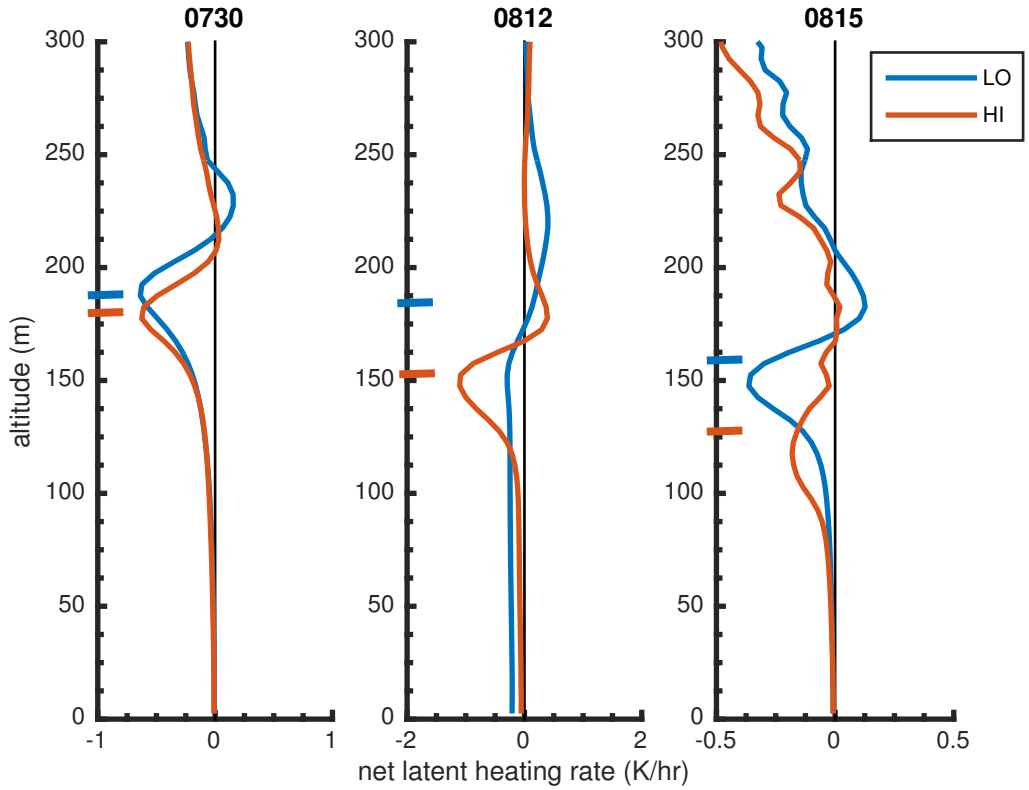



Figure 4.16: Profiles of net latent heating rate. Cloud base for each simulation is denoted by hash marks on the abscissa and defined as the lowest level with $\overline{q_l} > 0.01$ g kg$^{-1}$.

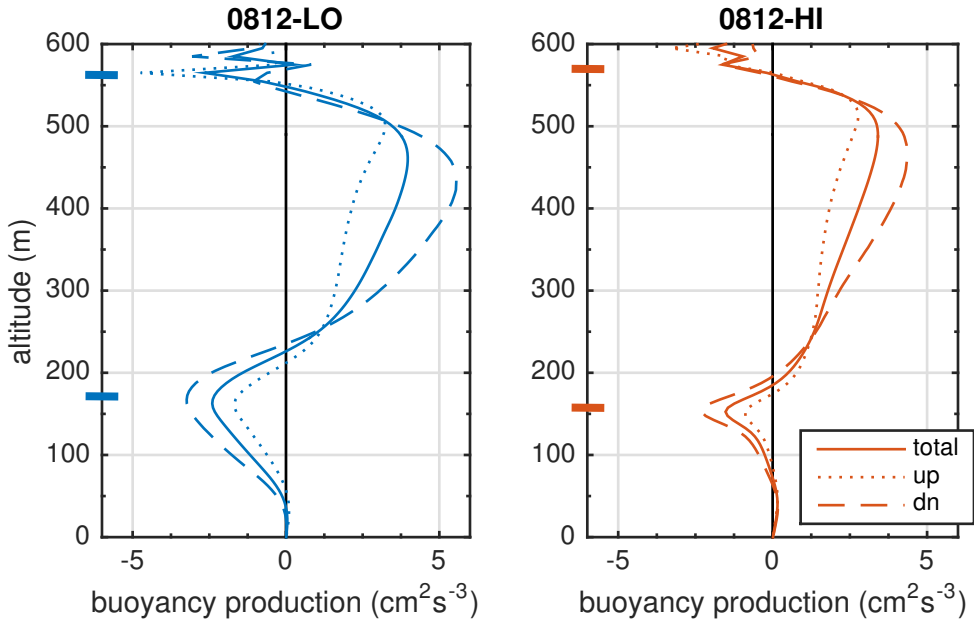



Figure 4.17: Partitioning of buoyancy production by $w'$, 0812 case. Cloud base and top are denoted by hashmarks on abscissa.

STBL. They argue that precipitation formation causes condensational heating at cloud top which is offset although not exceeded by radiative cooling. Thus, descending downdrafts are warmer than updrafts and reach saturation at a higher level than updrafts. As a consequence, evaporation begins to occur in downdrafts above the mean cloud base and downdrafts quickly become buoyant compared to their surroundings, i.e. buoyancy is consumed. This idea can be tested by partitioning buoyancy production into contributions from up- and downdrafts, shown in Fig. 4.17. Our results appear to agree with the *Stevens et al.* [1998] argument within 100 m of cloud base, but their reliance on warmer downdrafts is not consistent with greater positive buoyancy production in downdrafts than updrafts above $z = 250$ m. A more detailed description of the effect of sedimenting drops on buoyancy production is clearly needed, but will be left for a future study.

To summarize our findings with respect to turbulence, we find that increased spectral resolution amplifies turbulence relative to mass doubling resolution simulations in the

precipitating 0812 case while dampening it in the non-precipitating 0815 case. Little change is observed in the 0730 case. It is notable that the 0812-HI simulation can no longer be considered precipitating, as this appears to be the key in explaining the opposite responses to changing resolution in the 0812 and 0815 cases. In the presence of a weakly sedimenting cloud layer such as occurs in 0815-LO, on the other hand, increased buoyancy production at cloud top is not overcome by increased buoyancy consumption at cloud base and the entire boundary layer is more turbulent as a result.

## 4.5 Summary

For the last thirty years, dynamical models with explicit microphysical schemes have nearly exclusively utilized mass doubling spectral resolution. In the nascent period of numerical modeling of the atmosphere during which many microphysical schemes were first implemented, increased spatial resolution and expanded process representation were understandably of higher priority. The added computational expense of representing a finer drop size grid is admittedly substantial, with a quadrupling of spectral resolution requiring about a factor of six more time per time step in our model.

In the context of this study, the question of spectral resolution originally arose because of the desire to compare *in situ* observations of cloud drops with model output as opposed to the reasons of theoretical interest and numerical accuracy that drove many of the early attempts to discretize cloud microphysical processes [*Bleck*, 1970; *Berry and Reinhardt*, 1974; *Tzivion et al.*, 1987]. As such, it is important to validate that changing spectral resolution does not undesirably alter simulation results.

We have presented output of large eddy simulations with bin microphysics at the "standard" mass doubling resolution and high resolution with a logarithmic bin spacing factor of $2^{1/4}$. Boundary conditions for the case studies are based on observations of marine stratocumulus off the coast of California. The selection of cases encompasses a range of boundary layer depth, inversion strength, time of day, and aerosol loading. We find that only one of the three cases (0730) shows close agreement across spectral

resolution. The agreement in this case is likely due to a combination of low CCN concentration and a thin saturated layer such that collision-coalescence is of relatively minor importance. In the other two cases (0812 and 0815), major differences are noted in the drop size distribution such that many fewer large drops ($D > 100\,\mu m$) are present in the high resolution simulations. These differences are initially due to artifical acceleration of collision-coalescence at standard mass doubling resolution, but result in significant, self-reinforcing changes in boundary layer dynamics over the course of the simulations. Furthermore, the character of the dynamical differences between the 0812 and 0815 simulations are in opposition: in the 0812 case, the high resolution simulation is unable to form precipitation, resulting in a more turbulent boundary layer while in the 0815 case, the high resolution case produces less turbulence because of decreased buoyancy production near cloud top, even though it attains a higher maximum rain rate than the high resolution simulation near cloud top. Such dynamical changes reinforce the divergence in DSD outcomes between high and low resolution simulations.

Does the use of higher spectral resolution add value to model results in proportion to the computational expense? The answer to this question depends on the research question to be pursued. In the case of the present work, the answer is an emphatic "yes," as the goal of our research program is to evaluate the onset of collision-coalescence, a process to which there appears to be considerable sensitivity to spectral resolution. The ability of a refinement in spectral resolution to suppress precipitation with no other changes in boundary conditions or process representation suggests that microphysics with mass doubling bins may be getting the "right" answer for the wrong reasons.

# Chapter 5

# Can turbulent collision-coalescence improve the representation of drop size spectra in simulations of marine stratocumulus?

## 5.1 Introduction

Parameterization of the microphysical processes responsible for precipitation formation are necessary in all numerical models of the atmosphere that are capable of producing realistic atmospheric flow conditions because of the wide range of spatial scales that must be represented [*Franklin*, 2014]. The convective circulations that drive cloud and precipitation formation in the planetary boundary layer (PBL) occur at the vertical scale of the PBL – from hundreds of meters to about a kilometer – while the microphysical processes that govern the evolution of cloud drops occur on scales as small as micrometers, the size of the drops themselves. Despite the necessity for microphysical parameterizations, there remain major unresolved questions regarding the representation of the relevant processes such that clouds and their interaction with other

components of the climate system are the leading source of uncertainty in projections of future climate [*IPCC*, 2013].

One topic that has received considerable attention over the years is the initiation of precipitation in the absence of ice. Collision-coalescence is the process responsible for growing drops from the small sizes attainable by condensation (drop diameter $D$ ~10-30 μm) to the size of rain drops observed at the surface ($D > 1$ mm) on time scales commensurate with a single overturning of the PBL (15-20 minutes). A typical cloud drop 20 μm in diameter must undergo over $10^5$ collisions to become a 1 mm raindrop in that time period. Many mechanisms have been proposed to explain how collision-coalescence may be accelerated (or to some extent circumvented) such as the existence of giant cloud condensation nuclei [*Johnson*, 1982], introduction of heterogeneity by turbulent mixing [*Baker and Latham*, 1979], and direct augmentation of collision-coalescence rates by turbulence [*Wang and Grabowski*, 2009]. While all of these likely play a role, the focus of this study is on turbulent enhancement of collision-coalescence.

Several parameterizations of turbulent collision-coalescence rates have been developed for use in dynamical models [*Ayala et al.*, 2008b; *Franklin*, 2008; *Benmoshe et al.*, 2012] and application of these parameterizations has confirmed that turbulence can increase surface accumulation of precipitation in shallow cumulus [*Seifert et al.*, 2010; *Wyszogrodzki et al.*, 2013; *Franklin*, 2014]. Less attention has been given to developing a systematic description of how turbulent collision-coalescence modifies the drop size distribution (DSD) and aids or suppresses production of the first embryonic drizzle drops. This study seeks to apply the turbulent kernel of *Ayala et al.* [2008b] in observationally-constrained large eddy simulations (LES) of marine stratocumulus off the coast of California to evaluate whether turbulent collision-coalescence improves the representation of the DSD relative to *in situ* aircraft observations. The simulations also employ a newly-implemented high spectral resolution bin microphysics scheme to assess whether standard mass-doubling microphysics spectral resolution is sufficient to directly compare model output of the DSD with *in situ* observations of the DSD in the size regime relevant to precipitation formation ($20 \lesssim D \lesssim 100\,\mu$m).

## 5.2 Model description

For our simulations, we use RAMS version 4.3.0 in LES mode. The model is configured as described in Chapter 4.2, with two changes to the bin microphysics scheme: (1) the turbulent collision kernel of *Ayala et al.* [2008b, hereafter referred to as the Ayala kernel] is implemented and (2) the approximative condensation/evaporation scheme of *Stevens et al.* [1996a] is used.

The Ayala kernel extends the quiescent hydrodynamical kernel of *Hall* [1980] to account for the effects of microscale turbulence on collision efficiency and the geometric collection kernel. Turbulent enhancement of the kernel is parameterized as a function of the turbulent dissipation rate $\epsilon$ (i.e. $K_{Ayala}(m_1, m_2, \epsilon)$), which is calculated as in *Wyszogrodzki et al.* [2013]:

$$\epsilon = C_\epsilon (TKE)^{3/2} / \Delta \tag{5.1}$$

where $C_\epsilon = 0.845$, turbulent kinetic energy (TKE) is calculated from resolved scale velocity perturbations, and $\Delta = (\Delta x + \Delta y + \Delta z)/3$ is the arithmetic mean of the model grid spacings. The Ayala kernel is explicitly defined from direct numerical simulations at $\epsilon = \{100, 400\}\,\mathrm{cm^2 s^{-3}}$ [*Ayala et al.*, 2008a] and linearly interpolated to other values of $\epsilon$ for use in LES.

Kernel coefficients for use in the collision-coalescence subroutine are calculated offline and stored in a lookup table. To avoid repeated interpolation over $\epsilon$ during runtime, Ayala kernel coefficients are generated at discrete values of dissipation rate relevant to shallow convection, $\epsilon = \{0, 10, 30, 50, 100, 300, 400, 600\}\,\mathrm{cm^2 s^{-3}}$. The kernel value in a grid cell is then selected by rounding up $\epsilon$ (e.g. $K(\epsilon = 15) = K(\epsilon = 30)$), with the proviso that that $K(\epsilon < 1) = K(0)$ since $\epsilon$ is always greater than 0 in cloud. It should be noted that the Ayala kernel reduces to the Hall kernel at $\epsilon = 0$. While the "round up" approach leads to artificial acceleration of collision-coalescence rates because the Ayala kernel is a monotonically increasing function of $\epsilon$, uncertainty resulting from the linear interpolation dominates at the low dissipation rates prevalent in

marine stratocumulus (where typical $\overline{\epsilon} \lesssim 10\,\mathrm{cm^2 s^{-3}}$, *Siebert et al.*, 2010) . This study is not the first to implement the Ayala kernel in a dynamical model, although it is the first to focus on stratocumulus; other studies have implemented it for use with both bin and bulk microphysics schemes to simulate cumulus [e.g. *Wyszogrodzki et al.*, 2013; *Seifert et al.*, 2010, respectively].

The model can be configured to use the high spectral resolution bin microphysics scheme described in Chapter 4 with logarithmic grid spacing factor $p = 2^{1/4}$. In Chapter 4, the analytical condensation and evaporation scheme of *Tzivion et al.* [1989] was used. Violation of conservation of mass occurred during high resolution simulations with the turbulent kernel and the approximative "top hat" condensation/evaporation scheme of *Stevens et al.* [1996a] was therefore used to generate all the results presented here. The general approach of each scheme is similar: bin boundaries are moved according to the vapor forcing and drop number and mass (zeroth and first moments of the DSD) are remapped accordingly. The *Stevens et al.* [1996a] method assumes a constant mass distribution within a bin (thus the "top hat" descriptor, originally from *Egan and Mahoney*, 1972) instead of allowing the number and mass concentration to evolve independently as in the analytical method. The "top hat" approximation causes slightly more net condensation than the analytical method, causing liquid water path to be somewhat higher ($\Delta LWP/LWP < 10\%$). This margin of error does not affect the conclusions of the study.

Four simulations are performed for each case study: standard mass-doubling spectral resolution with the quiescent collision kernel (default "control" configuration, LO-CTRL); standard resolution with the turbulent kernel (LO-TURB); high spectral resolution with the quiescent kernel (HI-CTRL); and high spectral resolution with the turbulent kernel (HI-TURB). All simulations are run for 6 hours and the results presented are averaged over the horizontal domain during the final hour of each simulation. The quiescent Hall kernel is used during the first 2 hours of simulation time at which point simulations branch into CTRL and TURB variants. This is done to avoid spuriously large collision-coalescence rates during model spinup, when the turbulent dissipation

rate upon which the turbulent collision kernel depends fluctuates widely. In all figures where results from simulations are presented, blue represents LO resolution simulations and red represents HI resolution simulations (as in Chapter 4). The line style indicates the collision kernel, with CTRL represented by a solid line and TURB by a dashed line. Where it appears that only a solid line exists for a given resolution, there is no noticeable difference between CTRL and TURB simulations. Vertical profiles of the observations binned in 10 m altitude increments are plotted in black for those variables for which observations exist.

## 5.3 Observations and case studies

Observational data are derived from research flights during the Physics of Stratocumulus Tops (POST) campaign, which took place during July and August 2008 off the coast of Monterey, California. Research flights were flown by the Center for Interdisciplinary Remotely Piloted Aircraft Studies Twin Otter which was instrumented with standard thermodynamic, dynamic and microphysics probes. Details of the instrumentation are available in *Carman et al.* [2012] and *Gerber et al.* [2013].

Of primary relevance to this study are the microphysics probes. Cloud drops of diameter 2-150 μm are sampled by an Artium Phase Doppler Interferometer [PDI, *Chuang et al.*, 2008] and drizzle drops of diameter $25-1550\,\mu m$ are sampled by a Droplet Measurement Technologies Cloud Imaging Probe [CIP, *Baumgardner and Korolev*, 1997; *Korolev*, 2007]. The sampling range of the PDI and CIP overlap, so construction of a merged DSD from the full size range sampled ($2-1550\,\mu m$) for comparison with model output involves selection of a crossover size between instruments. Ideally, the full sampling range of one instrument could be used, but the CIP has known sizing issues for drops smaller than $100\,\mu m$ [*Strapp et al.*, 2001] hence it is desirable to minimize use of CIP bins smaller than $100\,\mu m$. While the PDI has no such sizing issues, its small sampling volume results in degradation of population statistics for drops significantly larger than $\sim$ 80 μm in the relatively clean conditions observed during POST, with a

narrower usable range in more pristine conditions (i.e. lower total concentration reduces the probability of sampling particularly large or small drops). The crossover diameter is chosen to be 65 μm, such that there is 1 μm of overlap between the two instruments (PDI bin 97 sampling diameter 63 – 66 μm, and CIP bin 3 sampling 64 – 89 μm). While this forces the use of two CIP bins sampling drops of $D < 100\,\mu m$, a continuous merged DSD is preferable.

All observed DSD rain rates and percentile diameters presented herein are calculated from flight mean merged DSDs and percentile diameters are calculated only for drops of size $D > 10\,\mu m$ because model-derived DSDs have anomalously high concentration at smaller sizes. Profiles of liquid water content (LWC) and drop concentration $N_D$ were calculated from only the PDI [*Carman et al.*, 2012] for two reasons: (1) cloud base height is estimated using LWC and $N_D$ should not take into account contributions to liquid water from drizzle drops (in this case simply and somewhat coarsely defined as drops in the CIP range) and (2) some concerns exist regarding the post-processing of the CIP observations during POST. The default output of the CIP tends to overcount drops at all size ranges because of lax image rejection criteria, leading to unrealistically high concentrations.

Flights during POST focused on the cloud top region and the inversion layer above it. This focus on a thin layer of the atmosphere resulted in limited sampling of the surface mixed layer, cloud base and the free troposphere. As such, several of the free tropospheric soundings are based on only 2-4 aircraft traverses. Initial soundings are constructed from idealized linear piecewise fits to the observations but are significantly simplified above the boundary layer to reflect low confidence in the ability of a few data points to represent the mean state of the atmosphere.

Selection of case studies is described in detail in Chapter 4.3. The criteria for case selection were a well-developed cloud layer, minimal change in boundary layer height over the observational period and minimal shear. The three cases selected are 2008-07-30 (TO7, day flight), 2008-08-12 (TO14, evening/night flight) and 2008-08-15 (TO17, day flight). These cases will be referred to by 4-digit month and date for the remainder

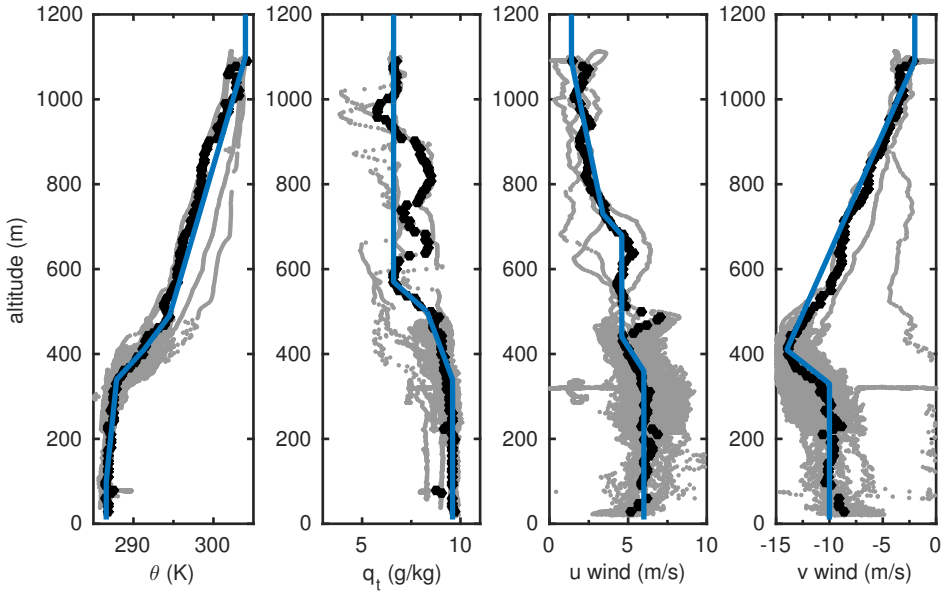



Figure 5.1: Thermodynamic soundings for the 0730 case. Profiles from left to right: a) potential temperature $\theta$, b) total water mixing ratio $q_t$, c) $u$ wind component (west-east), d) $v$ wind component (north-south). Gray dots are all observations, black filled circles are 10 m binned median observations and blue solid lines are initial model soundings.

of the chapter, i.e. 0730, 0812 and 0815, respectively. Table 4.2 gives the boundary conditions used in each simulation. The observational context of each case study will be explored individually in the remainder of this section.

### 5.3.1 Case 1: 0730

The 0730 case (Fig. 5.1) was a daytime flight through the thinnest cloud layer of the three case studies ($\overline{z_{CT}} - \overline{z_{CB}} = 282\,\text{m}$) that was characterized by a weak inversion in both temperature and moisture ($\Delta T = 2.9\,\text{K}$, $\Delta q_t = -0.27\,\text{g kg}^{-1}$). The moisture content of the free troposphere was quite variable in this case. In the interest of simplicity, the vertical structure betwen 600 and 1000 m was ignored, as well as the kink in the $u$ wind component at the top of the inversion layer. Total drop concentration $N_D$ is the lowest of the three cases, reaching a maximum between 35 and 40 $\text{cm}^{-3}$. Despite the relatively

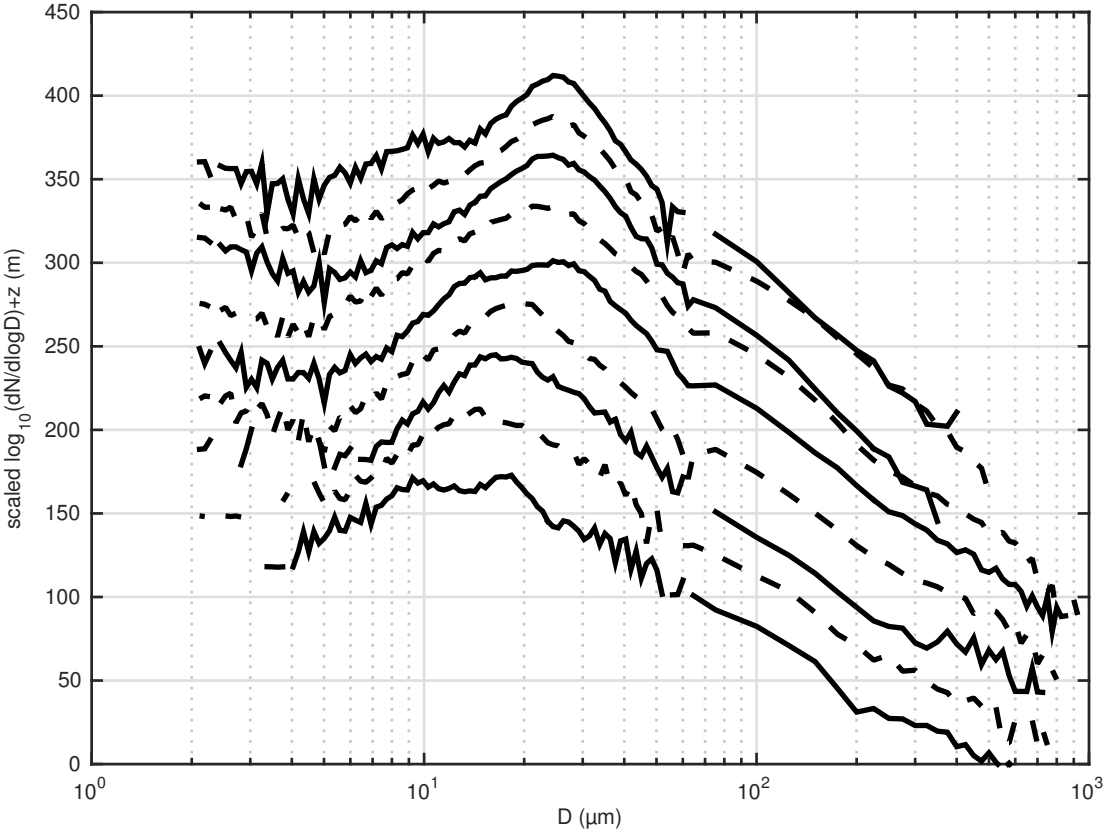



Figure 5.2: Profile of the merged DSD as a function of altitude, 0730 case. Alternating solid and dashed lines for visual clarity. Lowest level plotted is $z = 150\,\mathrm{m}$ and the highest level plotted is $z = 300\,\mathrm{m}$.

thin cloud layer, light drizzle was observed below cloud base due to low concentration (mean cloud base rain rate $R_{CB} \approx 0.15\,\mathrm{mm\,d^{-1}}$).

The weak, moist inversion present during the 0730 research flight makes for a somewhat complicated microphysical picture. Merged DSDs as a function of altitude at 30 m intervals and conditioned on $\overline{LWC(z)} > 0.05\,\mathrm{g\,m^{-3}}$ are shown in Fig. 5.2. Despite the cloud being less than 300 m thick, a clear drizzle mode can be seen with drops of up to nearly a millimeter in size observed in the lower half of the cloud. There is also evidence of secondary activation of CCN at cloud top as indicated by the relatively high concentration of small drops ($D < 10\,\mu\mathrm{m}$), likely because of the weak thermal contrast at cloud top and high moisture content of entrained air. Low total drop concentration

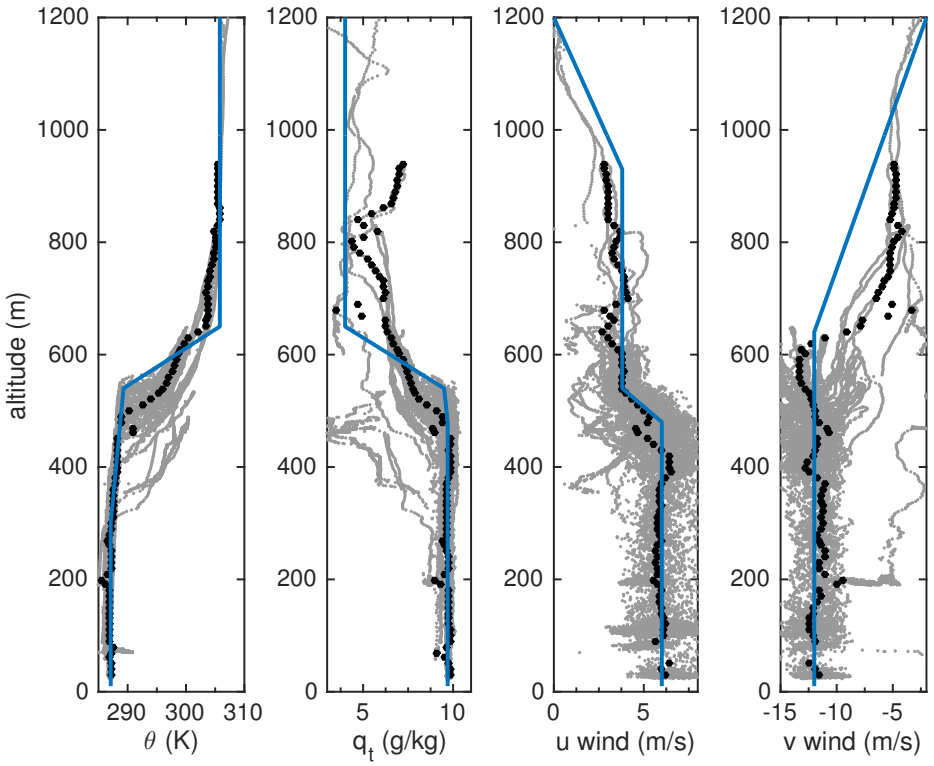



Figure 5.3: Thermodynamic soundings for the 0812 case. Profiles from left to right: a) potential temperature $\theta$, b) total water mixing ratio $q_t$, c) $u$ wind component (west-east), d) $v$ wind component (north-south). Gray dots are all observations, black filled circles are 10 m binned median observations and blue solid lines are initial model soundings.

is responsible for the discontinuity of the DSD near the PDI-CIP crossover diameter ($D = 65\,\mu\text{m}$).

### 5.3.2 Case 2: 0812

The 0812 case (Fig. 5.3) is an example of a more "classical" nocturnal marine stratocumulus setting with a moderately strong inversion capping the boundary layer ($\Delta T = 6.4\,\text{K}$, $\Delta q_t = -1.47\,\text{g}\,\text{kg}^{-1}$). The choice to start the inversion above the median of the observations was made because of the constant v wind sounding. Over the course

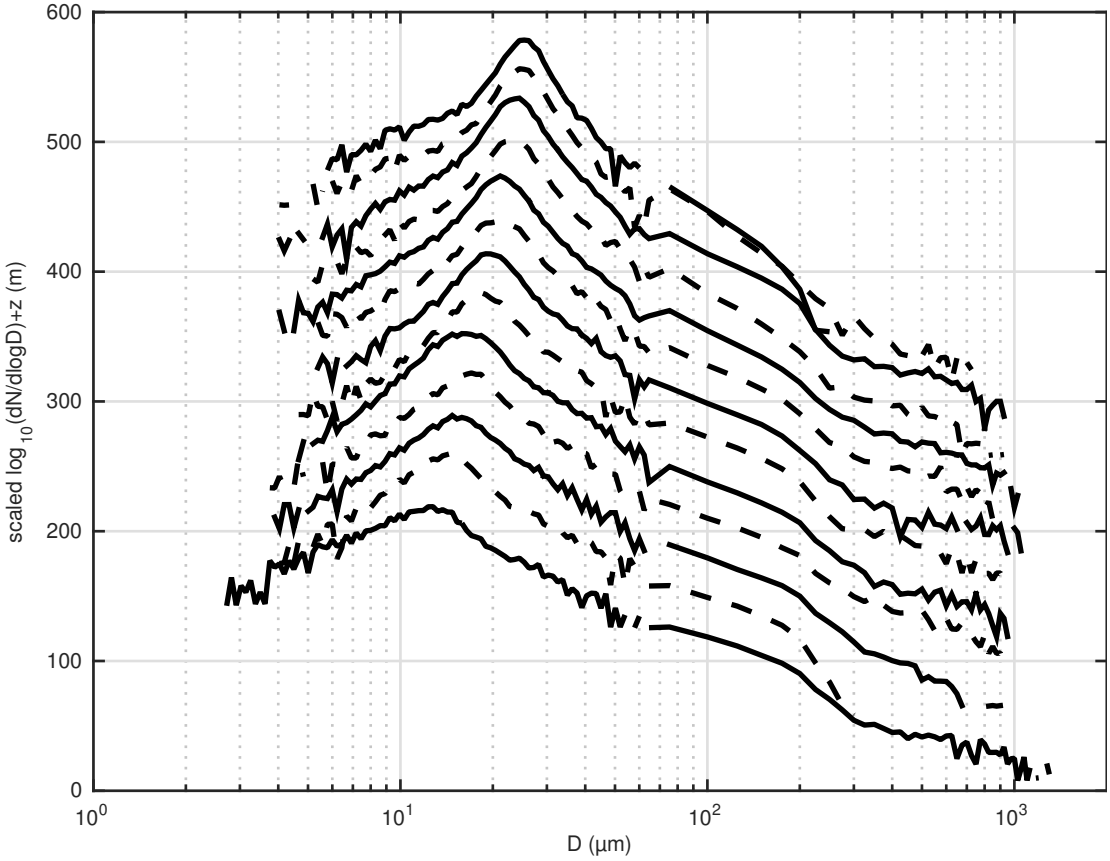



Figure 5.4: Profile of the merged DSD as a function of altitude, 0812 case. Alternating solid and dashed lines for visual clarity. Lowest level plotted is $z = 180\,\mathrm{m}$ and the highest level plotted is $z = 480\,\mathrm{m}$.

of the simulations, the u component of wind adjusts to match the free tropospheric value of $\sim 4\,\mathrm{m\,s^{-1}}$ such that negligible shear is generated. While one might expect that raising the inversion height by nearly 50 m would bias the simulations toward producing too much liquid water, it will be seen that this is not the case. This case is the most heavily precipitating, with mean $R_{CB} = 0.5\,\mathrm{mm\,d^{-1}}$ and cloud layer $N_D \approx 100\,\mathrm{cm^{-3}}$.

The profile of the merged DSD is presented in Fig. 5.4. Compared with the 0730 case (Fig. 5.1), two major contrasts can be made: the growth of the mode size with altitude due to condensation is much clearer and the drizzle mode is more pronounced in this case with drops of size $D \approx 1\,\mathrm{mm}$ forming by 60 m below cloud top. The DSD

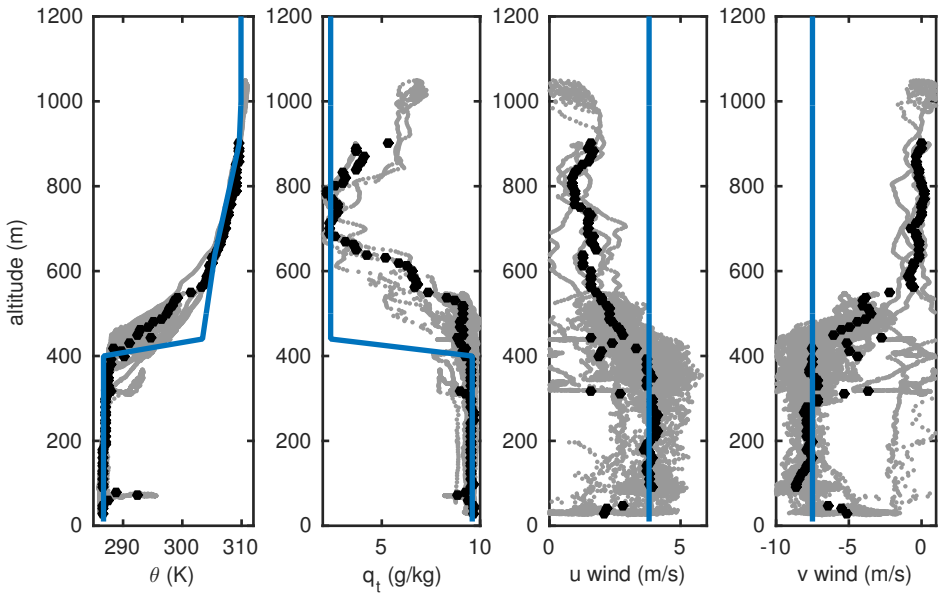



Figure 5.5: Thermodynamic soundings for the 0815 case. Profiles from left to right: a) potential temperature $\theta$, b) total water mixing ratio $q_t$, c) $u$ wind component (west-east), d) $v$ wind component (north-south). Gray dots are all observations, black filled circles are 10 m binned median observations and blue solid lines are initial model soundings.

is also somewhat more continuous across the instrument crossover owing to greater $N_D$ and a larger mode size. The apparent lack of drizzle drops 30 m above cloud base is probably due to a combination of poor sampling at that altitude and spatial variability in precipitation.

### 5.3.3 Case 3: 0815

The 0815 case is one of the more complex of the POST cases, with differential advection of a continental origin apparent in the inversion layer that caused this case to have a well-defined thermal inversion but a positive moisture jump with increasing altitude ($\Delta T = 6.8\,\mathrm{K}$; $\Delta q_t = +0.21\,\mathrm{g\,kg^{-1}}$). The profiles of horizontal wind were set to be constant throughout the depth of the model domain because changes in wind direction through the inversion do not generate appreciable shear. In addition to serving

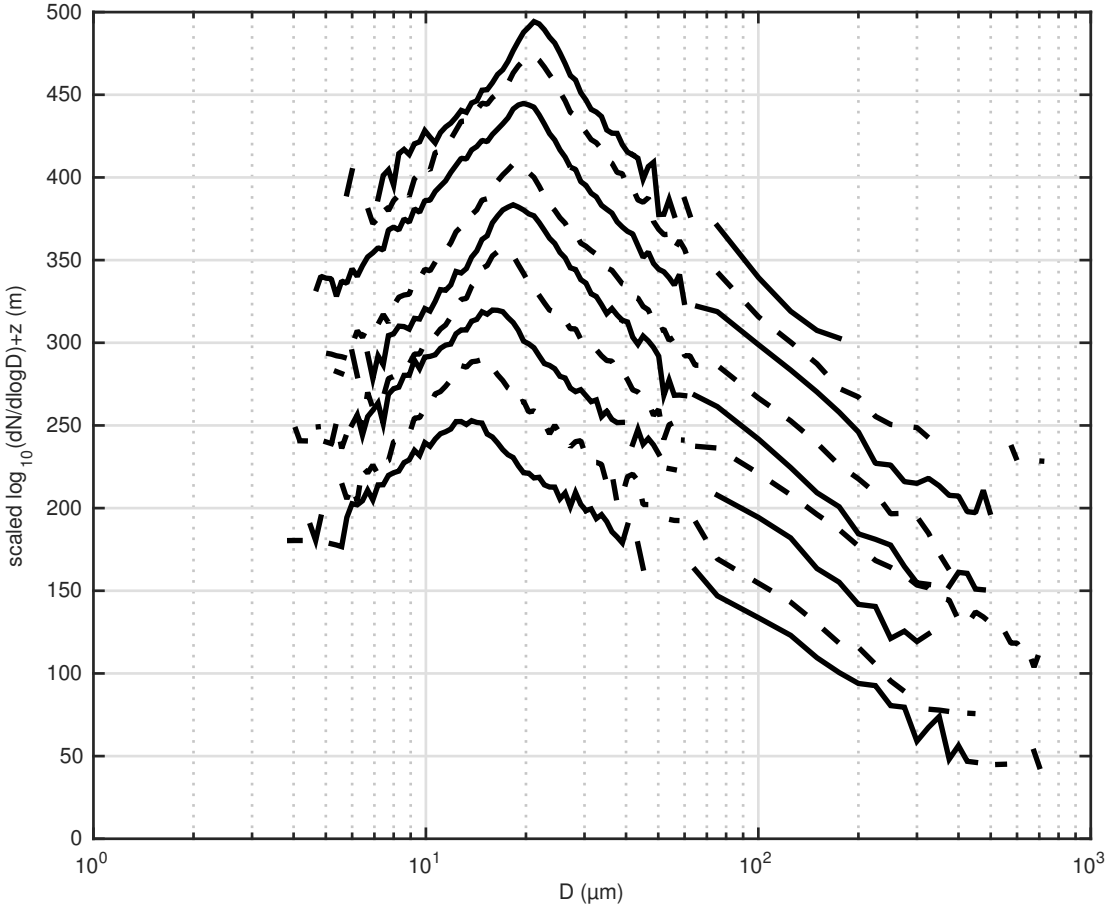



Figure 5.6: Profile of the merged DSD as a function of altitude, 0815 case. Alternating solid and dashed lines for visual clarity. Lowest level plotted is $z = 180$ m and the highest level plotted is $z = 390$ m.

as a source of free tropospheric moisture, the contintentally-sourced air mass above cloud top also contained high aerosol concentrations that appeared to be impinging on the cloud layer. Cloud drop concentration was a reasonable 100 $\mathrm{cm}^{-3}$ through much of the cloud layer but much higher values exceeding 200 $\mathrm{cm}^{-3}$ were observed near cloud top, some of the highest concentrations seen during POST. Although $R_{CB}$ was negligible during this flight, isolated values in excess of 1 $\mathrm{mm\,d}^{-1}$ were observed.

The profile of the merged DSD is given in Fig. 5.6 and for this case shows a clearly non-precipitating cloud layer, at least in the mean. Limited numbers of larger drops

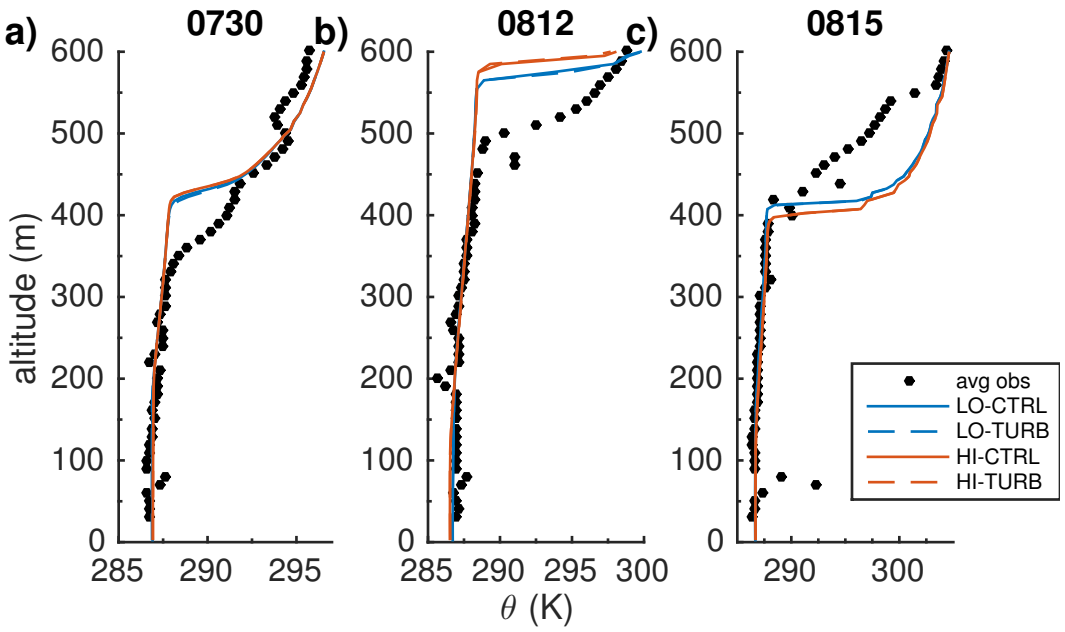



Figure 5.7: Profiles of potential temperature $\theta$

are observed, but drops of the cloud base mode size ($D \approx 15\,\mu$m) are separated by $\sim 8$ orders of magnitude in concentration from the largest drops observed at the same level ($D \approx 300\,\mu$m). Curiously, there is no evidence for secondary activation near cloud top despite the haze layer overlying the cloud. The strong thermal inversion appears to be limiting transport of particulate matter into the cloud layer via entrainment.

## 5.4 Model results and validation against observations

Profiles of basic thermodynamic quantities will be presented to show that model output is roughly comparable with the observations. Some differences between LO and HI resolution simulations are to be expected based on the results of Chapter 4. Overall, profiles of $\theta$ (Fig. 5.7) are in good agreement between simulations of the same microphysical resolution but illustrate a well-known problem in LES of stratocumulus, over-entrainment at cloud top, which causes the boundary layer to grow more quickly

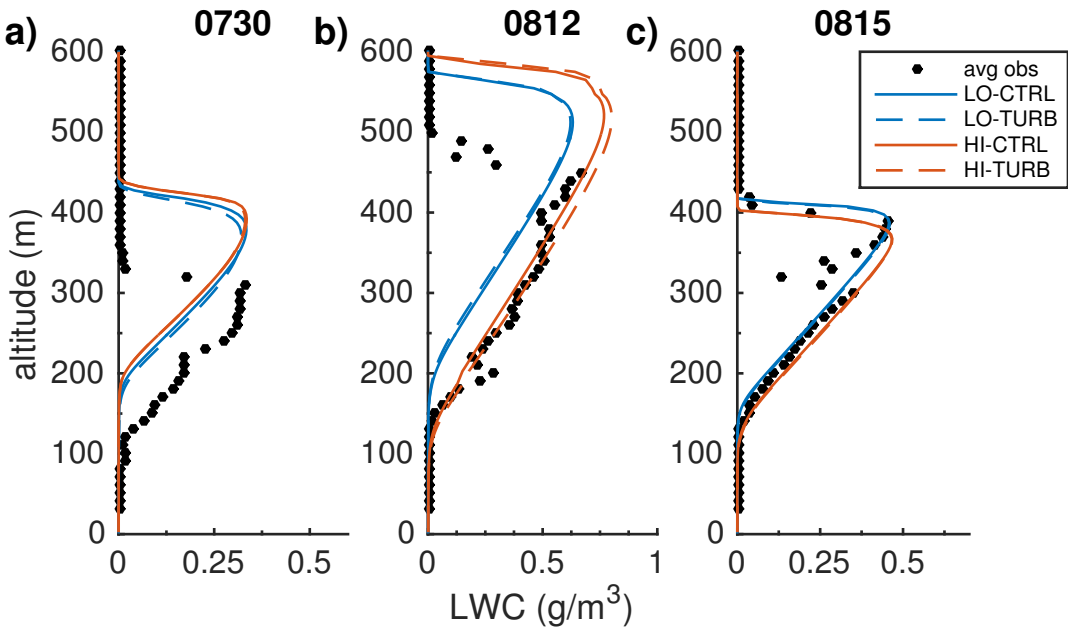



Figure 5.8: Profiles of liquid water content LWC

than observed. This issue is particularly prominent in RAMS [*Stevens et al.*, 2005] and is most obvious in the 0730 case (compare Fig. 5.7a with Fig. 5.1a), where the inversion has lifted by almost 50 m and sharpened considerably over the course of the simulations. Use of the turbulent kernel has very little effect on the thermal structure of the simulations, causing a slightly higher inversion height in the 0730 and 0812 LO-CTRL experiments relative to LO-TURB but no other differences of note.

The effect of the turbulent kernel is also subtle in profiles of LWC in Fig. 5.8. Greater differences are apparent in profiles of rain rate $R$ that help explain the minor discrepancies in LWC (Fig. 5.9). Descending from cloud top in the 0730-LO simulations, $R$ becomes greater in the TURB configuration; a greater rate of near-cloud top LWC removal by sedimentation explains the slightly lower 0730-LO-TURB LWC maximum in both magnitude and altitude (Fig. 5.8a). Rain rate in 0730-LO-TURB remains greater than the CTRL simulation throughout the boundary layer. A similar narrative applies to the 0812-LO simulations, although the separation between TURB and CTRL simulations is

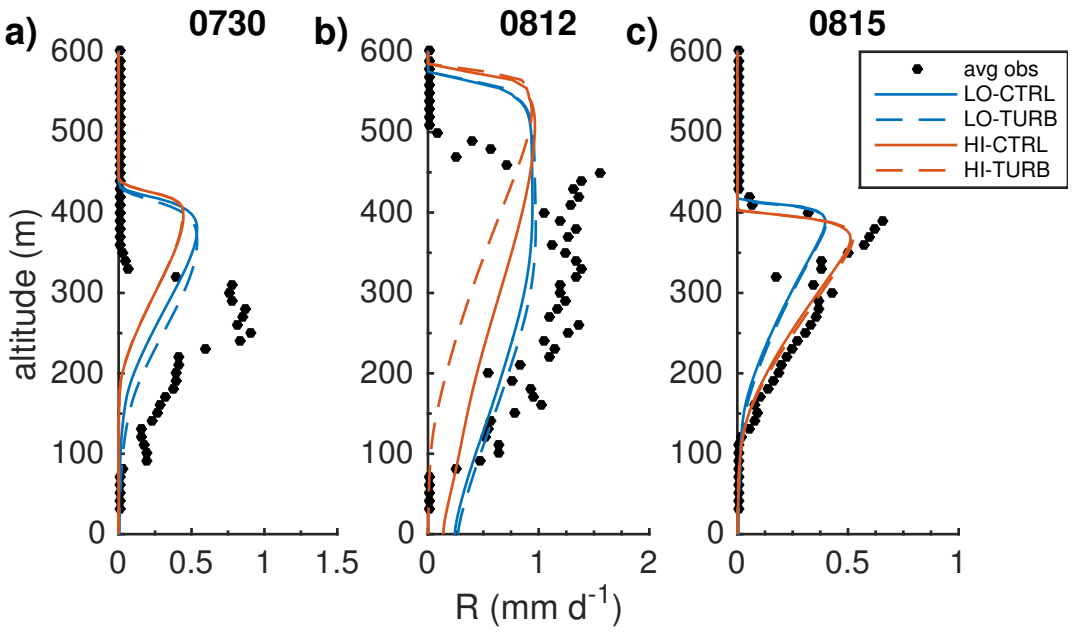



Figure 5.9: Profiles of rain rate $R$

smaller. The most substantial modification of rain rate due to the turbulent kernel is seen in the 0812-HI simulations, where precipitation is effectively suppressed by the TURB configuration, the opposite response as in the LO simulations. In addition, 0812-HI-TURB LWC is the greatest of all the 0812 simulations – at least in part due to decreased $R$. Further discussion of this seemingly contradictory response to the turbulent kernel is deferred until the end of the section. Very minor differences are seen in the 0815 case simulations though it is notable that 0815 is the only case for which the HI simulations more closely match the observations than the LO configuration, with greater values of $R$ through the entire depth of the cloud layer and the greatest values obtained by the 0815-HI-TURB solution.

The microphysical differences between CTRL and TURB simulations that determine differences in quantities such as $R$ depend on the turbulent dissipation rate $\epsilon$, profiles of which are shown in Fig. 5.10. Unsurprisingly, the magnitude of domain mean $\epsilon$ is rather unimpressive; stratocumulus is known to be the least turbulent convective cloud

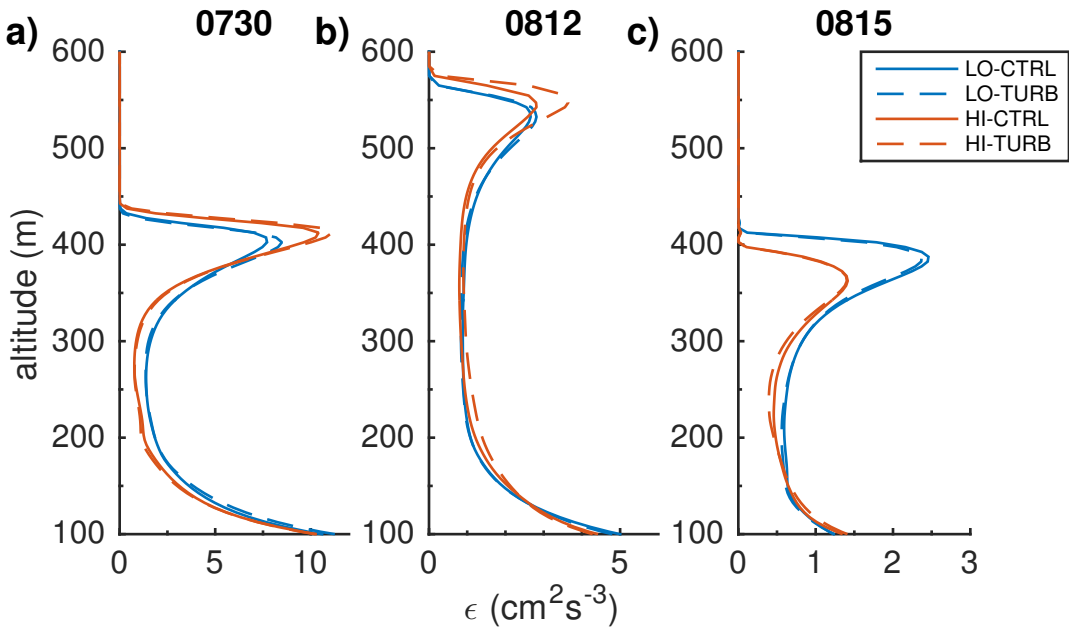



Figure 5.10: Profiles of TKE dissipation rate $\epsilon$

type [cf. *Siebert et al.*, 2010; *Devenish et al.*, 2012]. Yet despite such low magnitude, these simulations show that feedbacks on the vertical structure of $\epsilon$ can occur as a result of coupling turbulence to collision-coalescence. In the 0730-LO-TURB simulation, increased collision rates lead to an increased cloud top sedimentation flux, which then causes an increase in spatially-averaged turbulence intensity as evidenced by higher cloud top $\epsilon$ in 0730-LO-TURB than 0730-LO-CTRL (Fig. 5.10a). This increase in TKE is somewhat surprising, as more intense drizzle formation should lead to greater condensational and sedimentation heating rates, which in turn should have a stratifying influence on cloud top. Increased sedimentation apparently causes enough of a decrease in entrainment rate [*Ackerman et al.*, 2004; *Bretherton et al.*, 2007] to offset what would otherwise be expected to be an increase in entrainment from increasing TKE at cloud top. This is confirmed by the constant cloud top heights among simulations at the same spectral resolution.

Before examining the DSD, profiles of total drop concentration $N_D$ give context to

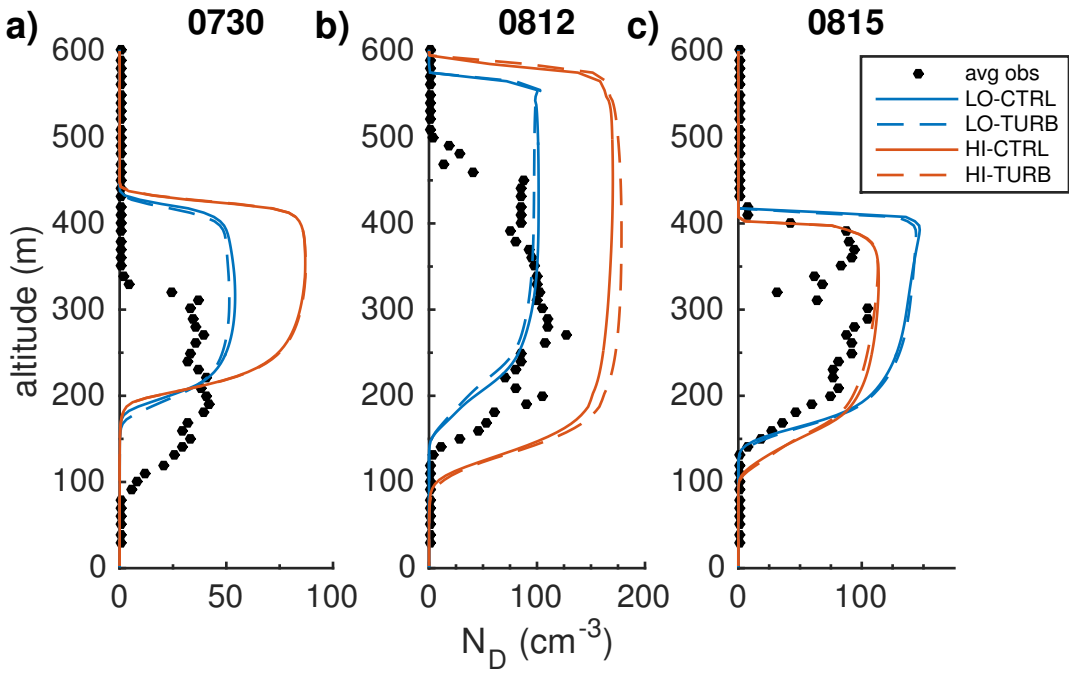



Figure 5.11: Profile of total drop concentration $N_D$

the remainder of the investigation (Fig. 5.11). Here an unintended consequence of the choice of spectral resolution is revealed: in the two drizzling cases (0730 and 0812) the HI simulations have much greater total concentration. All else being equal, it is more difficult to generate precipitation in the presence of higher drop concentrations [*Xue and Feingold*, 2006b; *Stevens. and Feingold*, 2009], especially in the framework of the model used in this study, where CCN concentration is held constant and cannot be reduced by collisonal scavenging. This contrast in $N_D$ alone may explain much of the difference in $R$ across resolution in the 0730 and 0812 cases (Fig. 5.9), where precipitation is effectively suppressed in the 0812-HI-TURB and both 0730-HI simulations. It is unclear why the same trend does not hold in the 0815 case; the reasons for this will be explored in future work.

The turbulent kernel has subtle but observable impacts on the macrophysical evolution of the simulations. Its effect is seen most clearly in low resolution simulations that

are already conducive to drizzle formation (i.e. the 0730 and 0812 LO simulations), while the response in HI simulations is muted or seemingly in opposition to the response of the LO simulations, as in the 0812-HI-TURB simulation where drizzle is suppressed. This is in great part due to increased $N_D$. Next we will examine the size-resolved microphysical response to the turbulent kernel to better understand the varied response of the simulations.

## 5.5 Comparison of LES microphysics output with observations

The sedimentation flux (equivalent to rain rate if converted to units of length per time) is a strong function of drop size, given in discrete form by

$$R = \sum_{k=1}^{K} m(k)N(k)v_T(k) \tag{5.2}$$

where $m(k)$ is the average mass of a drop in bin $k$ assuming spherical geometry, $N(k)$ is the concentration in bin $k$, $v_T(k)$ is the Stokes terminal velocity of the average mass drop in bin $k$ and $K$ is the total number of bins. In the drop size range considered here ($D < 1$ mm), $v_T(k)$ can be approximated as $v_T(k) \approx \alpha D(k)^\beta$ where $\alpha$ and $\beta$ depend on drop size such that the differential contribution to $R$ can be expressed

$$\frac{dR(k)}{dlog_{10}D} = \frac{\pi}{6}\frac{dN(k)}{dlog_{10}D}\begin{cases}\alpha D(k)^5 & D < 80\,\mu\text{m} \\ \alpha D(k)^4 & D \geq 80\,\mu\text{m}\end{cases}. \tag{5.3}$$

It is clear from Equation 5.3 that the sedimentation flux is quickly dominated by the production of large drops because of the dependence on higher-order moments of the DSD. The conclusion can be drawn from Fig. 5.9 that the production of the large drops that drive the total sedimentation flux must be accomplished in the top $\sim$ 50 m of cloud as the rain rate just below cloud top is never exceeded lower in the boundary layer (at least in the mean). Therefore, it is reasonable to assume that if the DSD near cloud top

can be closely approximated by the model microphysics scheme, then good agreement with observations of cloud base rain rate or surface accumulation rate (if applicable) should follow. A "close approximation" of the DSD in this context means accurately reproducing the right tail of the DSD in LES.

One useful metric for visually examining the tail of the DSD is percentile diameter, which collapses the DSD from a sized-resolved function of at least many tens of categories to a single value based on the percentile of interest. For example, the 50th percentile (notated $d_{50}$) describes the median diameter of the DSD and contains information about the maximum size drops can reach by condensation. The percentile diameter metric allows for a visually simplified analysis of systematic variation in the DSD with altitude, yet still depends on the shape of the full distribution. Percentile diameters can be calculated from the DSD in any units (e.g. number or mass concentration, differential sedimentation flux); the profiles of percentile diameter presented here are calculated from the mass DSD because number concentration decreases too quickly above the median diameter to be useful in analyzing the tail of the distribution.

Profiles of $d_{99}$ are presented in Fig. 5.12 and illustrate the stark contrast in the DSD between LO and HI simulations. The LO simulations diverge from observed $d_{99}$ within 100 m of cloud top in the 0730 and 0812 cases, with $d_{99}$ biased too large by over 50 μm by midcloud in the 0812 case. Similar bias exists in the 0815-LO simulations near cloud base as well, a clear demonstration of the artificial acceleration of collision-coalescence inherent to mass-doubling resolution, especially given that $N_D$ is greater in the LO simulations by $\sim$ 20%. The LO simulations generally align better with observations of integrated microphysical quantities like LWC and $R$, but this occurs for the wrong reasons; it appears that agreement between LO simulations and observations is more a function of good agreement with observed $N_D$ than it is a reflection of sound physical parameterizations. The constant values of $N_{CCN}$ chosen for each case were iteratively chosen to match $N_D$ in the LO simulations before the high spectral resolution scheme was implemented. Thus while the parameterization of activation is not directly affected by the shift in resolution, differences in the number of activated drops across resolution

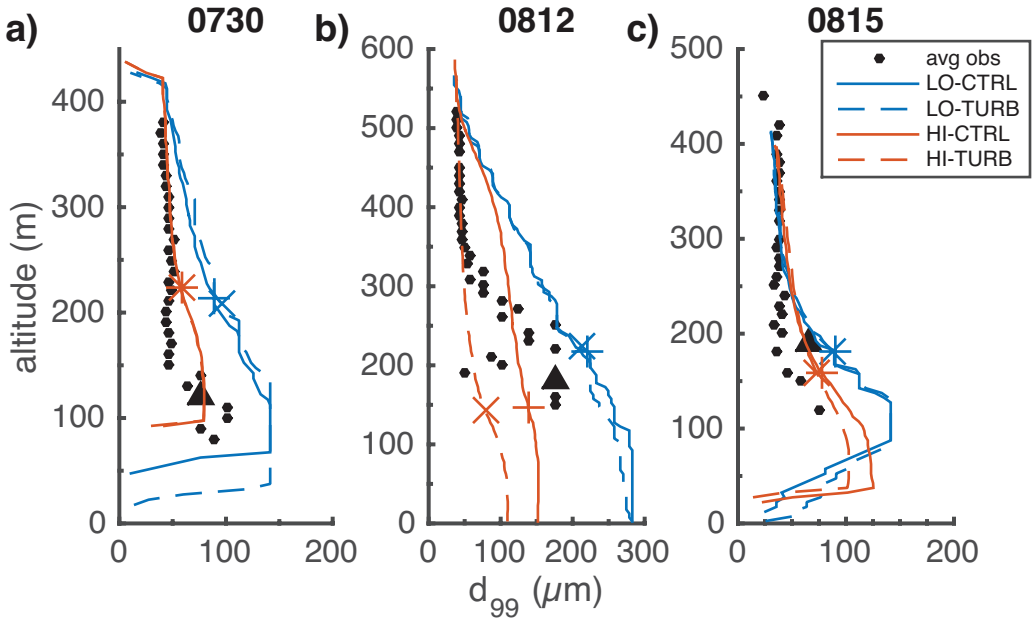



Figure 5.12: Profiles of $d_{99}$ from merged mass DSDs. Colored markers (▲ for observations, + for CTRL runs, × for TURB runs) indicate cloud base, defined as $\overline{LWC(z)} > 0.05\,\mathrm{g\,m^{-3}}$.

has great explanatory power regarding the poorer agreement of observations with HI simulations.

Despite the biases seen in many of the macrophysical variables in the HI simulations, $d_{99}$ profiles from these simulations are in closer agreement with the observations throughout much of the cloud layer in all three cases (Fig. 5.12). The observations show that $d_{99}$ is nearly constant through the top half of the cloud layer; in the 0730 and 0815 cases, significant growth only begins within 20-30 m of cloud base. The HI-TURB simulations perform best in the mid-cloud and cloud top regions because any big drops that do begin to grow higher in the cloud more quickly grow to a size at which they quickly sediment away, effectively reducing the residence time of large drops. Thus the turbulent kernel counterintuitively limits the size to which the largest drops can grow at cloud top by the coupling of collision-coalescence and sedimentation.

Does this trend hold if a more extreme measure of the tail is examined? Profiles of $d_{99.9}$ (Fig. 5.13) show that the LO simulations (CTRL and TURB) still produce drops that are too big, although now the HI simulations bracket the observations with drops that are too small lower in the cloud. Despite this bracketing of the observations by the simulations of differing resolution, the HI simulation results show some overlap with the observations. In comparison with $d_{99}$ (Fig. 5.12), the $d_{99.9}$ profiles show the onset of collisional growth at a much higher altitude in the 0730 and 0812 cases, while in the 0815 case $d_{99.9}$ remains constant in the top $\sim$ 100 m of cloud – possibly the microphysical signature of the overlying haze layer, and certainly supporting the interpretation that 0815 is a non-precipitating case. The same difference in 0812 and 0815 HI-TURB runs is seen in $d_{99.9}$ as in $d_{99}$, namely that the turbulent kernel prevents very large drops from forming at cloud top, which in turn reduces $d_{99.9}$ throughout the depth of the cloud.

Analysis of $d_{99}$ and $d_{99.9}$, two measures of the DSD at the far end of the right tail, show that standard spectral resolution produces drops far too quickly while the turbulent kernel prevents the formation of large drops near cloud top in HI simulations. As a final check that this conclusion is robust, profiles of a less extreme percentile diameter, $d_{90}$,

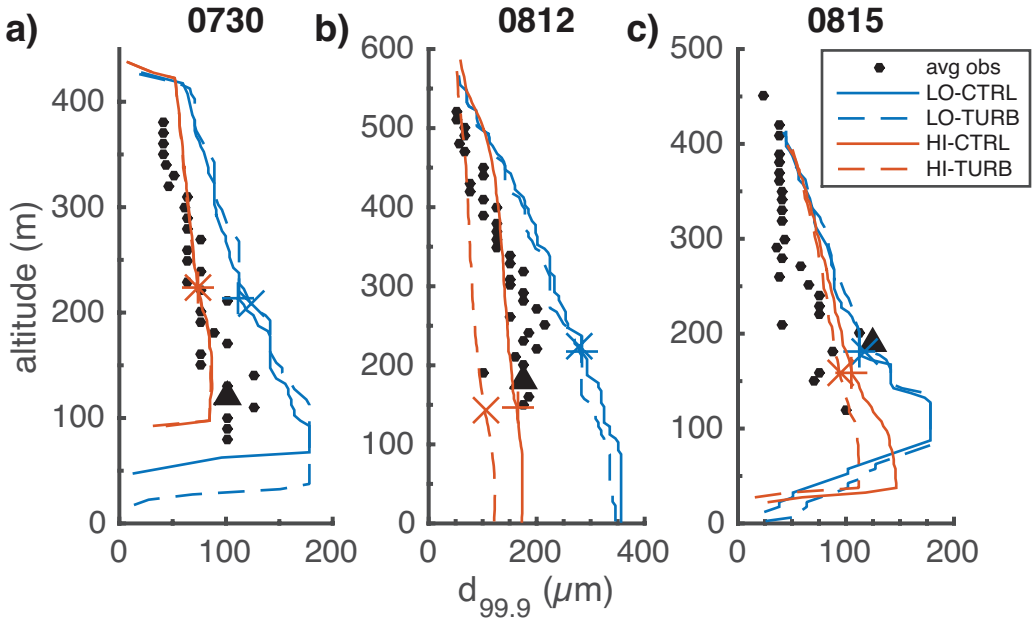



Figure 5.13: Profiles of $d_{99.9}$ from merged DSDs. Colored markers (▲ for observations, + for CTRL runs, × for TURB runs) indicate cloud base, defined as $\overline{LWC(z)} > 0.05\,\mathrm{g\,m^{-3}}$.

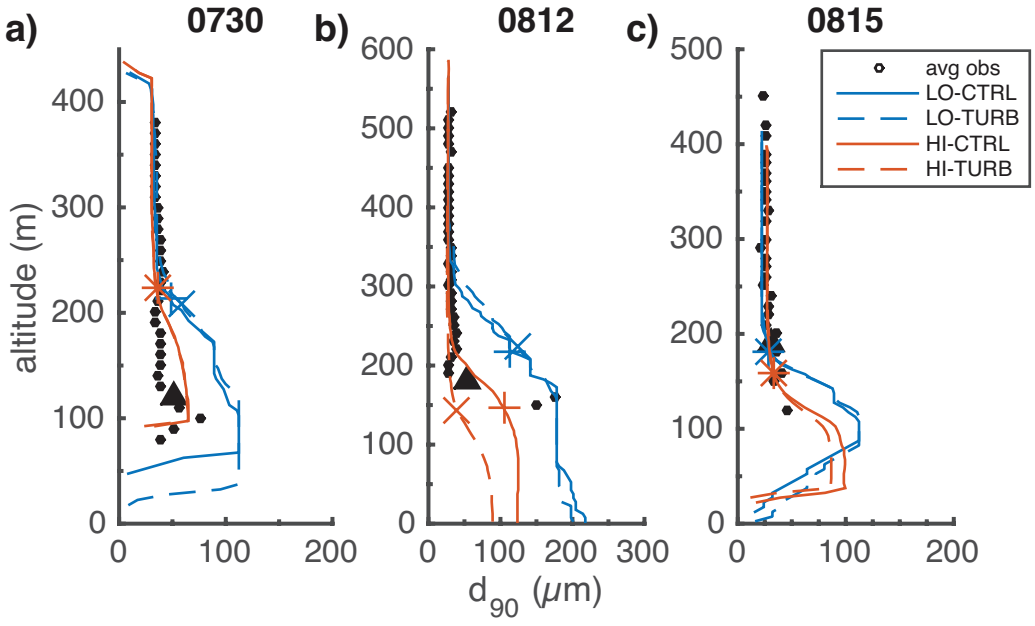



Figure 5.14: Profiles of $d_{90}$ from merged DSDs. Colored markers (▲ for observations, + for CTRL runs, × for TURB runs) indicate cloud base, defined as $\overline{LWC(z)} > 0.05$ g m$^{-3}$.

are shown in Fig. 5.14. Profiles of $d_{99.9}$ (Fig. 5.13) showed more immediate growth than $d_{99}$ (Fig. 5.12); similarly, profiles of $d_{90}$ show less variability through the cloud layer. In fact, cloud layer $d_{90}$ barely varies within the cloud layer or between cases, with values between 25−35 µm for each case. Only at cloud base are major deviations from the cloud layer value observed where small, slowly sedimenting cloud drops evaporate and only the larger drops are left behind. Again, the LO simulations show worse agreement with the observations than the HI simulations, especially in the 0812 case. Aerosol effects on concentration reduce the separation between CTRL and TURB configurations among the HI simulations, but in the subcloud layer HI-CTRL simulations exhibit somewhat higher $d_{90}$, especially in the 0812 case.

## 5.6 Discussion

Simulations of varying spectral resolution and collision-coalescence numerics have been presented to evaluate the ability of the Ayala turbulent collision kernel to improve simulations of marine stratocumulus. In attempting to reconcile the seemingly contradictory effects of the turbulent kernel at different spectral resolution, it became apparent that the outcome of simulations differed enough as a function of resolution that the impact of the kernel with respect to its ability to explain the observations cannot be readily assessed at this time. The LO simulations showed greater precipitation rates (Fig. 5.9), deeper penetration of precipitation into the subcloud layer (Fig. 5.12), and a positive feedback of the turbulent kernel on TKE (Fig. 5.10). The first two outcomes were expected while the third deserves further scrutiny. But profiles of percentile diameter show that the nature of precipitation in the LO simulations bears little resemblance to that observed (Figs. 5.12-5.14). While a drizzle mode is certainly observed in the DSD in the upper reaches of the cloud (e.g. Fig. 5.4), the effect of collisional growth on all but the most extreme percentile diameter examined ($d_{99.9}$, Fig. 5.13) is not apparent until a considerable distance below cloud top in the observations. Observed percentile diameters were calculated from merged DSDs which causes derived percentile diameters to be biased high because of issues with CIP image processing, casting great doubt on the fidelity of the LO simulations.

The HI simulations suffered from different setbacks that prohibit conclusive evaluation of the turbulent kernel. In these simulations, the total drop concentration $N_D$ responded differently than in the LO runs, resulting in much greater $N_D$ in the 0730 and 0812 cases and lower $N_D$ in the 0815 case. As a result of having greater $N_D$, rain rate was drastically reduced completely suppressed in the 0730-HI-CTRL, 0730-HI-TURB and 0812-HI-TURB simulations. In the 0730-HI simulations in particular, no significant difference is noted in any of the microphysical quantities examined. This is not an indictment of the turbulent kernel; rather it raises the point that in order to arrive at the same outcome, the HI and LO sets of simulations require different boundary conditions (more specifically, different CCN concentrations). This would perhaps not be the case

given a more sophisticated approach to activation, but we are unable to assess this claim at present. The main "boundary condition" that creates discrepancies between HI and LO simulations, $N_{CCN}$, is an observationally-constrained quantity outside of cloud but is difficult to diagnose within cloud. In the context of these simulations, $N_{CCN}$ should be viewed as more of a "tunable" parameter to match observed $N_D$ than as an independent boundary condition. Hence it is not contradictory to use different constant $N_{CCN}$ values for standard and high resolution simulations.

This study is not the first to acknowledge the difficulty of process-level attribution with respect to the impact of the turbulent collision kernel [*Grabowski*, 2014]. The response of many other workers has been to remove microphysical feedbacks on dynamics [*Pinsky et al.*, 2008; *Grabowski*, 2014; *Magaritz-Ronen et al.*, 2016] but the coupling of microphysics and dynamics in the presence of precipitation significantly alters the outcome of simulations and cannot be ignored [*Stevens et al.*, 1998; *Ackerman et al.*, 2004; *Bretherton et al.*, 2007]. Instead, the work presented here seeks to use observations as the standard for comparison while holding boundary conditions constant to allow the coupled microphysical-dynamical cloud system to respond in an admittedly more complex but physically relevant manner. The problem with using observations as the point of comparison is that many aspects of covariability in microphysics and meteorology are not captured in LES. They either occur at temporal/spatial scales that cannot be simulated in LES, or they are simply not represented in the model physics. As such, obtaining perfect agreement between observations and LES results may be an ultimately unattainable goal. Despite this, the observations should still serve as the "ground truth," as they can more meaningfully guide future work by demonstrating the shortcomings of the models designed to reproduce them.

# Chapter 6

# Summary

The research presented in this dissertation contributes to expanding mechanistic understanding of the role of microphysical processes in the evolution of cloudy boundary layers. The primary focus was on the role of collision-coalescence in precipitation initiation in marine stratocumulus (MSc) using *in situ* observations of the drop size distribution (DSD) and large eddy simulation (LES) with size-resolved microphysics to guide the inquiries. MSc is the most common cloud on the planet by areal coverage, with changes in coverage of a few percent able to exert a radiative forcing on par with anthropogenic greenhouse gas emissions [*Slingo*, 1990]. Despite their importance, MSc are among the most difficult clouds to simulate in global circulation models because accurate simulation depends on the representation of processes and strong thermodynamic gradients that occur on length scales of a few meters at most. Improvement of microphysical parameterizations in both small and large scale numerical models has wide-ranging implications on our ability to predict weather and make future climate projections.

Each chapter focused on a different aspect of the representation of clouds, but far from conclusively ending any lines of inquiry, the chapters instead illustrate the complexity of cloud systems and serve as a launching point for future investigations. Chapter 2 developed a metric for predicting cumulus life stage from a single measurement of cloud total water mixing ratio to provide context to observations, but pointed out that the

small population of clouds analyzed represents only the simplest narrative of cumulus life cycle. Chapter 3 introduced an analytical framework for retrieving collision rate constants from *in situ* observations of marine stratocumulus, which raises fundamental questions about spatial variability and what exactly constitutes a "local" description of the DSD. Chapter 4 developed and implemented a high spectral resolution microphysics scheme in LES; the implementation of the new scheme was not initially expected to cause any major changes in the outcome of simulations, but this was not the case. Instead, it showed the importance of sedimentation in boundary layer dynamics and highlighted the need for a mechanistic explanation of the sedimentation-entrainment feedback. Finally, Chapter 5 implemented a turbulent collision kernel in the new microphysics scheme, and in so doing highlighted the difficulty of teasing apart the effects of process-level changes on the mean state of the cloud.

The questions raised over the course of this work have directed my attention to two broad problems for future study: 1) whether the currently accepted mathematical description of the DSD is sufficient to describe spatial heterogeneity and 2) how well numerical models can reproduce the observed covariability of meteorology and cloud properties. Both of these problems hint at a deeper question of great relevance to prediction of weather and future climate – how much information is necessary for an accurate description of the state of the atmosphere? Or framed from the opposite viewpoint, how much information can be omitted while still obtaining a reasonable outcome?

On the one hand, the results of this dissertation could be viewed as a statement that more detail, more observations, and a fuller description of atmospheric physics are required to improve our overall understanding of the climate system. At a fundamental level this must be true to some extent, for how are we to describe processes or relationships that have not yet been observed or charcterized? On the other, it points toward a paradigm shift in how outstanding problems are approached. The representation of the DSD in microphyics schemes is an excellent example of a concept that works well in approximation, but may be woefully inadequate to describe clouds in nature. The

DSD as it is presently described is at home in the world of classical physics, described by (relatively) computationally convenient "bin" schemes or smooth parametric distributions. In reality, the DSD is intermittent and rough, with no concept of "identity" in the Eulerian sense due to constant turbulent mixing. Hence it should come as no surprise that numerical models have trouble reproducing the wide observed variability in size-integrated microphysical quantities such as liquid water content and rain rate. A new vocabulary that emphasizes the transience of clouds as well as the immense heterogeneity of cloud properties across length and time scales is necessary. To return to Karl Popper's essay "Of Clocks and Clouds" [*Popper*, 1972], perhaps it is time to abandon the idea that we can force clouds to look like clocks, and focus our energies on describing clouds as they are: turbulent, transient, intermittent in space and time.

# Appendix A

# Details of the rate constant analytical framework

The rate constant analysis is composed of 4 steps: (1) observations of the DSD are rebinned to linear "collision space" based on the monomer diameter $d_0$ and mass $m_0$ such that drops are regrouped as a linear combination of drops of size $m_0$; (2) rate constants are estimated from the observed DSDs assuming the DSD is at steady state; (3) for context, the collision-coalescence box model of *Bott* [1998] is run with a known collision kernel and the DSD is initialized to the shape of the observed DSD to which the box model results will be compared; and (4) rate constants estimated from the observations are divided by the box model-derived rate constants, the result of which is termed the enhancement factor.

Equation 3.1 is the basis for step 2 of the analysis, but we must also take into account other outcomes of collision events than the default outcome of advancing a single bin ($\Delta i = 1$). Collisions may also result in a drop remaining in the same bin ($\Delta i = 0$) or advancing two bins ($\Delta i = 2$). Weights $w_{i,\Delta i}$ for each collision outcome and flight leg are calculated based on the PDI distributions within each collision bin and incorporated into the steady state equation after dividing by $n_0$:

$$k_{i-2} w_{i-2,2} n_{i-2} + k_{i-1} w_{i-1,1} n_{i-1} - k_i (1 - w_{i,0}) n_i = 0 \tag{A.1}$$

where the factor of $(1 - w_{i,0})$ in the third term represents the loss of drops to bin $i+1$, reduced by the fraction of drops that remain in bin $i$.

In step 3, the drop size grid of the Bott model is set to match the PDI lower size bound and spectral resolution ($d_{min}$ = 2.0363 μm and $dlog_{10}d$ = 0.0156, respectively) with 200 bins. The DSD is initialized as a piecewise combination of lognormal and power law distributions (see Section 3.3.1 for more detail). In addition to the distribution parameters $d_0$ and $\beta$, the total drop concentration $N_D$ and LWC are also taken from the observations to initialize the DSD.

# Appendix B

# Validation of radiative fluxes across spectral resolution

We compare radiative fluxes from the 0730 case to ensure that the interpolation performed in the RAMS binned cloud optics scheme does not lead to significant errors. Average radiative flux and radiative flux difference profiles for all 3 cases are shown in Figs. B.1 and B.2. We focus on the 0730 case for two reasons: 1) the profiles of LWC are similar, therefore longwave cooling should be similar since cloud top height and temperature are also similar and 2) it is a daytime case (i.e. nontrivial shortwave flux comparison). Profiles of longwave and shortwave cooling are comparable (Figs. B.3 and B.4, respectively), with very slight differences seen near cloud top where slight differences in LWC are also noted (Fig. 4.5a). Profiles of the other two cases exhibit somewhat greater differences, but this is not surprising because of previously noted differences in cloud top height and LWC.

Vertically integrated radiative fluxes are in close agreement over the entire course of the 0730 simulations, typically differing by no more than a few percent (Figs B.5 and B.6). Differences in liquid water path explain the maxima in integrated flux differences between 2.5 and 3 hours, as a large decrease in LWP begins about 10 minutes earlier in the LO simulation than in the HI simulation (Fig. 4.7a). These results

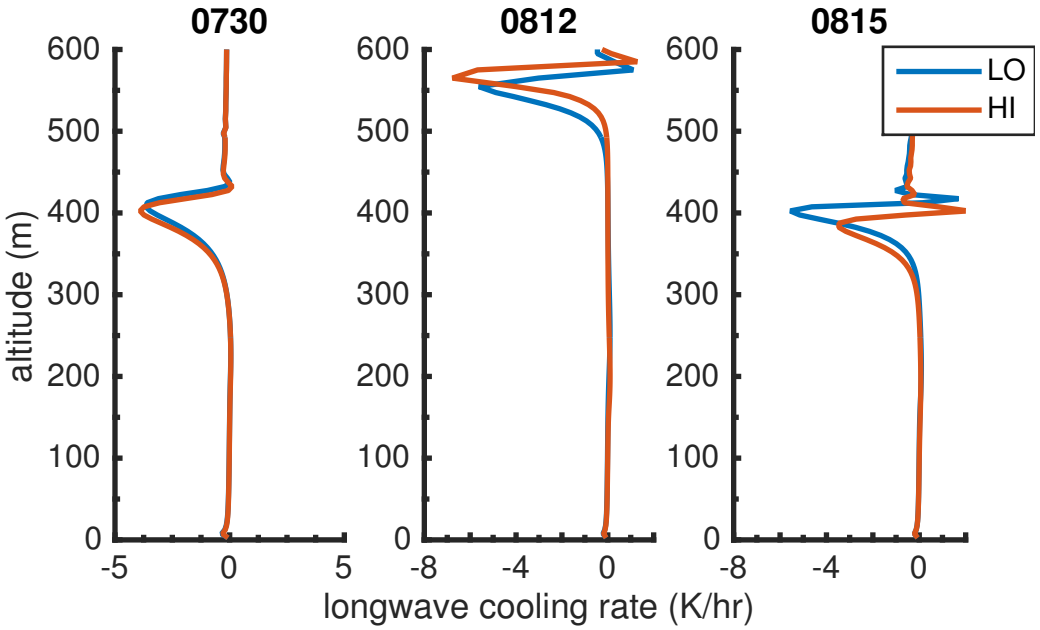



Figure B.1: Profiles of longwave cooling rate

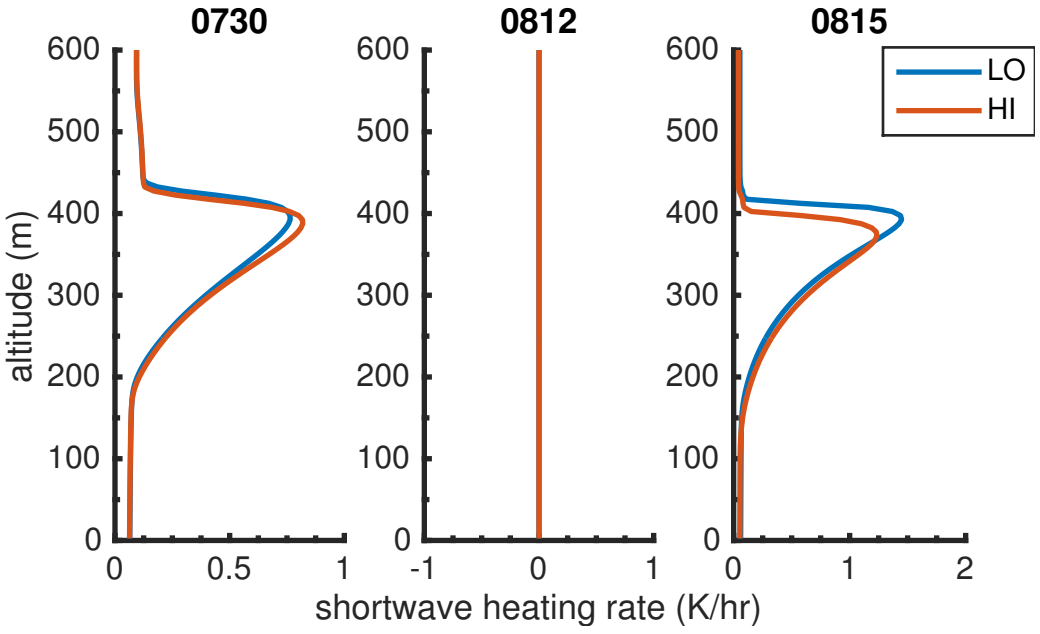



Figure B.2: Profiles of shortwave heating rate

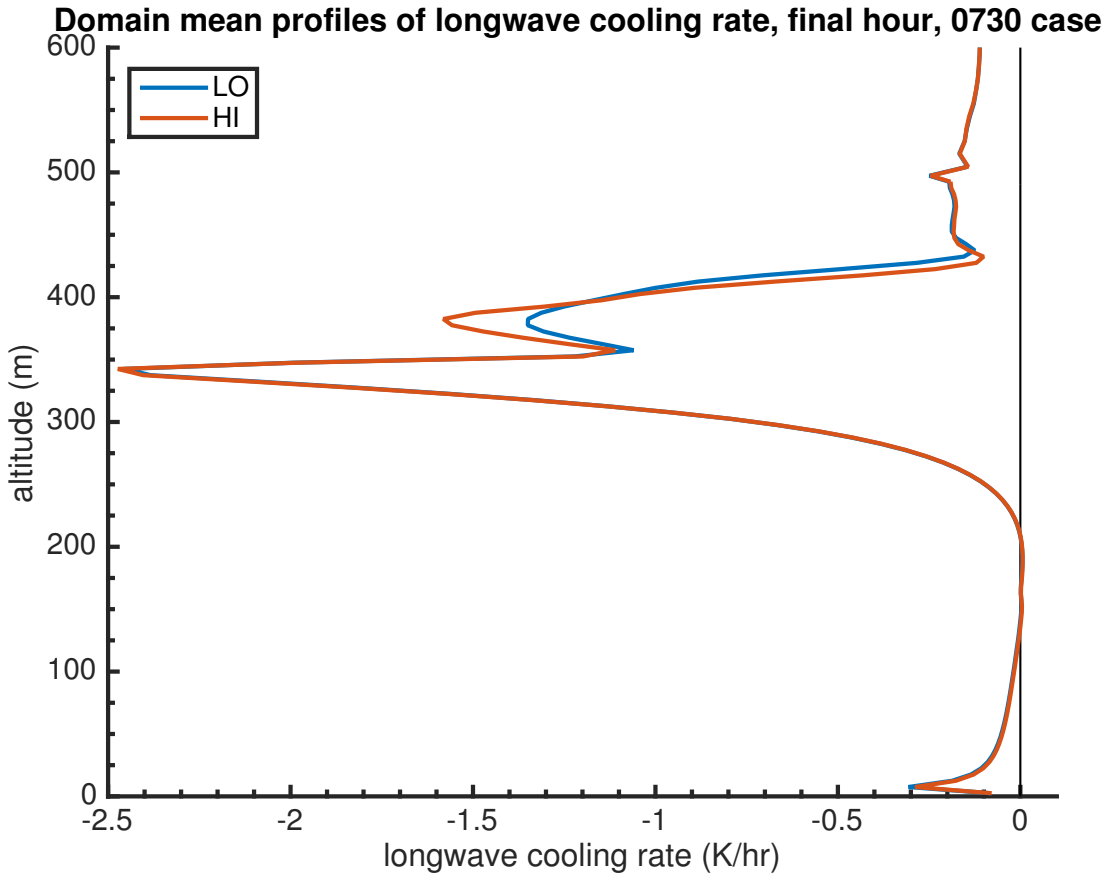



Figure B.3: Profile of longwave cooling rate, 0730 case

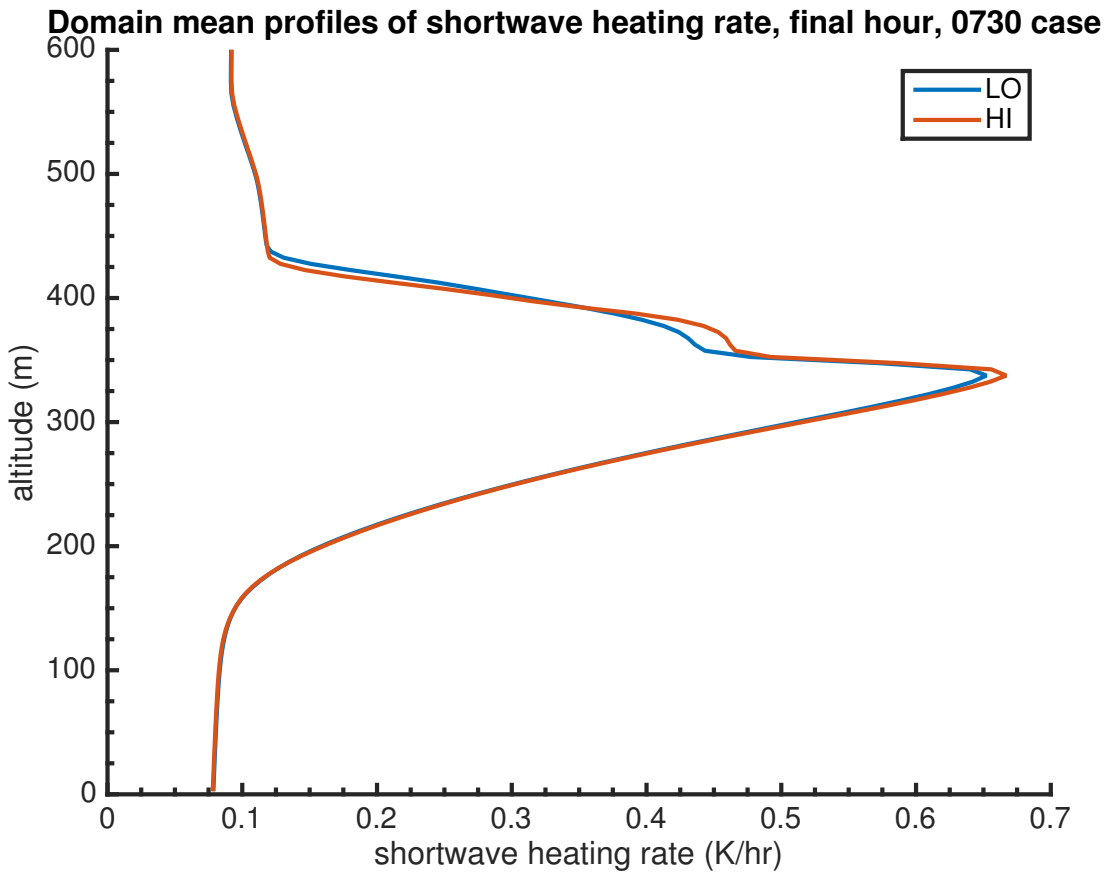



Figure B.4: Profile of shortwave heating rate, 0730 case

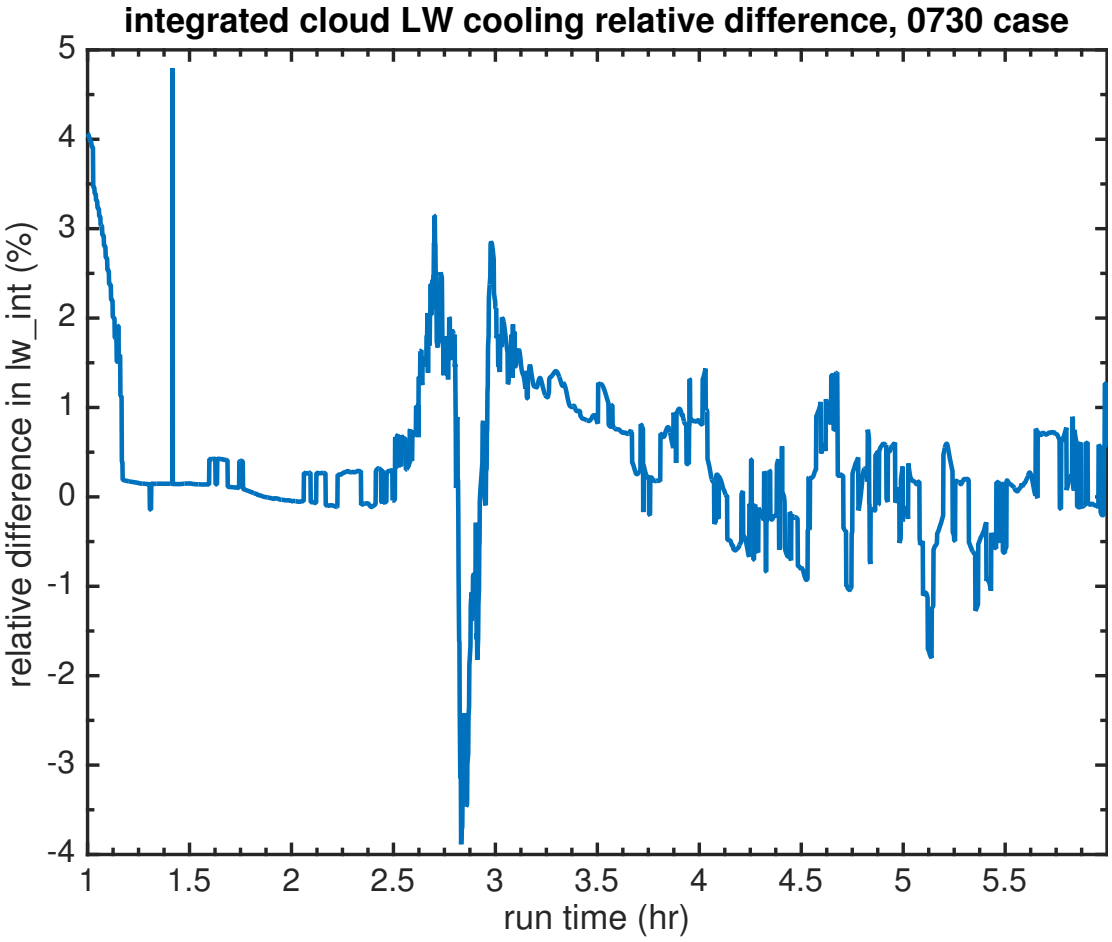



Figure B.5: Relative difference of integrated longwave cooling, 0730 case

confirm that interpolation of the DSD to mass doubling bins in the radiation routine does not produce unacceptable error in radiative fluxes.

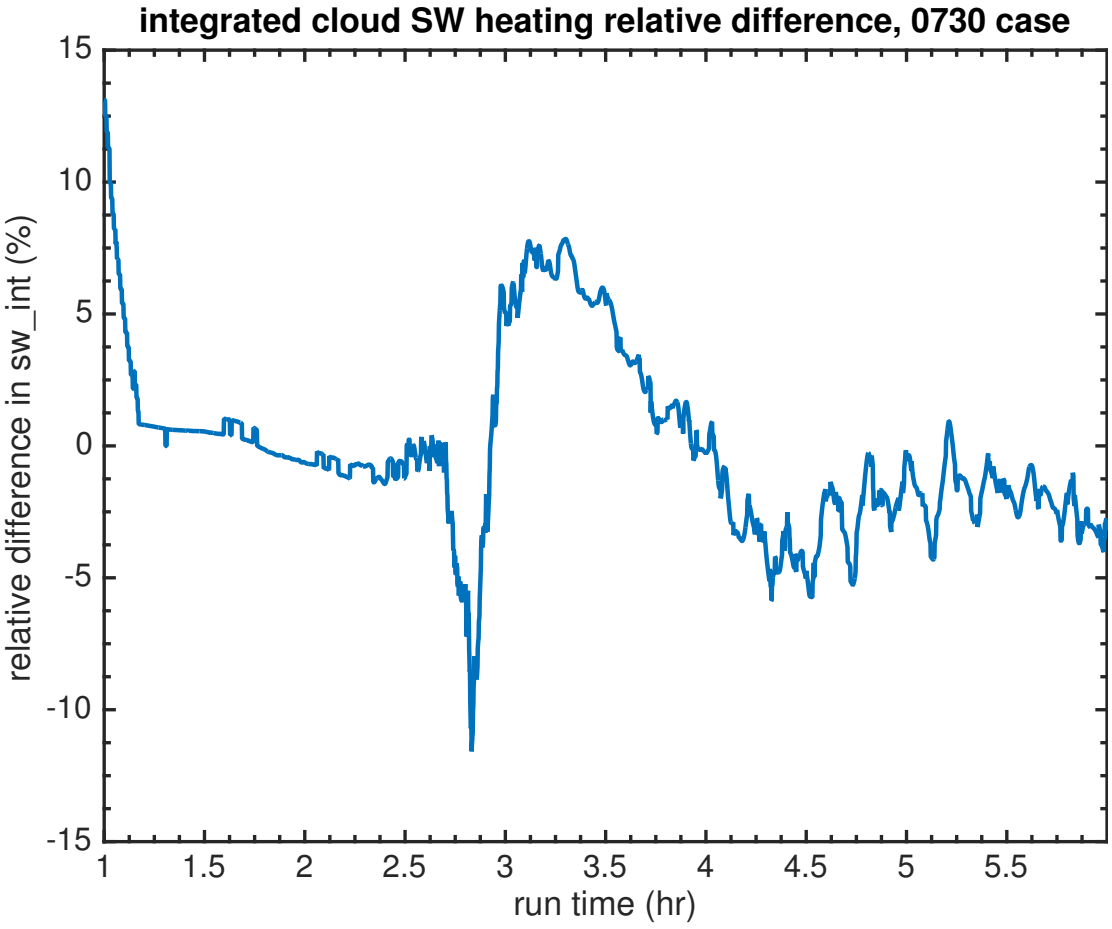



Figure B.6: Relative difference of integrated shortwave heating, 0730 case

# Bibliography

Ackerman, A. S., M. P. Kirkpatrick, D. E. Stevens, and O. B. Toon, The impact of humidity above stratiform clouds on indirect aerosol climate forcing, *Nature*, *432*, 1014–1017, 2004.

Ackerman, A. S., et al., Large-eddy simulations of a drizzling, stratocumulus-topped marine boundary layer, *Mon. Weather Rev.*, *137*, 1083–1110, 2009.

Albrecht, B., D. A. Randall, and S. Nicholls, Observations of marine stratocumulus during fire, *Bull. Amer. Meteor. Soc.*, *69*, 618–626, 1988.

Albrecht, B., M. P. Jensen, and W. J. Syrett, Marine boundary layer structure and fractional cloudiness, *J. Geophys. Res.*, *100*(D7), 14,209–14,222, 1995.

Anderson, K., *Predicting the weather: Victorians and the science of meteorology*, University of Chicago Press, Chicago, 2005.

Arenberg, D., Turbulence as a major factor in the growth of cloud droplets, *Bull. Amer. Meteor. Soc.*, *20*, 444–445, 1939.

Austin, P., Y. Wang, R. Pincus, and V. Kujala, Precipitation in stratocumulus clouds: Observationl and modeling results, *J. Atmos. Sci.*, *52*(13), 1995.

Ayala., O., W. W. Grabowski, and L.-P. Wang, A hybrid appoach for simulating turbulent collisions of hydrodynamically-interacting particles, *J. Comput. Phys.*, *225*(1), 51–73, doi:10.1016/j.jcp.2006.11.016, 2007.

Ayala, O., W. W. Grabowski, and L. P. Wang, A hybrid approach for simulating turbulent collisions of hydrodynamically-interacting particles, *J. Comput. Phys.*, *225*(1), 51–73, 2007.

Ayala, O., B. Rosa, L.-P. Wang, and W. Grabowski, Effects of turbulence on the geometric collision rate of sedimenting droplets. part 1: Results from direct numerical simulation, *New J. Physics*, *10*, 2008a.

Ayala, O., B. Rosa, L.-P. Wang, and W. Grabowski, Effects of turbulence on the geometric collision rate of sedimenting droplets. part 2: Theory and parameterization, *New J. Physics*, *10*, 2008b.

Baker, M. B., and J. Latham, The evolution of droplet spectra and the rate of production of embryonic raindrops in small cumulus clouds, *J. Atmos. Sci.*, *36*(8), 1612–1615, 1979.

Baumgardner, D., and A. Korolev, Airspeed corrections for optical array probe sample volumes, *J. Atmos. Oceanic Technol.*, *14*, 1124–1129, 1997.

Beard, K., and H. Ochs, Warm-rain initiation: an overview of microphysical mechanisms, *J. Applied Metereol.*, *32*(4), 608–625, 1993.

Benmoshe, N., M. Pinsky, A. Pokrovsky, and A. Khain, Turbulent effects on the microphysics and initiation of warm rain in deep convective clouds: 2-d simulations by a spectral mixed-phase microphysics cloud model, *Journal of Geophysical Research*, *117*, D06,220, 2012.

Berry, E., and R. Reinhardt, An analysis of cloud drop growth by collision: part i. double distributions, *J. Atmos. Sci.*, *31*, 1974.

Bleck, R., A fast approximative method for integrating the stochastic coalescence equation, *J. Geophys. Res.*, *75*, 5165, 1970.

Bott, A., A flux method for the numerical solution of the stochastic collection equation, *J. Atmos. Sci.*, *55*, 2284–2293, 1998.

Bretherton, C. S., P. N. Blossey, and J. Uchida, Cloud droplet sedimentation, entrainment efficiency, and subtropical stratocumulus albedo, *Geophys. Res. Let.*, *34*, L03,813, doi:10.1029/2006GL027648, 2007.

Carman, J. K., D. L. Rossiter, D. Khelif, H. H. Jonsson, I. C. Faloona, and P. Y. Chuang, Observational constraints on entrainment and the entrainment interface layer in stratocumulus, *Atmos. Chem. Phys.*, *12*, 11,135–11,152, 2012.

Chuang, P. Y., E. W. Saw, J. D. Small, R. A. Shaw, C. M. Sipperley, G. A. Payne, and W. D. Bachalo, Airborne phase Doppler interferometry for cloud microphysical measurements, *Aerosol Science and Technology*, *42*(8), 685–703, 2008.

Cole, J., Assessing the importance of unresolved cloud-radiation interactions in atmospheric global climate models using the multiscale-modelling framework (ph.d. thesis), Ph.D. thesis, The Pennsylvania State University, 2005.

Cooper, W. A., S. G. Lasher-Trapp, and A. M. Blyth, The influence of entrainment and mixing on the initial formation of rain in a warm cumulus cloud, *J. Atmos. Sci.*, *70*, 1727–1743, 2013.

Dagan, G., I. Koren, and O. Altaratz, Aerosol effects on the timing of warm rain processes, *Geophysical Research Letters*, *42*(11), 4590–4598, doi:10.1002/2015GL063839, 2015GL063839, 2015.

Davis, M., Collisions of small cloud droplets: gas kinetic effects, *J. Atmos. Sci.*, *29*, 911–915, 1972.

Dawe, J., and P. Austin, Statistical analysis of an les shallow cumulus cloud ensemble using a cloud tracking algorithm, *Atmos. Chem. Phys. Discuss.*, *11*, 23,231–23,273, 2011.

de Rooy, W., P. Bechtold, K. Fröhlich, C. Hohenegger, H. Jonker, D. Mironov, A. Siebesma, J. Teixeira, and J.-I. Yano, Entrainment and detrainment in cumulus convection: an overview, *Quart. J. Roy. Meteor. Soc.*, *139*, 1–19, 2013.

deAlmeida, F., The collisional problem of cloud droplets moving in a turbulent environment-part i: a method of solution, *J. Atmos. Sci.*, *33*(8), 1571–1578, 1976.

deAlmeida, F., Collisional problem of cloud droplets moving in a turbulent environment: Turbulent collision efficiencies, *J. Atmos. Sci.*, *36*(8), 1564–1576, 1979a.

deAlmeida, F., Effects of small-scale turbulent motions on the growth of a cloud droplet spectrum, *J. Atmos. Sci.*, *36*(8), 1557–1563, 1979b.

Deardorff, J. W., Stratocumulus-capped mixed layers derived from a 3-dimensional model, *Bound.-Layer Meteor.*, *18*(4), 495–527, 1980.

Defant, A., Gesetzmassigkeiten in der verteilung der vershiedenen tropfengroessen bei regenfÃ€llen, *K. Akad. Wiss., Math.-Naturw. Klasse SitzBer*, *114*, 585–646, [German], 1905.

Devenish, B., et al., Droplet growth in warm turbulent clouds, *Quart. J. Roy. Meteor. Soc.*, 2012.

Dodin, Z., and T. Elperin, On the collision rate of particles in turbulent flow with gravity, *Phys. Fluids*, *14*(8), 2002.

East, T. W. R., and J. S. Marshall, Turbulence in clouds as a factor in precipitation, *Quart. J. Royal Meteo. Soc.*, *80*, 26–47, 1954.

Egan, B. A., and J. R. Mahoney, Numerical modeling of advection and diffusion of urban area source pollutant, *J. Appl. Meteorol.*, *11*, 312–322, 1972.

Feingold, G., B. Stevens, W. R. Cotton, and R. L. Walko, An explicit cloud microphysics/les model to simulate the twomey effect, *Atmos. Res.*, *33*, 207–233, 1994.

Feingold, G., B. Stevens, W. R. Cotton, and A. S. Frisch, The relationship between drop in-cloud residence time and drizzle production in numerically simulated stratocumulus clouds, *J. Atmos. Sci.*, *53*(8), 1108–1122, 1996.

Feingold, G., W. R. Cotton, S. M. Kreidenweis, and J. T. Davis, The impact of giant cloud condensation nuclei on drizzle formation in stratocumulus: Implications for cloud radiative properties, *Journal of the Atmospheric Sciences*, *56*(24), 4100–4117, doi:10.1175/1520-0469(1999)056<4100:TIOGCC>2.0.CO;2, 1999.

Fielding, M., J. Chiu, R. Hogan, and G. Feingold, 3d cloud reconstructions: Evaluation of scanning radar scan strategy with a view to shortwave radiation closure, *J. Geophys. Res.*, 2013.

Franklin, C., A warm rain microphysics parameterization that includes the effect of turbulence, *J. Atmos. Sci.*, *65*(6), 1795–1816, 2008.

Franklin, C., The effects of turbulent collision-coalescence on precipitation formation and precipitation-dynamical feedbacks in simulations of stratocumulus and shallow cumulus convection, *Atmos. Chem. Phys.*, *14*, 6557–6570, doi:10.5194/acp-14-6557-2014, 2014.

Geoffroy, O., J.-L. Brenguier, and F. Burnet, Parametric representation of the cloud droplet spectra for les warm bulk microphysical schemes, *Atmos. Chem. Phys.*, *10*, 4835–4848, 2010.

Gerber, H., G. Frick, S. P. Malinowski, H. Jonsson, D. Khelif, and S. K. Krueger, Entrainment rates and microphysics in post stratocumulus, *Journal of Geophysical Research: Atmospheres*, *118*, 12,094–12,109, 2013.

Gillespie, D., An exact method for numerically simulating the stochastic coalescence process in a cloud, *J. Atmos. Sci.*, *32*, 1975, 1975.

Golaz, J.-C., V. E. Larson, and W. R. Cotton, A pdf-based model for boundary layer clouds. part i: Method and model description, *J. Atmos. Sci.*, *59*, 3540–3551, 2002.

Grabowski, W. W., Numerical experiments on the dynamics of the cloud-environment interface: Small cumulus in a shear free environment, *J. Atmos. Sci.*, *46*, 3513–3541, 1989.

Grabowski, W. W., Extracting microphysical iimpact in large-eddy simulations of shallow convection, *J. Atmos. Sci.*, *71*, 4493–4499, doi:10.1175/JAS-D-14-0231.1, 2014.

Hall, W., A detailed microphysical model within a two-dimensional dynamic framework: model description and preliminary results, *J. Atmos. Sci.*, *37*, 1980.

Harrington, J., The effects of radiative and microphysical processes on simulated warm and transition season arctic stratus (ph.d. thesis), Ph.D. thesis, Colorado State University, 1997.

Harrington, J. Y., and P. Q. Olsson, A method for the parameterization of cloud optical properties in bulk and bin microphysical models. implications for arctic cloudy boundary layers, *Atmos. Res.*, *57*(1), 51–80, 2001.

Hartmann, D. L., *Global Physical Climatology*, Academic Press, 1994.

Heus, T., H. Jonker, H. Van den Akker, E. Griffith, M. Koutek, and F. Post, A statistical approach to the life cycle analysis of cumulus clouds selected in a virtual reality environment, *J. Geophys. Res.*, 2009.

Hocking, L. M., and P. R. Jonas, The collision efficiency of small drops, *Quarterly Journal of the Royal Meterological Society*, *96*(410), 722–729, 1970.

Hsieh, W. C., H. Jonsson, L. P. Wang, G. Buzorius, R. C. Flagan, J. H. Seinfeld, and A. Nenes, On the representation of droplet coalescence and autoconversion: Evaluation using ambient cloud droplet size distributions, *J. Geophys. Res. Atmos.*, *114*, 2009.

IPCC, *Climate Change 2013: The Physical Science Basis. Contribution of Working Group I to the Fifth Assessment Report of the Intergovernmental Panel on Climate*

*Change*, 1535 pp., Cambridge University Press, Cambridge, United Kingdom and New York, NY, USA, 2013.

Jiang, H., H. Xue, A. Teller, G. Feingold, and Z. Levin, Aerosol effects on the lifetime of shallow cumulus, *Geophys. Res. Let.*, 2006.

Jiang, H., G. Feingold, and I. Koren, Effect of aerosol on trade cumulus cloud morphology, *J. Geophys. Res.*, *114*, 2009.

Jiang, H., G. Feingold, and A. Sorooshian, Effect of aerosol on the susceptibility and efficiency of precipitation in warm trade cumulus clouds, *J. Atmos. Sci.*, *67*, 2010.

Johnson, D. B., The role of giant and ultragiant aerosol particles in warm rain initiation, *J. Atmos. Sci.*, *39*, 448–460, 1982.

Jonas, P., The collision efficiency of small drops, *Quart. J. Roy. Meteor. Soc.*, *98*(417), 681–683, 1972.

Khain, A. P., et al., Represenation of microphysical processes in cloud-resolving models: Spectral (bin) microphysics versus bulk parameterization, *Rev. Geophys.*, *53*, 247–322, 2015.

Klein, S., and D. Hartmann, The seasonal cycle of low stratiform clouds, *J. Climate*, *6*(8), 1587–1606, 1993.

Klett, J., and M. Davis, Theoretical collision efficiencies of cloud droplets at small reynolds numbers, *J. Atmos. Sci.*, *30*(1), 107–117, 1975.

Knight, C. A., J. Vivekanandan, and S. G. Lasher-Trapp, First radar echoes and the early z(dr) history of florida cumulus, *J. Atmos. Sci.*, *59*(9), 1454–1472, 2002.

Kolmogorov, A., A refinement of previous hypotheses concerning the local structure of turbulence in a viscous incompressible fluid at high reynolds number, *J. Fluid Mech.*, *13*(1), 82–85, 1962.

Koren, I., O. Altaratz, G. Feingold, Z. Levin, and T. Reisin, Cloud's center of gravity - a compact approach to analyze convective cloud development, *Atmos. Chem. Phys.*, *9*, 155–161, 2009.

Korolev, A., Reconstructino of the sizes of spherical particles from their shadow images. part i: Theoretical considerations, *J. Atmos. Oceanic Technol.*, *24*, 376–389, doi: 10.1175/JTECH1980.1, 2007.

Kostinski, A. B., and R. A. Shaw, Scale-dependent droplet clustering in turbulent clouds, *J. Fluid Mech.*, *434*, 389–398, 2001.

Kostinski, A. B., and R. A. Shaw, Fluctuations and luck in droplet growth by coalescence, *Bull. Am. Meteorol. Soc.*, *86*(2), 235–+, 2005.

Larson, V. E., and B. M. Griffin, Analytic upscaling of a local microphysics scheme. part i: Derivation, *Quart. J. Roy. Meteor. Soc.*, *139*, 46–57, 2013.

Lau, K., and H. Wu, Warm rain processes over tropical oceans and climate implications, *Geophysical Research Letters*, *30*(24), 2290, 2003.

Lehmann, K., H. Siebert, and R. A. Shaw, Homogeneous and inhomogeneous mixing in cumulus clouds: Dependence on local turbulence structure, *J. Atmos. Sci.*, *66*(12), 3641–3659, 2009.

Leon, D. C., Z. Wang, and D. Liu, Climatology of drizzle in marine boundary layer clouds based on 1 year of data from cloudsat and cloud-aerosol lidar and infrared pathfinder satellite observations (calipso), *J. Geophys. Res.*, *113*, D00A14, doi:10. 1029/2008JD009835, 2008.

Lin, C., and S. Lee, Collision efficiency of water drops in the atmosphere, *J. Atmos. Sci.*, *32*, 1412–1418, 1975.

Long, A. B., Solutions to the droplet collection equation for polynomial kernels, *J. Atmos. Sci.*, *31*, 1040–1052, 1974.

Lu, M. L., W. C. Conant, H. H. Jonsson, V. Varutbangkul, R. C. Flagan, and J. H. Seinfeld, The marine stratus/stratocumulus experiment (mase): Aerosol-cloud relationships in marine stratocumulus, *J. Geophys. Res. Atmos.*, *112*(D10), 2007.

Magaritz-Ronen, L., M. Pinsky, and A. Khain, Drizzle formation in stratocumulus clouds: effects of turbulent mixing, *Atmos. Chem. Phys.*, *16*, 1849–1862, 2016.

Malinowski, S. P., H. Gerber, I. J.-L. Plante, M. K. Kopec, W. Kumala, K. Nurowska, P. Y. Chuang, D. Khelif, and K. E. Haman, Physics of stratocumulus top (post): turbulent mixing across capping inversion, *Atmos. Chem. Phys.*, *13*, 12,171–12,186, 2013.

Martin, G. M., D. W. Johnson, and A. Spice, The measurement and parameterization of effective radius of droplets in warm stratocumulus clouds, *J. Atmos. Sci.*, *51*(13), 1994.

Maxey, M. R., The gravitational settling of aerosol-particles in homogeneous turbulence and random flow-fields, *J. Fluid Mech.*, *174*, 441–465, 1987.

McClatchy, R. A., R. W. Fenn, J. E. A. Selby, F. E. Volz, and J. S. Garing, Optical properties of the atmosphere, *Environmental Research Papers 411*, Air Force Cambridge Research Laboratories, Bedford MA, 1971.

Medeiros, B., B. Stevens, I. M. Held, M. Zhao, D. L. Williamson, J. G. Olson, and C. S. Bretherton, Aquaplantets, climate sensitivity and low clouds, *J. Climate*, *21*(19), 4971–4991, 2008.

Melzak, Z. A., A scalar transport equation, *Trans. Amer. Math. Soc.*, *85*, 547, 1957.

Petters, J. L., H. Jiang, G. Feingold, D. L. Rossiter, D. Khelif, L. C. Sloan, and P. Y. Chuang, A comparative study of the response of modeled non-drizzling stratocumulus to meteorological and aerosol perturbations, *Atmos. Chem. Phys.*, *13*, 2507–2529, doi:10.5194/acp-13-2507-2013, 2013.

Pincus, R., and S. A. Klein, Unresolved spatial variability and microphysical process rates in large-scale models, *J. Geophys. Res.*, *105*(D22), 27,059–27,065, 2000.

Pinsky, M., and A. Khain, Formation of inhomogeneity in drop concentration induced by the inertia of drops falling in a turbulent flow, and the influence of the inhomogeneity on the drop-spectrum broadening, *Quart. J. Roy. Meteor. Soc.*, *123*(537), 165–186, 1997a.

Pinsky, M., A. Khain, and M. Shapiro, Collisions of small drops in a turbulent flow. part i: Collision efficiency. problem formulation and preliminary results, *J. Atmos. Sci.*, *56*(15), 2585–2600, 1999.

Pinsky, M., L. Magaritz, A. Khain., O. Krasnov, and A. Sterkin, Investigation of droplet size distribution and drizzle formation using a new trajectory ensemble model. part i: Model description and first results in a nonmixing limit, *J. Atmos. Sci.*, *65*, 2064–2086, doi:10.1175/2007JAS2486.1, 2008.

Pinsky, M. B., and A. P. Khain, Turbulence effects on the collision kernel .1. formation of velocity deviations of drops falling within a turbulent three-dimensional flow, *Quart. J. Roy. Meteor. Soc.*, *123*(542), 1517–1542, 1997b.

Pinsky, M. B., A. P. Khain, and M. Shapiro, Collisions of cloud droplets in a turbulent flow. part iv: Droplet hydrodynamic interaction, *J. Atmos. Sci.*, *64*(7), 2462–2482, 2007.

Pope, S. B., *Turbulent flows*, Cambridge University Press, Cambridge, 2000.

Popper, K., *Objective Knowledge: An Evolutionary Approach*, revised ed., Oxford University Press, USA, 1972.

Pruppacher, H., and J. Klett, *Microphysics of Clouds and Precipitation*, 2 ed., Klewer Academic, 1997.

Reade, W., and L. R. Collins, Effect of preferential concentration on turbulent collision rates, *Phys. Fluids*, *12*(10), 2000.

Reiche, C. H., and S. Lasher-Trapp, The minor importance of giant aerosol to precipitation development within small trade wind cumuli observed during {RICO}, *Atmospheric Research*, *95*(4), 386 – 399, doi:http://dx.doi.org/10.1016/j.atmosres.2009.11.002, 2010.

Rogers, R., and M. Yau, *A Short Course in Cloud Physics*, 3 ed., Butterworth Heinemann, 1989.

Rossiter, D. L., Observational studies of drizzle in marine stratocumulus, Ph.D. thesis, University of California Santa Cruz, 2012.

Rotstayn, L. D., On the "tuning" of autoconversion parameterization, *J. Geophys. Res.*, *105*, 15,495–15,507, 2000.

Saffman, P., and J. Turner, On the collision of drops in turbulent clouds, *J. Fluid Mech.*, 1956.

Saw, E., R. Shaw, S. Ayyalasomayajula, P. Chuang, and A. Gylfason, Inertial clustering of particles in high-reynolds-number turbulence, *Physical Review Letters*, *100*, 214,501, 2008.

Seifert, A., L. Nuijens, and B. Stevens, Turbulence effects on warm-rain autoconversion in precipitating shallow convection, *Quart. J. Roy. Meteor. Soc.*, *136*, 1753–1762, 2010.

Shafrir, U., and T. Gal-Chen, A numerical study of the collision efficiencies and coalescence parameters for droplet pairs with radii up to 300 microns, *J. Atmos. Sci.*, *28*(7), 741–751, 1971.

Shaw, R., Particle-turbulence interactions in atmospheric clouds, *Annu. Rev. Fluid Mech.*, *34*, 183–227, 2003.

Shaw, R. A., and S. P. Oncley, Acceleration intermittency and enhanced collision kernels in turbulent clouds, *Atmos. Res.*, *59*, 77–87, 2001.

Siebert, H., R. Shaw, and Z. Warhaft, Statistics of small-scale velocity fluctuations and internal intermittency in marine stratocumulus clouds, *J. Atmos. Sci.*, *67*(1), 262–273, 2010.

Slingo, A., Sensitivity of the earth's radiation budget to changes in low clouds, *Nature*, *343*, 49–51, 1990.

Smoluchowski, M., Brownian motions, *Tech. rep.*, Observatoria Nauchno Technicheskoi Informatzii, [Russian], 1936.

Squires, K. D., and J. K. Eaton, Particle response and turbulence modification in isotropic turbulence, *Phys. Fluids A*, *2*(7), 1990.

Stevens, B., Atmospheric moist convection, *Annu. Rev. Earth Planet. Sci.*, *33*, 605–43, 2005.

Stevens., B., and G. Feingold, Untangling aerosol effects on clouds and precipitation in a buffered system, *Nature*, *461*, 607–613, doi:10.1038/nature08281, 2009.

Stevens, B., G. Feingold, W. R. Cotton, and R. L. Walko, Elements of the microphysical structure of numerically simulated nonprecipitating stratocumulus, *J. Atmos. Sci.*, *53*(7), 980–1006, 1996a.

Stevens, B., R. L. Walko, W. R. Cotton, and G. Feingold, The spurious production of cloud-edge supersaturations by eulerian models, *Mon. Weather Rev.*, *124*, 1034–1041, 1996b.

Stevens, B., W. R. Cotton, G. Feingold, and C.-H. Moeng, Large-eddy simulations of strongly precipitating, shallow, stratocumulus-topped boundary layers, *J. Atmos. Sci.*, *55*, 3616–3638, 1998.

Stevens, B., et al., Dynamics and chemistry of marine stratocumulus – dycoms-ii, *Bull. Amer. Meteor. Soc.*, *84*(5), 579–593, doi:10.1175/BAMS-84-5-579, 2003.

Stevens, B., et al., Evauation of large-eddy simulations via observations of nocturnal marine stratocumulus, *Mon. Weather Rev.*, *133*, 1443–1462, 2005.

Strapp, J. W., F. Albers, A. Reuter, A. V. Korolev, U. Maixner, E. Rashke, and Z. Vukovic, Laboratory measurement of the response of a pms oap-2dc, *J. Atmos. Oceanic Technol.*, *18*, 1150–1170, 2001.

Sundaram, S., and L. R. Collins, Collision statistics in an isotropic particle-laden turbulent suspension .1. direct numerical simulations, *J. Fluid Mech.*, *335*, 75–109, 1997.

Telford, J. W., N. S. Thorndike, and E. G. Bowen, The coalescence between small water drops, *Quart. J. Roy. Meteor. Soc.*, *81*(148), 241–250, doi:10.1002/qj.49708134810, 1955.

Tzivion, S., G. Feingold, and Z. Levin, An efficient numerical solution to the stochastic collection equation, *J. Atmos. Sci.*, *44*(21), 3139–3149, 1987.

Tzivion, S., G. Feingold, and Z. Levin, The evolution of rain-drop spectra. part ii: Collisional collection/breakup and evaporation in a rain shaft, *J. Atmos. Sci.*, *46*, 3312–3327, 1989.

Tzivion, S., T. G. Reisin, and Z. Levin, A numerical solution of the kinetic collection equation using high spectral grid resolution: a proposed reference, *J. Comput. Phys.*, *148*, 527–544, doi:jcph.1998.6128, 1999.

Vali, G., R. D. Kelly, J. French, S. Haimov, D. Leon, R. E. McIntosh, and A. Pazmany, Finescale structure and microphysics of coastal stratus, *J. Atmos. Sci.*, *55*(24), 3540–3564, 1998.

vanZanten, M. C., and B. Stevens, Observations of the structure of heavily precipitating marine stratocumulus, *J. Atmos. Sci.*, *62*(12), 4327–4342, 2005.

Wang, L.-P., and W. Grabowski, The role of air turbulence in warm rain initiation, *Atmos. Sci. Let.*, *10*, 1–8, 2009.

Wang, L.-P., and M. R. Maxey, Settling velocity and concentration distribution of heavy particles in homogeneous isotropic turbulence, *J. Fluid Mech.*, *256*, 27–68, 1993a.

Wang, L. P., and M. R. Maxey, Settling velocity and concentration distribution of heavy-particles in homogeneous isotropic turbulence, *J. Fluid Mech.*, *256*, 27–68, 1993b.

Wang, L.-P., O. Ayala, S. Kasprzak, and W. Grabowski, Theoretical formulation of collision rate and collision efficiency of hydrodynamically interacting cloud droplets in turbulent atmosphere, *J. Atmos. Sci.*, *62*(7), 2433–2450, 2005.

Wang, L.-P., Y. Xue, O. Ayala, and W. Grabowski, Effects of stochastic coalescence and air turbulence on the size distribution of cloud droplets, *Atmos. Research*, *82*, 416–432, 2006.

Wang, L.-P., O. Ayala, B. Rosa, and W. Grabowski, Turbulent collision efficiency of heavy particles relevant to cloud droplets, *New J. Physics*, *10*, 2008.

Wang, P., On the definition of collision efficiency of atmospheric particles, *J. Atmos. Sci.*, *40*(4), 1051–1052, 1983.

Wood, R., Stratocumulus clouds, *Monthly Weather Review*, *140*, 2373–2423, 2012.

Wood, R., M. KÃ¶hler, R. Bennartz, and C. O'Dell, The diurnal cycle of surface divergence over the global oceans, *Quart. J. Roy. Meteor. Soc.*, *135*, 1484–1493, 2009.

Wood, R., C. R. Mechoso, and C. S. e. a. Bretherton, The vamos ocean-cloud-atmosphere-land study regional experiment (vocals-rex): goals, platforms, and field operations, *Atmos. Chem. Phys.*, *11*(2), 627–654, 2011.

Wyszogrodzki, A. A., W. W. Grabowski, L.-P. Wang, and O. Ayala, Turbulent collision-coalescence in maritime shallow convection, *Atmos. Chem. Phys.*, *13*, 8471–8487, doi:10.5194/acp-13-8471-2013, 2013.

Xue, H., and G. Feingold, Large-eddy simulations of trade wind cumuli: Investigation of aerosol indirect effects, *J. Atmos. Sci.*, *63*, 1605–22, 2006a.

Xue, H., and G. Feingold, Large-eddy simulations of trade wind cumuli: investigation of aerosol indirect effects, *J. Atmos. Sci.*, *63*(6), 1605–1622, 2006b.

Xue, Y., L.-P. Wang, and W. Grabowski, Growth of cloud droplets by turbulent collision-coalescence, *J. Atmos. Sci.*, *65*(2), 331–356, 2008.

Yang, F., R. Shaw, and H. Xue, Conditions for super-adiabatic droplet growth after entrainment mixing, *Atmos. Chem. Phys. Discuss.*, doi:10.5194/acp-2016-94, 2016.